Analysis of Combined Isotropic and Anisotropic Line-Width Data With a View to Improved Rotational CARS Thermometry

Mark John Newlyn Horner

June, 2002

Abstract

The development of a new line-width model and recently measured rotational (anisotropic) line-widths has allowed for a critical analysis of the various basis rates models. These basis rates will be analysed using both vibrational (isotropic) and rotational line-width data. The data sets are analysed individually and in combination. For all fits, parameter correlations are determined. In addition, the sensitivity of the goodness of fit to variations in the effective interaction length for collisions, l_c, is investigated. To complete the investigation full rotational spectra are calculated and compared with experimental spectra.

Acknowledgements

I would like to acknowledge the following:

My supervisor, Prof. G. Robertson, without whom this project would not have been what it is.

Prof. H.S. Driver, for all his patience and advice.

My parents, for all their loving support. Sorry about the delay.

Sarah and Nicky, for listening and talking.

The gang (Rory, Bruce, Sahal, Spencer, Sam (the Token Irishman) and Vanessa), for good coffee-time conversation and ponytail theory.

Again to Spencer, Sarah and Prof. Driver, for being prepared to proofread.

My blondes, for caring and keeping life interesting and fun.

Contents

List of Figures

List of Tables

Chapter 1

Introduction

This work is focussed on making a contribution to the field of temperature diagnostics. In particular, to improve a technique which is used in industry for the probing of temperatures in volatile gases. This work will not develop a technique but improve the basis on which code for actual temperature diagnostics can be based.

A critical analysis of the various competing methods of calculating certain quantities, vital for temperature diagnostics, will be presented in light of recent experimental results. The identification of the most accurate method will be one result. In addition it will be shown how well experimental results can reproduced.

For temperature diagnostics in a gas, a spectrum of one of the constituents of the gas is measured. The spectral profile has some temperature dependence. An accurate knowledge of the dependence of the spectral profile on temperature allows the temperature to be fitted from the spectrum.

The technique, which this document intends to contribute to, will be rotational Coherent Anti-Stokes Raman Spectroscopy. Coherent Anti-Stokes Raman Spectroscopy is commonly referred to as CARS. Using CARS for temperature diagnostics involves analysing a particular spectrum of some gas which will be specific to the application. The spectrum is measured by the stimulated Raman effect. Rotational CARS deals with the rotational spectrum while vibrational CARS clearly involves the vibrational spectrum.

1.1 Line-Widths

Clearly the more accurately the experimental spectrum can be measured or the more accurate the theoretical spectra are the more accurate the fit. The contribution made in this work will be to the theoretical aspect rather than

to experimental technique. A CARS spectrum is just an intensity profile which consists of peaks corresponding to transitions. The shape and width of these peaks requires calculation. The width of the peaks, which are termed line-widths, can, in principle, be calculated. An integral part of the calculation of spectra is the calculation of line-widths. Line-width calculations are complicated and there is some uncertainty as to which technique is the best to use for this purpose. In this document the various methods that form a basis for line-width calculations will be evaluated and compared.

The spectral lines have a width which has a complex dependence on, amongst other things, energy, velocity and collisions. These will be mentioned in more detail later.

The stumbling block is that the mechanism which results in the broadening of the lines has properties which are unknown. In particular, collision broadening, which in fact dominates, can only be calculated if the true form of the potential between the collision participants is known. In collision broadening a radiating molecule is perturbed in a collision, which results in a change of phase or frequency of the emitted radiation. These changes decrease the coherence length and thus broaden the peaks in the intensity spectrum for the radiating molecule. Unfortunately, the basic trends of how the potential between collision participants should behave are known but its specific form is not.

This results in various approximation methods being required to calculate the collision broadening induced line-widths. Later it will be shown that the uncertainty over the form of the potential has, in effect, been confined to an uncertainty over the form of the basis rates which occur in the line-width model.

The model implemented in this document is the result of work done by Xavier Bruet and is discussed further in 2.7.2. It must be mentioned that this is the first theoretical analysis which results in a model capable of accounting for both vibrational and rotational line-widths.

The analysis presented here will use the available experimental line-width data to choose the most accurate form of the basis rates. The final decision will be based solely on the ability of the model to reproduce the experimental data. This is a very pragmatic approach and implemented strictly to find the best fit.

The unequivocal choice of a basis for the line-width calculation adds to the stability of the technique and allows energy to be focussed on other areas.

This thesis will show that the most recent theoretical treatments of the line-width problem do in fact allow for one set of parameters which characterise both the vibrational and rotational line-widths. The vibrational problem has been the subject of much work, primarily because of the use of the

vibrational spectra for diagnostics. With the latest line-width models and experimental rotational line-widths at various temperatures the technique of using rotational spectra for temperature diagnostics has become more feasible. A more detailed comparison of the two techniques can be found in 2.6.

This, along with the constant improvement in the processing power of computers, will allow for the refinement of rotational CARS temperature diagnostic techniques.

1.2 CARS

In rotational CARS a spectral profile of the rotational Raman transitions for the probed molecule is built. This spectrum depends on the temperature of the medium and thus if the spectrum can be measured and analysed accurately the temperature can be determined.

The choice of transitions to be probed can significantly affect the accuracy of the results. The two primary candidates for probing are the vibrational spectrum and the rotational spectrum. A large amount of work has been put into the development of vibrational CARS. The vibrational spectra are also termed Q-branch spectra. Rotational spectra are termed S-branch spectra. This nomenclature originates from spectroscopy where the branch structure is determined by the change in J. In spectroscopy branches exist for various types of transitions characterised by different changes in quantum numbers. The naming convention is as follows: the branches for transitions for which $\Delta J = -2, -1, 0, 1, 2$ are called the O-, P-, Q-, R- and S-branches [75]. The vibrational branch line-widths are thus also called Q-branch line-widths.

The use of the vibrational spectrum as a probe has been implemented [47, 6] but found lacking in its ability to accurately determine the temperature. It is the behaviour of the line at high pressure and temperature where the entire spectrum collapses into a single line (motional narrowing) which makes this technique difficult to successfully implement. An alternative is to measure the rotational spectrum for a particular vibrational band. The rotational spectrum is much better behaved at high pressure and temperature. The rotational spectrum is actually less sensitive to the temperature variation than the vibrational band. It is the magnitude of the sensitivity of the vibrational band to the temperature variation that actually inhibits the technique.

The complications introduced stem from broadening effects at high temperature and pressure. These effects make spectral analysis complicated. The different transition ranges for the vibrational and rotational bands lead to

different manifestations of pressure broadening. Specifically rotational bands do not suffer from the effect of motional narrowing.

In the case of temperature diagnostics in a piston chamber, where air from the atmosphere is admitted to the chamber, there is a large amount of N_2, as 79% of the atmosphere is N_2. N_2 is inert, making a temperature measurement using N_2 an average temperature measurement of the medium.

1.3 Experimental

This thesis is not experimental in nature but will make a contribution to what is largely an experimental field. The various forms of the basis rates form a set of possible bases on which to build a line-width model. Given a line-width model the natural extension is the calculation of spectra. The main focus here is to evaluate the various forms of the basis rates. For completeness the resulting parameters will be used to calculate line-widths and then full spectra which can be compared to experimental spectra.

Firstly the unknown parameters in the various basis rate models must be determined. This requires experimental data which the model can be fitted to. For this purpose experimental line-width data for both rotational and vibrational transitions has been provided, kindly, by our French colleagues. This data includes for the first time rotational line-widths and thus allows the ability of the various basis rates for different and combinations of data sets to be analysed.

Once this has been done spectra will be produced which can be compared with experimental spectra kindly provided by our Swedish colleagues. The spectra provided are at all room temperature but cover a range of pressures (1 - 90 bar). The provided spectra are measured using dual-broadband CARS.

1.4 Motivation

Dual-broadband CARS allows the measurement of a complete spectrum on a very short time scale ($\sim ns$). The technique is an optical one which generates a coherent signal giving a good signal to noise ratio.

The nature (spatio-temporal resolution and coherence) of the technique makes it useful where other techniques fail. Specifically when the temperature changes on timescales comparable to those of spectral measurement or in cases where a physical probe would alter the behaviour or reaction in such a way that the that the temperature readings would be meaningless.

This work will form part of a project which will ultimately use spectra

measured from diatomic nitrogen in a piston chamber. Temperature readings will be taken at different stages during the combustion process. CARS is useful for a number of reasons. Firstly, for a thermocouple to make a temperature measurement the thermocouple must be in thermal equilibrium with the medium whose temperature is being measured. In the case of temperature diagnostics in a piston chamber the combustion process takes place too fast for a thermocouple or similar temperature measuring device to achieve thermal equilibrium. The shape of a piston chamber also affects the mixing of the fuel and gas. To place a device in the piston chamber would affect the mixing and thus temperature measurements, should it be possible to take them, would not represent the true temperatures of a working engine where the obstruction no longer exists and therefore no longer affects the mixing. The short time scale also allows temperature measurements to be taken at various stages of the combustion process allowing the temperature evolution to be calculated.

In addition the technique has good spatial resolution in addition to the good temporal resolution. The spatial resolution is of function of the coherence length of the laser beams used in the technique.

Here needs to be some argument as to why it is a useful technique to have available to industry.

Chapter 2

Theory

2.1 The Raman Effect

This effect, named after the Indian scientist C. V. Raman, is characterized by the scattering of electromagnetic radiation, of incident frequency ν_0, by a medium at a frequency $\nu_0 \pm \nu_C$, where ν_C is some characteristic frequency of the medium. This characteristic frequency corresponds to an electronic, rotational or vibrational transition of the constituents of the medium. The effect was first observed by C. V. Raman and K. S. Krishnan in liquids in 1928 [1].

Together, frequency shifted lines, one for each ν_C, constitute a Raman spectrum. A spectrum of lines shifted to higher frequency is termed an Anti-Stokes Raman spectrum, while those lines shifted to lower frequency constitute a Stokes Raman spectrum. The intensity of the lines in the spectrum is proportional to the population differences between the states involved in the transition. The intensity of the Anti-Stokes Raman spectrum decreases rapidly with increasing frequency or wavenumber as the population of energy states decreases exponentially with increasing energy [2].

Spontaneous Raman scattering is always accompanied by spontaneous Rayleigh scattering. In Rayleigh scattering the scattering centre is small compared to the wavelength of the radiation being scattered. The relative intensity of Raman to Rayleigh scattering, although exhibiting complex dependence on conditions, is typically $\sim 10^{-3}$ [2].

Spontaneous Raman scattering is, however, much less effective for spectroscopy in luminous reactive media than the third order non-linear optical technique for performing stimulated Raman spectroscopy called Coherent Anti-Stokes Raman Scattering (CARS) [4]. This third order non-linear technique relies on a four wave mixing process. It was first observed by Maker

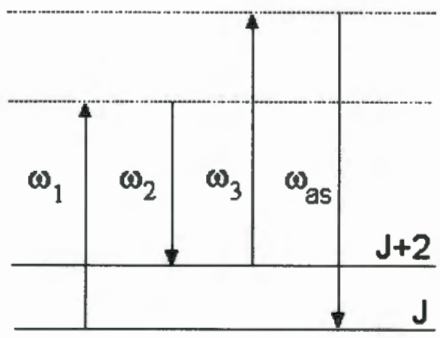

Figure 2.1: An energy level representation of the stimulated Anti-Stokes Raman effect

and Terhune [5] in 1965.

2.2 CARS

When the induced polarisation of a centro-symmetric medium responding to an applied electric field consisting of several harmonic components is considered, it is found to contain terms which resonate at various combinations of the harmonics of the applied electric fields. Each of these polarisation terms acts as a coherent source of radiation. In particular, terms occur corresponding to a polarisation at some frequency which results in a Stokes or Anti-Stokes signal. The use of lasers to induce such polarisation terms results in what is known as the stimulated Raman effect. It is the coherent nature of the effect which makes it an attractive method for measuring spectra.

Traditionally, in CARS, there are two applied electric fields (incident laser beams), one referred to as the pump laser and the other as the Stokes laser. The pump laser is of higher intensity and is maintained at a constant frequency. The Stokes laser is usually of lower intensity and is often tunable or a broadband dye laser, depending on the specific application. Combinations of the frequencies, through the third order polarisation, give rise to the signals corresponding to the various effects, one being the Anti-Stokes Raman effect (CARS); another the Stokes Raman effect (CSRS). The energy level representations of the origin of the Stokes- and Anti-Stokes signal are given in figures 2.2 and 2.1 respectively.

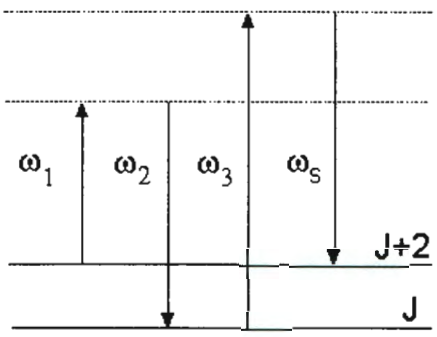

Figure 2.2: An energy level representation of the stimulated Stokes Raman effect

The atom or molecule which is undergoing the transitions can couple more than once to the same radiation field. Therefore it is possible to stimulate the Raman effect with two lasers. All that is required is that two of the transition frequencies be identical (from the same radiation field) typically in the case where just two lasers are used. This is not always the case and another case will be described later. The simplest case is when both lasers are single longitudinal mode devices; they both produce radiation at only one frequency.

In the case of only a pump and Stokes laser, ω_1 and ω_3 both belong to the pump laser. By scanning ω_2 (the Stokes laser) through a range of frequencies, various transitions can be probed and a spectrum built up. Alternatively, a number of different ω_2's can be applied simultaneously, as in the case of the use of a broadband dye laser as the Stokes laser. This is useful when there is insufficient time for the variation of the Stokes laser for the compilation of a spectrum, as in the application of temperature diagnostics in a piston chamber.

In the cases where one of the lasers is not a single longitudinal mode device, the multiple frequency nature of the laser must be accounted for. Such a treatment can be found in [50] and references contained therein.

In applications where time resolution is required or there is insufficient time for the variation of the Stokes laser to generate a spectrum, a broadband Stokes laser can be used. A broadband laser can, simply put, be seen as the simultaneous application of Stokes laser beams at multiple frequencies. This

allows many transitions to be probed at once. An entire spectrum can be built in a single pulse if a pulse pump and Stokes laser are used.

The standard practice is to use a broadband dye laser however, there is one issue which needs to be considered. There is a large shot-to-shot variation in the intensity profile of a broadband dye laser. Thus single shot spectra are not reproducible. If two broadband dye lasers are used then there is an averaging over the breadth of the dye lasers.

Writing the applied electric fields as a sum of plane waves all travelling in the $\overrightarrow{k}$ direction

$$\mathbf{E}(\overrightarrow{r},t) = \sum_{j=-N}^{N} \mathbf{E}_j(\overrightarrow{r},\omega_j)e^{i(\overrightarrow{k}_j\overrightarrow{r}-\omega_j t)}, \tag{2.1}$$

where the k's and ω's can be negative (when j is negative) and we have that $\mathbf{E}(\overrightarrow{r},-\omega_j) = \mathbf{E}^*(\overrightarrow{r},\omega_{-j}) = \mathbf{E}^*(\overrightarrow{r},\omega_j)$. The polarisation, when expanded in terms of its harmonic components, is written as:

$$\mathbf{P}(\overrightarrow{r},t) = \sum_{k=-M}^{M} \mathbf{P}_k(\overrightarrow{r},\omega_k)e^{i(-\omega_k t)}, \tag{2.2}$$

where the same convention as for equation 2.1 applies.

The induced polarisation in the third order can be written as [4, 5]

$$\begin{aligned}\mathbf{P}^{(3)}(\overrightarrow{r},\omega_{AS},t) &= D\chi^{(3)}(\omega_{AS},\omega_1,\omega_2,\omega_3)\times \\ &\mathbf{E}_1(\overrightarrow{r},\omega_1)\mathbf{E}_2(\overrightarrow{r},\omega_2)\mathbf{E}_3(\overrightarrow{r},\omega_3)e^{i(k_1+k_2+k_3)},\end{aligned} \tag{2.3}$$

where $\chi^{(3)}$ is a tensor and is the third order non-linear susceptibility and $-\omega_{AS} = \omega_1 + \omega_2 + \omega_3$. D is a linear factor that comes from symmetry properties of the tensor. This induced polarisation acts as a source whose result is a solution of [6]:

$$\left(\nabla^2 + \frac{1}{c^2}\frac{\partial^2}{\partial t^2}\right)E_s(\overrightarrow{r},t) = -\frac{4\pi}{c^2}\frac{\partial^2}{\partial t^2}\mathbf{P}^{(3)}(\overrightarrow{r},\omega_{AS},t). \tag{2.4}$$

The source is subject to phase matching conditions and acts as a coherent source of electromagnetic radiation.

In dual-broadband CARS, two broadband dye lasers are used and the rotational Raman transitions in the molecule are coherently excited by multiple pairs of photons, one from each dye laser, which have a frequency difference corresponding to the transition being probed, before coupling to photons from the pump laser [12].

2.3 The Third-order Susceptibilities

To predict the CARS spectrum given the applied electric fields (which are applied through the use of lasers at various frequencies) and knowledge of the constituents of the medium, requires calculation of $\chi^{(3)}$ for various frequencies. This procedure requires knowledge of the density matrix. Molecular motion complicates the calculation of the density matrix in gases. Following the treatment shown in [4], we have that the density at some position $\vec{r}$ in the medium is given by

$$\rho(\vec{r},t) = \int \rho(\vec{r},t,\mathbf{v})F(\mathbf{v})d^3\mathbf{v} \tag{2.5}$$

where $\rho(\vec{r},t)$ is the solution of the density operator evolution equation in the laboratory frame, and $F(\mathbf{v})$ is the velocity distribution. The density operator is described by the Liouville equation:

$$i\hbar\dot{\rho} = [H_0 + H_{int}, \rho] + i\hbar\Gamma\rho \tag{2.6}$$

where H_0 is the unperturbed Hamiltonian for the system and H_{int} is the Hamiltonian representing the dipole interaction with the applied field. Γ represents the Raman width of the line and can be thought of as the rate at which the system relaxes to equilibrium.

The expectation value of the density operator is then found by expanding ρ as a perturbation expansion as follows:

$$\begin{aligned} i\hbar\dot{\rho}^{(0)} &= [H_0, \rho^{(0)}] + i\hbar\Gamma\rho^{(1)} \\ i\hbar\dot{\rho}^{(1)} &= [H_0, \rho^{(1)}] + [H_{int}, \rho^{(0)}] + i\hbar\Gamma\rho^{(1)} \\ i\hbar\dot{\rho}^{(n)} &= [H_0, \rho^{(n)}] + [H_{int}, \rho^{(n-1)}] + i\hbar\Gamma\rho^{(n)} \end{aligned} \tag{2.7}$$

The result obtained for the net third order polarisation is:

$$\mathbf{P}^{(3)}(\vec{r},\omega_{AS},t) = N\mathbf{Tr}\left[\rho^{(3)}(\vec{r},\omega_{AS},t)\mu\right] + c.c. \tag{2.8}$$

where μ is the dipole operator and **Tr** refers to taking the trace of $\rho^{(3)}(\vec{r},\omega_{AS},t)\mu$. $\rho^{(3)}$ is obtained from (2.7). The resulting expression for $\chi^{(3)}$ has 48 terms. From these it is possible to group those that satisfy the correct resonance conditions for various non-linear effects.

The final expression for $\chi^{(3)}_{CARS}$ can be written relatively simply, if each of the three frequencies is away from electronic resonance and if the assumption that the rotational spectral lines are well separated in frequency space is made. This is done by relating the Raman polarizability elements which occur, to the Raman scattering cross-sections. The resulting expression is:

$$\chi^{(3)}_{CARS} = \chi_{NR} + \sum_{ij} \frac{\varepsilon^4}{4\hbar\omega_s^4} \frac{N_i - N_j}{\omega_{fi} - \omega_p + \omega_s - i\Gamma_{fi}} \left(\frac{d\sigma_{fi}}{d\Omega}\right), \tag{2.9}$$

where $\left(\frac{d\sigma_{fi}}{d\Omega}\right)$ is the differential Raman scattering cross-section. It is convenient to write $\chi^{(3)}_{CARS}$ as follows

$$\chi^{(3)}_{CARS} = \chi_{NR} + \sum_{if} \frac{a_{if}}{\omega_{fi} - \omega_p + \omega_s - i\Gamma_{fi}} \left(\frac{d\sigma_{fi}}{d\Omega}\right). \tag{2.10}$$

The terms that contribute to the Stokes signal can also be grouped and are given by:

$$\chi^{(3)}_{CSRS} = \chi_{NR} + \sum_{if} \frac{a_{if}}{\omega_{fi} - \omega_p - \omega_s - i\Gamma_{fi}} \left(\frac{d\sigma_{fi}}{d\Omega}\right). \tag{2.11}$$

The term χ_{NR} can be thought of as the contribution from all the terms which are not in resonance. These contributions come from transitions involving only virtual states and so are suppressed [73, 74]. The primary physical difference between the two physical processes is that in CARS the transitions are from J to $J+2$, while in CSRS they are from J to $J-2$. This expression (equation 2.11) has been included because there is a coupling between the CARS and CSRS bands which must be included under certain circumstances [44]. In general the phase matching conditions that optimise the CARS signal will not optimise the CSRS signal. It has been shown [44] that a significant CSRS contribution can be generated when perfect phase matching for the CARS signal exists, if the coherence length of the CSRS generation is longer than the interaction length of the volume where the beams are interacting.

2.4 CARS Spectrum

The CARS intensity profile will be proportional to $|\chi^{(3)}_{CARS}|^2$ which implies that

$$I(\omega) \propto \chi^2_{NR} + \chi_{NR}\left(\chi^{(3)}_{RES} + \chi^{*(3)}_{RES}\right) + |\chi^{(3)}_{RES}|^2, \tag{2.12}$$

where

$$\chi_{RES} = \sum_{if} \frac{a_{if}}{\omega_{fi} - \omega_p + \omega_s - i\Gamma_{fi}} \left(\frac{d\sigma_{fi}}{d\Omega}\right). \tag{2.13}$$

There are circumstances under which the influence of the non-resonant background is suppressed. Then it is possible to calculate only $|\chi^{(3)}_{CARS}|^2$ when calculating a spectrum and neglect entirely terms in χ_{NR}.

Another possible complication is the coupling between the Stokes and Anti-Stokes bands in the rotational spectrum. In the case of vibrational CARS, the bands are far enough removed that the coupling is negligible. In

the rotational case, at sufficiently high pressures, the coupling contribution must be included to reproduce the experimental spectra accurately [44]. This implies that the spectrum to be calculated is best represented by

$$I(\omega) \propto |\chi_{NR} + \chi^{(3)}_{RES\ CARS} + \chi^{(3)}_{RES\ CSRS}|^2. \tag{2.14}$$

Once the effective third order non-linear susceptibility is known, calculation of the actual spectrum can take place. It should be noted that in experiment the intensity contour that is measured is not detector independent. The instrument function of the detector alters the spectral profile and this must be accounted for. In addition to this, the laser intensity profile also influences the spectral profile. The complete spectral profile is then the intensity profile convoluted with the laser profiles as well as the instrument function.

A complete expression for the final measured intensity contour, which only needs to be convoluted with the instrument function, is

$$I(\omega) = K \int\int\int |\chi^{(3)}(\omega)|^2 I_1(\omega_1) I_2(\omega_2) I_3(\omega_3) d\omega_1 d\omega_2 d\omega_3, \tag{2.15}$$

where $I_i(\omega_i)$ describes the intensity profiles of the interacting laser beams.

This expression can be simplified in specific cases once the laser intensity profiles have been specified. This is experiment-specific and no general simplified expression is possible. The optimal situation would be broadband lasers with a step function profile and a pump laser with a Dirac delta function profile. In this case the contributions from the laser profiles would be a multiplicative constant and all that would need to be calculated is $\chi^{(3)}(\omega)$.

2.5 Spectral Effects of Pressure and Temperature

The first and simplest effect of temperature is that it determines the average velocity of the molecules in the medium. It is the random distribution of the velocities of the particles about some mean value that results in slight shifts of energy (Doppler shift) and thus broadening of the peak in the measured spectrum.

As pressure and temperature increase, the frequency of collisions between radiating molecules increases. The collision between a perturber and radiating molecule can result in a change in frequency or phase of the radiation, or even both. It is the nature and frequency of these changes that results in pressure broadening.

Motional Narrowing, which is quite spectacular, occurs when the transition frequency between states is comparable to the frequency of the radiation corresponding to that particular transition. This effect is particularly noticeable in the vibrational (Q-branch) spectrum of diatomic nitrogen as density increases [7, 8]. It is possible for the entire spectrum to broaden, overlap and then collapse into a single line as the pressure and temperature are increased. If both direct dephasing and rotational-vibrational (RV) coupling are present, then it is possible for the line-widths to be narrower than in the case where there is no RV coupling. It is at near liquid densities that the direct dephasing cannot be ignored. Theories ignoring direct dephasing can only apply to lower density substances.

A detailed treatment of this phenomenon in terms of the Gordon J-diffusion model can be found in [7]. It has also been expressed in a relaxation matrix formalism in [8].

An explicit derivation of a model using the Gordon J-diffusion model and certain explained approximations which is able to produce the motionally narrowed isotropic Raman Q-branch profile can be found in [54] and is most enlightening.

It is motional narrowing that makes it particularly difficult to use vibrational CARS for temperature diagnostics. It is not that the spectrum is not sensitive to high pressure and temperature, but rather that it is too sensitive.

The Gordon J-diffusion model assumes that the probability of moving from state k to any other state j is the same. The state is completely thermalised in the collision, making the probability of going to that level the same as the thermal probability of that level.

The relaxation matrix formalism uses the time dependent perturbation approach to the solution of the density matrix because this model can be applied to both reorientation and vibrational dephasing and so is able to predict both isotropic and anisotropic Raman widths.

Pressure broadening is the overall effect that the collisions of the particles have on each other.

2.6 Pure Rotational Dual-Broadband CARS

It is the implementation of the technique of pure rotational dual-broadband CARS which is the ultimate goal of the project to which this document is contributing. In rotational dual-broadband CARS the rotational transitions in a vibrational band are probed. There are a number of advantages to this but they all carry with them certain constraints as detailed below. The primary alternative to pure rotational dual-broadband CARS is vibrational

CARS, so it is the choice of the one above the other that requires justification.

Vibrational CARS spectroscopy, although more sensitive at high temperature than pure rotational dual-broadband CARS spectroscopy [12, 14], suffers from motional narrowing, first observed in N_2 by Varghese [11]. This effect occurs when the inelastic collision rates between rotational states are comparable to the vibration-rotation splitting of the corresponding Q-branch transitions, and results in narrowing of the Q-branch spectrum [6, 9, 10, 12, 7, 8]. At high enough pressure, the entire Q-branch spectrum collapses completely into a single line but even at low pressure the motional narrowing effects are not necessarily negligible.

The lower sensitivity of rotational CARS compared to vibrational CARS does not cripple the technique as sufficient signal intensity is still generated, as described in [13] even at flame temperatures.

The spacing of the rotational lines is such that there is none of the complex analysis of overlapping lines that accompanies the theoretical calculation of Q-branch spectra for vibrational CARS [12]. This also allows the instrument function to be unambiguously determined from the spectrum.

A number of molecules have their rotational bands falling in a common frequency range which is comparable to the frequency range of a broadband dye laser pulse. This allows the simultaneous collection of spectra with data corresponding to a number of different molecules [12, 14, 15], allowing the relative populations to be calculated through the relative intensity of the different rotational bands.

Rotational bands also have Raman cross-sections typically of the order of an order of magnitude greater than vibrational Raman cross-sections [12].

The rotational bands are less susceptible than the vibrational bands to changes in the value of χ_{NR} [14]. A factor of 5 change in χ_{NR} for spectra taken at 2000K leads to only a 1% change in the value of the estimated temperature while in the case of vibrational CARS, this change leads to a variation of 30% [13]. χ_{NR} can undergo large changes in fuel rich and sooty environments [13] which also strengthens the argument for the use of rotational CARS.

However, there are some disadvantages to using rotational CARS. Raman spectroscopy probes population differences between different states. As one moves to higher energy, one finds that population differences go to zero in the rotational populations [12]. Thus the intensity of this signal must go to zero as temperatures become relatively high, that is greater than 1600K [12]. In the specific case of combustion diagnostics, temperatures are not expected to exceed 1000K. It has been shown that the standard deviations on temperature calculations using rotational CARS, as opposed to vibrational CARS, are smaller below 1000K [12, 14]. Detailed calculations for standard deviations can be found in reference [14] where, up to 1200K, rotational

CARS is shown to be significantly better than vibrational CARS.

The choice of a dual-broadband setup allows an averaging process [12] even in the case of single shot spectra. As long as the transition being probed corresponds to a transition of lower frequency than the width of the broadband pulses, there will be an averaging over the two broadband pulses. This allows much improved statistics [12, 13, 15] and there is theoretical and experimental evidence to support lower signal to noise ratios for this configuration than for a large number of different configurations [13]. In the case of pure rotational dual-broadband CARS, it is possible for the spectral noise of the generated spectrum to be less than that of the sources generating the signal.

On the whole, the rotational spectrum is simpler to calculate and has better signal to noise ratios than vibrational CARS [12].

2.7 Lineshapes

The central problem in temperature or species diagnostics is the accurate calculation of theoretical spectra. These calculations are based on an intimate knowledge of the behaviour of the species being probed.

Knowledge of the lineshapes of the various transitions making up the Raman spectrum of N_2 is required. Essentially it is the spectrum of a radiating dipole undergoing almost constant collisions with neighbouring molecules [16]. There will be both strong and weak collisions which result in both changes in phase of the radiating molecule and complete interruptions with changes in frequency. This is the problem of pressure broadening as stated in section 2.5.

The lines undergo broadening which is dominated by collision broadening. The collision broadening is dominated by self-broadening. Collisions with other molecules have been considered (see [51] and references therein). The effects of these collisions will be neglected which can be justified simply by the abundance of N_2. The issue of self-broadening is further complicated by the fact that the lines overlap which must be accounted for in the theory.

The problem can be stated quite simply as the solution of Schrödinger's equation given as follows

$$\{H_1(t,r) + H_2(t,r) + V_{12}(t,r) - E\}\psi = 0, \tag{2.16}$$

where $H_1(t,r)$ is the internal Hamiltonian of molecule 1, $H_2(t,r)$ is the internal Hamiltonian of molecule 2, and $V_{12}(t,r)$ is the potential of the interactions between them.

This problem is difficult to solve because the form of the potential interaction between the two molecules is not known and the internal Hamiltonians are not known exactly. The solution to the problem is, in principle, given by the Lippmann-Schwinger equation [22, 23, 27, 26]

$$\begin{aligned}\psi_{\mathbf{k}_{j_0}}(j_0\lambda_0|\mathbf{R}\hat{\rho}) &= e^{i\mathbf{k}_{j_0}\mathbf{R}}Y_{j_0\lambda_0}(\hat{\rho}) - \frac{2M}{\hbar^2}\sum_{j\lambda l\mu} k_j Y_{j\lambda}(\hat{\rho})Y_{l\mu}(\hat{\mathbf{R}}) \\ &\int d\mathbf{R}'d\hat{\rho}'Y^*_{j\lambda}(\hat{\rho}')Y^*_{l\mu}(\hat{\mathbf{R}}')V(\mathbf{R}'\cdot\hat{\rho}')h_l^+(k_jR_>) \\ &j_l(k_jR_<)\psi_{\mathbf{k}_{j_0}}(j_0\lambda_0|\mathbf{R}'\hat{\rho}'). \qquad (2.17)\end{aligned}$$

The transition matrix must obey the Lippmann-Schwinger equation [22, 23, 26, 27]. The complexity of the entire problem naturally leads to a hierarchy of assumptions and approximations which, through developments over the years, have led to much improved predictive power in line-width models and thus better agreement between theoretically predicted and experimentally measured CARS spectra.

2.7.1 Early Work

There has been a large amount of work on the topic of pressure broadening of spectra, as well as on the calculation of scattering matrix elements. There are essentially three different approaches to the calculation of line-widths. One is the direct inversion of experimentally measured widths and shifts in terms of scaling relationships [29]. There is the perturbative approach, beginning with the pioneering work of Anderson [16], and then it is also possible to calculate the widths and shifts from accurate calculations of the S-matrix.

The most broadly applied theory of pressure broadening is that of Anderson [16]. Anderson worked in the microwave and infra-red regions. He dealt only with the isolated spectral lines of a radiating molecule using a perturbative approach in the impact and classical path approximations. Anderson's formalism can be used to solve the Debye case (i.e. the case of a freely rotating molecule).

Making the classical path approximation involves assuming that the path of the perturber need not be treated quantum mechanically [16] and thus the path of the perturber is a well defined function of time and so is the Hamiltonian. Various path models have been attempted which amounts to making an assumption about the form of the potential. In the impact approximation, the assumption that the duration of the collision is much shorter than the time of observation is made. A criterion for this is that the strong collisions are completely disentangled i.e. no two strong collisions occur at the same

time [39]. Discussion of the validity conditions of the impact and classical path approximations can be found in [16, 18].

Baranger [18, 19, 20] worked on the perturbation by electrons where the interaction, which fluctuates in time, is replaced by an effective interaction [19, 20] in the impact approximation. It is important to note that electrons are light perturbers and Baranger was working in the context of atomic rather than molecular spectroscopy. Baranger extends his theory to overlapping lines in [19] and shows that Anderson's solution for isolated lines can be reproduced in the limit of small overlap. In [30] rotational degeneracy is also accounted for.

The work is developed further (in a transparent way) by Fiutak and van Kranendonk [20, 17] in which Anderson's theory is extended to the Raman spectrum. The electric dipole scattering for freely rotating molecules can be decomposed into three parts corresponding to the $K = 0, 1, 2$ irreducible parts of the Raman tensor. These parts are termed the isotropic, magnetic dipole and electric quadrupole (anisotropic) parts respectively. These names are given to distinguish the various transformation properties rather than the type of radiation. Initially, lines belonging to the different irreducible parts of the Raman tensor were regarded as not interfering with each other [17, 21, 22]. The calculations of the S-matrix are presented for dipolar, quadrupolar [21, 55] and anisotropic intermolecular [21] forces.

As long as the scattering is non-resonant, the lines will have a Lorentzian shape [16, 17, 20].

Two different approaches to characterising the line-widths developed. The statistically based fitting laws, at a given temperature, assume that the rotational relaxation rates depend only on the energy gap between rotational levels. Any other dependence is contained in a statistical factor. Here the entire relaxation matrix is characterised by the parameters contained in the fitting law and no appeal is made to any physical meaning [10]. These laws must include a monotonic decrease in the line-width as J increases. Thus they exhibit some sort of decay. This can be achieved through an exponential or reciprocal polynomial component. This gives rise to various forms of these gap laws, termed exponential gap law (EGL) or polynomial gap law (PGL), depending on how the monotonic decrease is achieved.

The previously mentioned statistical fitting laws, which depend on the energy transferred and are commonly termed gap laws [30], can be used to characterise the set of basis rates. The PGL has in it a dependence on $\left(\frac{1}{j(j+1)}\right)^{\gamma}$. The EGL contains $e^{-\beta\Delta E}$, where ΔE is the energy difference between the states [30, 10], to characterise the decrease in line-width at high J. The combined form, the PEGL, has been shown to contain more

parameters than can reasonably be fitted [66].

There is also a more complicated (in terms of free parameters) law where both the exponential and the polynomial forms are combined. This is the polynomial exponential gap law (PEGL). These laws have not been wholly unsuccessful [49, 33] but are far removed from any physical explanation of the widths, although they have received some justification from information theory [65].

These laws will not be used for the complete characterisation of the line-widths here, but they will be used to characterise the basis rates which do form a part of the line-width model to be used.

Another method is to introduce various approximations into the problem and to develop the dynamically based fitting laws. In the coupled states (CS) approximation, the l^2 operator in the Lippmann-Schwinger equation is replaced by the effective eigenvalue $l(l+1)\hbar^2$ [25, 27]. A simple form of the potential is used. This amounts to conservation of the z-component of the angular momentum in the collision. Explanations of how angular momentum coupling can be removed are found in [25, 27, 24]. The infinite order sudden (IOS) approximation is essentially the sudden approximation to the coupled states approximation and in it the j^2 operator is replaced by the effective eigenvalue $j(j+1)\hbar^2$. This is equivalent to replacing the actual wavenumber by an effective wavenumber [27, 26]. These approximations remove coupling, thus allowing the use of closure relations for the summations over the infinite sets of functions rather than, as done previously, the truncation of the sets [27]. A detailed development of the relationship between the CS and IOS approximations can be found in [27]. It is also important to note that certain energy level differences have been neglected and this can become a problem at kinetic energies on the threshold of the energy differences that have been neglected [26].

It is convenient to note that the cross-sections can be factorised into basis rates and dynamical coefficients in the context of the IOS approximation [29, 26]. The dynamical coefficients have been shown to be equal to the inelastic cross-section for the transition $j = 0 \longrightarrow j = l$ and thus they are, essentially, basis rates [26] and will be referred to as such. These basis rates occur in the calculation of the transition matrix elements as well. They do not depend on the dynamics of the system being calculated. This means that a set of measurements of a certain cross-section can be used to fully characterise the basis rates. Once this has been done, these basis rates can be used in the calculation of any type of cross section. This means that only the dynamical coefficients need to be calculated [26, 29], giving a scaling law for calculating all rates in terms of the basis rates. These are the fitting laws and the scaling laws.

The fitting laws attempt to predict the widths in terms of a number of parameters, while the scaling laws attempt to find a relationship between a subset of measured widths and the remaining, unknown widths. Explanations and comparisons of a large number of scaling and power laws can be found in [30, 27, 57].

The spectroscopic coefficients can be calculated theoretically [27] and so, if a proper understanding of the basis rates is achieved, the problem of calculating pressure broadened line-widths is solved. At this stage there are two problems worth considering. How should the basis rates be characterised? Are there any improvements that can be made to the IOS approximation to bring predictions closer to experiment?

2.7.2 Ideas Consolidated

Here it is worth first considering any corrections that can be made to the IOS approximation, as these are independent of the form chosen for the basis rates. The IOS scaling law depends only on the energy sudden approximation and that the coupled states approximation is not required. There have been a number of papers comparing the various aspects of the different forms of the basis rates [33, 34, 35, 36, 37, 38].

The form of the basis rates is of paramount importance to the success of the model, whether it be IOS or ECS. In the IOS approximation, the inelastic transition rates are given by

$$W^{IOS}_{j_i,j_f} = (2j_f+1)e^{-\frac{E_{j_f}-E_{j_i}}{kT}} \sum_{\lambda} \begin{pmatrix} j_i & j_f & \lambda \\ 0 & 0 & 0 \end{pmatrix}^2 (2\lambda+1)Q_\lambda, \qquad (2.18)$$

where (:::) denote 3-j symbols and the Q_λ are the basis rates. The $(2j+1)$ factors account for the degeneracy. The factors preceding the summation guarantee that detailed balance is satisfied i.e. the population distribution remains consistent despite the constant transitions, or simply put, there is no accumulation in a state beyond that predicted by the thermal population distribution.

When the translational and rotational energy are of the order of k_BT, the sudden approximation is no longer valid and a correction for the adiabatic effects needs to be made [30]. This adiabaticity correction accounts for the fact that the two states involved in the transition are affected differently by the perturber. The addition of an adiabatic factor leads to the energy corrected sudden approximation (ECS). A derivation of the ECS model, in the context of S-matrix calculations and applied to $H^+ - CN$ systems, can be found in [64]. The ECS theory has been shown to describe accurately

rotation-rotation,translation- and vibration-vibration, rotation, translation energy transfer processes [29, 10]. By accounting for energy gaps and not restricting the number of spectral lines, the ECS approximation extends the ability of the IOS approximation [29]. The improvement comes from the inclusion of the adiabaticity factor. This accounts for the finite duration of the collision [6]. The ECS model does not admit an analytic solution to the collisional problem but does yield an analytic scaling relationship [29]. A detailed explanation of the properties of the cross-sections derived using the ECS model can be found in [29]. The ECS model gives, like the IOS model, the rates for a transition in terms of angular momentum coupling coefficients and the basis rates. The expression in [30, 46] for the ECS scaling law is

$$W^{ECS}_{j_i,j_f} = (2j_f+1)\Omega_{j_>} e^{-\frac{E_{j_>}-E_{j_i}}{kT}} \sum_{\lambda} \begin{pmatrix} j_i & j_f & \lambda \\ 0 & 0 & 0 \end{pmatrix}^2 (2\lambda+1)\frac{Q_\lambda}{\Omega_\lambda}, \qquad (2.19)$$

where Ω_λ is an adiabaticity factor.

$$\Omega_\lambda = \frac{1}{\left(1+\frac{\omega^2_{\lambda,\lambda-2} l_c^2}{12n\overline{v}}\right)}. \qquad (2.20)$$

The role of the adiabaticity factor is to correct for the fact that, in the sudden approximation, the rotation of the perturbed molecule has been neglected. An argument for the actual form of the adiabaticity factor can be found in [30]. It is characterised by the rotational frequency of the state and an average collision length [29]. It is also assumed that the perturbers can be well treated using an average velocity $\overline{v}$ [16] which is

$$\overline{v} = \sqrt{\frac{8k_B T}{\pi\mu}}. \qquad (2.21)$$

In this case μ is the reduced mass of the perturbing molecule.

The size of the set of Q_λ required to be able to make spectral calculations at sufficiently many temperatures for temperature diagnostics is too large for practical purposes. Thus a fitting law for the basis rates is required. Then experimental data can be used to fit a small number of parameters which will be used to generate all the basis rates.

The basis rates, for a given temperature, can be described as either

$$Q_\lambda = A(T)\left(\frac{1}{\lambda(\lambda+1)}\right)^\gamma, \qquad (2.22)$$

in the case of the polynomial gap law, or

$$Q_\lambda = A(T)e^{-\beta\frac{\hbar\omega_\lambda}{k_B T}}, \qquad (2.23)$$

in the case of the exponential gap law. These basis rate expressions result in the ECS-P and ECS-E laws respectively.

These laws can be further combined, first proposed in [30], to produce what is termed the ECS-EP fitting law where the expression for the basis rates, in the context of the current work [38], is

$$Q_\lambda = A\left(\frac{1}{\lambda(\lambda+1)}\right)^\gamma e^{-\beta\frac{\hbar\omega_\lambda}{k_B T}}. \tag{2.24}$$

It is, in fact, possible to utilise any of the basis rate expressions to produce IOS-P, IOS-E and IOS-EP fitting laws, but it has been shown that the ECS fitting laws are much better suited, especially in heavier gases, to reproducing experimental results [30, 46, 33]. Furthermore the exponential gap law outperforms the polynomial gap law [33, 10]. Detailed comparisons of these laws with each other and the experimental data, in most cases N_2 but also other molecules in ternary mixtures, can be found in [30, 32, 31, 33, 36, 38, 46, 61, 62]. In this work both the polynomial and exponential basis rate forms will be compared for completeness.

2.7.3 Recent Work

In [10], the strong collision (SC) model, which is based on the Gordon J-diffusion model, is compared with the various statistically based and dynamically based fitting laws. The SC model is derived by imposing thermal population probabilities as transition probabilities and imposing the unitarity of the S-matrix. The validity of this model increases as temperature increases. Exact expressions for the SC model can be found in [52].

Under the influence of heavy perturbers, the linear line mixing of the light molecules is absent [46]. This results in the deviation from the Lorentzian lineshape. A new theoretical approach to the problem of line coupling is developed in [46]. This leads to an ECS model which obeys all sum rules and detailed balance.

The coupling between bands is affected by the angular momentum coupling. The entire set of line-widths, lineshifts and interband coupling can be combined and presented as a tetradic supermatrix [56]. It is the work of Bruet which extends the ECS model on strong physical grounds and includes angular momentum coupling effects [63, 41]. In previous work the tetradic supermatrix was expanded in terms of the dyadic mechanical cross sections [63] which required new parameters in the off-diagonal matrix elements. Bruet *et al.* deliver a new approach to the calculation of the isotropic and infra-red branches on a physical basis which removes the need for any parameters beyond those characterising the basis rates.

In addition it is shown that a four parameter form of the basis rates i.e. using only an exponential or a polynomial but not both, is sufficient for modeling the data adequately [66, 67, 41] i.e. as accurately, in terms of $\frac{\chi^2}{ndf}$, as a five parameter fit. It also reduces the number of parameters that require fitting.

In light of the work presented in [66, 67], it should be mentioned that the value of n is not necessarily 2 in equation 2.20. A value of 1 has been shown to be more accurate for far infra-red spectra which is not specific to this work. For completeness, fit results using both values of the exponent have been given, allowing the reader access to a more complete set of fit results. The lack of an indisputable argument in favour of one value over the other is the reason for this larger set of results.

This project has been made possible by the recent work in further improving the ECS model. The extension involves the inclusion of relaxation mechanisms that are neglected in the IOS approximation [40, 39]. In [39] the extended ECS model is used for calculations of the infrared band for bending modes but can be applied to other spectroscopic bands like the anisotropic Raman bands [40].

This is further extended by Bruet [41] where he derives the following result

$$\begin{aligned} W^K_{j_i j_f j'_i j'_f} = & \frac{\delta_{j_i j'_i}\delta_{j_f j'_f}}{2}\left(\frac{1}{\tau_{j_i}}+\frac{1}{\tau_{j_f}}\right) - \frac{[j'_i]}{2}\sqrt{[j_f][j'_f]} \\ & \left(\Omega^n_{j_{imax}} e^{-\frac{\hbar\omega_{j_{imax}j_i}}{k_B T}} + \Omega^n_{j_{fmax}} e^{-\frac{\hbar\omega_{j_{fmax}j_f}}{k_B T}}\right) \\ & \sum_\lambda [\lambda] \begin{pmatrix} j_i & j'_i & \lambda \\ 0 & 0 & 0 \end{pmatrix} \begin{pmatrix} j_f & j'_f & \lambda \\ 0 & 0 & 0 \end{pmatrix} \\ & \begin{Bmatrix} j_i & j_f & K \\ j'_i & j'_f & \lambda \end{Bmatrix} \frac{Q_\lambda}{\Omega^n_\lambda} \end{aligned} \tag{2.25}$$

where (:::) denote 3-j symbols and {:::} denote 6-j symbols. The $\frac{1}{\tau_j}$ are given by

$$\frac{1}{\tau_j} = \sum_{j'} [j'] \Omega^n_{j_{max}} e^{-\frac{\hbar\omega_{j_{max}j}}{k_B T}} \sum_\lambda [\lambda] \begin{pmatrix} j & j' & \lambda \\ 0 & 0 & 0 \end{pmatrix}^2 \frac{Q_\lambda}{\Omega^n_\lambda}, \tag{2.26}$$

where $[j] = 2j + 1$ and we have that

$$Q_\lambda = A\left(\frac{T_0}{T}\right)^N e^{-\beta\frac{\hbar\omega_\lambda}{k_B T}}. \tag{2.27}$$

In these equations, ω_l represents the energy of the state with $j = l$. In the application of this model to Raman spectra, the final state j-values are determined by the type of transition being considered and are given by $j_f = j_i + K$, where $K = 0$ for isotropic transitions (Q-branch transitions) and $K = 2$ for anisotropic transitions (S-branch transitions).

The resulting model for the spectroscopic elements of the transition matrix combining both isotropic and anisotropic elements has four free parameters (A, N, β, l_c) which need to be determined from experimental data.

2.7.4 Raman Cross-Sections

The differential scattering cross-sections occur in the expression for $\chi^{(3)}$ and thus need to be determined before any spectral calculations can take place. The differential cross sections are well known and have been shown, for radiation incident along the z-axis and plane polarized along the y-axis, to be [2, 3]

$$\frac{d\sigma_{\parallel}}{d\Omega}(\frac{\pi}{2}) = k'_{\tilde{\nu}}(\tilde{\nu} - \tilde{\nu}_{j',j''})^4 N_{j'} \overline{[\alpha_{zy}]^2_{j',j''}} E_y^2, \tag{2.28}$$

for scattered radiation parallel to the plane of scattering, and

$$\frac{d\sigma_{\perp}}{d\Omega}(\frac{\pi}{2}) = k'_{\tilde{\nu}}(\tilde{\nu} - \tilde{\nu}_{j',j''})^4 N_{j'} \overline{[\alpha_{yy}]^2_{j',j''}} E_y^2, \tag{2.29}$$

for scattered radiation polarized perpendicular to the plane of scattering. Both expressions are for the case where the scattered radiation is at $\frac{\pi}{2}$ to the direction of incidence. The total differential cross-section for scattering at $\frac{\pi}{2}$ to the direction of incidence will be the sum of the two polarisation components shown above.

The average polarizability matrix elements for CARS are given by

$$\overline{[\alpha_{zy}]^2_{j',j''}} = \frac{1}{15} b_{j+2,j} (\gamma)_0^2 \tag{2.30}$$

and

$$\overline{[\alpha_{yy}]^2_{j',j''}} = \frac{4}{45} b_{j+2,j} (\gamma)_0^2, \tag{2.31}$$

where

$$b_{j+2,j} = \frac{3(j+1)(j+2)}{2(2j+1)(2j+3)}. \tag{2.32}$$

These need to be adjusted in the case of CSRS, where

$$\overline{[\alpha_{zy}]^2_{j',j''}} = \frac{1}{15} b_{j-2,j} (\gamma)_0^2 \tag{2.33}$$

and

$$\overline{[\alpha_{yy}]^2_{j',j''}} = \frac{4}{45} b_{j-2,j} (\gamma)^2_0, \tag{2.34}$$

where

$$b_{j-2,j} = \frac{3j(j-1)}{2(2j+1)(2j-1)}. \tag{2.35}$$

The value of $(\gamma)^2_0$ is the anisotropy of the polarizabilty tensor.

2.8 Techniques for Calculation of Spectra

Having the third order susceptibility is tantamount to solving the problem. The calculation is mere labour. It is possible to calculate the spectra using one of two different techniques. The autocorrelation function can be calculated and then Fourier transformed which gives the spectrum in the frequency domain. It is also possible to do a direct calculation of the spectrum in the frequency domain.

2.8.1 Frequency Domain

In the frequency domain $\omega_l - \omega_s$ can be replaced with the frequency for which the spectrum is to be calculated. This variable can be swept over the frequency range of the spectrum to be calculated.

The process of calculating the intensity for a particular value of the frequency involves [43] writing the third order non-linear susceptibility in the following way

$$\chi^{(3)} = -\frac{N}{\hbar} \sum_j \alpha_j \sum_k \alpha_k \Delta\rho_k G^{-1}_{jk}, \tag{2.36}$$

where

$$G_{jk} = \delta_{jk}(\omega_j - \omega_l + \omega_s - i\Gamma_j) + (1 - \delta_{jk}) i\gamma_{jk}. \tag{2.37}$$

The elements of G consist of the transition frequencies in combination with the line-widths. These will be calculated using (2.25). α is the polarisability of a specific transition and is given by

$$\alpha_{if} = \sqrt{\left(\frac{d\sigma}{d\Omega}\right)_{if}} \left(\frac{c}{\omega_s}\right)^2, \tag{2.38}$$

which allows us to return to the equation shown earlier for the third order non-linear susceptibility given in (2.9). Note that the CARS spectrum is proportional to the square modulus of the third order non-linear susceptibility.

This, however, has not accounted for the effect the laser intensity profiles and instrument function have on the spectrum. The lineshapes are Lorentzian which can be seen quite clearly from the form of the equation for $\chi^{(3)}$. The instrument function can have various forms eg. Lorentzian, Gaussian etc. The final, measured experimental spectrum will be the convolution of the laser profiles and instrument function with the spectrum.

The experimental details of the laser intensity profiles for the spectra to be calculated here are given in [69, 44, 45]. The laser profiles and instrument function will be taken as accurate and all that will be changed for the calculation of spectra shown later, is the form of the line-width model used.

2.8.2 Time Domain

It will be argued that it is more convenient to work in the time domain, i.e. in terms of autocorrelation functions, rather than the frequency domain, as shown in [60]. It is useful to illustrate the meaning of working in the time domain clearly. The use of Fourier transforms to simplify the calculation of spectra was first documented by Lasser [48] where he is able to break the spectral contributions into terms which lend themselves to physical interpretation.

There are some technical points which need to be mentioned regarding the numerical nature of the discrete fast Fourier transform. Given that a continuous function is being sampled a finite number of times on a fixed and enforced periodicity interval, there are certain constraints as to what can be achieved. As with all numerical techniques, there is the problem arising from the fact that what we have is an approximation to the actual function. To ensure that the various harmonic modes of the true function are not lost in ambiguity, we require sampling of ten points or more over the period of the fastest varying harmonic [48].

In order to work in the time domain it is important to note that, when working with Fourier transforms, the following relationship holds

$$F(e^{i(\omega_j-\omega-i\gamma_j)t}) \propto \frac{1}{i(\omega_j-\omega)-\gamma_j}, \tag{2.39}$$

where $F(f(t))$ denotes the Fourier transform of $f(t)$. It is possible to write $\chi^{(3)}_{CARS}$ in terms of a sum of terms like those on the RHS of (2.39) and thus to calculate the frequency dependent $\chi^{(3)}_{CARS}$ by taking the Fourier transform of an, as yet undefined, function which reduces greatly the computational demand of the procedure.

To work in the time domain we write the radiation as a sum of autocorrelation functions :

$$\phi(t) = \sum_{j=1}^{N} A_j e^{(i\omega_j - \gamma_j)t}. \tag{2.40}$$

The Fourier transform of this must be $\chi^{(3)}_{CARS}$, which allows us to write the autocorrelation function for the Anti-Stokes Raman spectrum as

$$\Phi(t) = \alpha e^{\underline{\mathbf{G}}t} \underline{\rho} \alpha, \tag{2.41}$$

where α is defined in equation (2.38) and is a row vector. $\underline{\mathbf{G}}$ is defined in equation (2.37) and ρ is diagonal in the transition population differences. This is convenient because if we calculate the eigenvector matrix Q of G then we have that

$$\underline{Q}^{-1}\underline{G}\underline{Q} = diag(i\omega_j - \gamma_j). \tag{2.42}$$

Thus (2.41) can be written in the following way

$$\Phi(t) = \alpha \underline{Q}\underline{Q}^{-1} e^{\underline{\mathbf{G}}t} \underline{Q}\underline{Q}^{-1} \underline{\rho} \alpha = \alpha \underline{Q} e^{(i\omega_j - \gamma_j)t} \underline{Q}^{-1} \underline{\rho} \alpha. \tag{2.43}$$

This allows us to calculate the sum of autocorrelation functions for all the transitions which, when Fourier transformed, gives us $\chi^{(3)}_{CARS}$. We require both $\chi^{(3)}_{CARS}$ and $|\chi^{(3)}_{CARS}|^2$ in certain cases where the non-resonant background term cannot be neglected. In this case the expression for $|\chi^{(3)}_{CARS}|^2$ becomes, when working in the time domain,

$$|\chi^{(3)}_{CARS}|^2 = \sum_j \sum_k \left\{ \frac{a_j}{i(\omega - \omega_j) - \Gamma_j} \right\} \left\{ \frac{a_k^*}{i(\omega - \omega_k) - \Gamma_k} \right\}. \tag{2.44}$$

By decomposing in partial fractions and after some algebra this expression becomes

$$\begin{aligned} |\chi^{(3)}_{CARS}|^2 \;=\; & \sum_j \left\{ \frac{a_j}{i(\omega - \omega_j) - \Gamma_j} \right\} \sum_k \left\{ \frac{a_k^*}{i(\omega_k - \omega_j) - \Gamma_k - \Gamma_j} \right\} + \\ & \sum_k \left\{ \frac{a_k^*}{-i(\omega - \omega_k) - \Gamma_k} \right\} \\ & \sum_j \left\{ \frac{a_j}{i(\omega_k - \omega_j) - \Gamma_k - \Gamma_j} \right\}, \end{aligned} \tag{2.45}$$

where, by making the following substitutions,

$$b_j = \sum_k \left\{ \frac{a_k^*}{i(\omega_k - \omega_j) - \Gamma_j - \Gamma_k} \right\} \tag{2.46}$$

and

$$b_j^* = \sum_k \left\{ \frac{a_k}{-i(\omega_k - \omega_j) - \Gamma_j - \Gamma_k} \right\}, \tag{2.47}$$

we obtain

$$|\chi^{(3)}_{CARS}|^2 = \sum_j \frac{a_j b_j}{i(\omega - \omega_j) - \Gamma_j} + \sum_k \frac{a_k^* b_k^*}{-i(\omega - \omega_k) - \Gamma_k}. \tag{2.48}$$

Thus we are able to calculate the intensity spectum using the third order non-linear susceptibility and its square modulus in the time domain.

The convolution of two functions in the frequency domain is equivalent to taking the Fourier transform of the product of the two functions in the time domain. The measured spectrum is, in fact, the convolution of the above functions with the instrument function of the detector. Thus it is necessary to write the instrument function as the Fourier transform of some function of time. This greatly simplifies the calculation of the actual spectrum.

2.8.3 Time Domain vs. Frequency Domain

In the time domain, in order to calculate the spectrum only the Fourier transform needs to be taken. For comparison with experimental spectra this only needs to be sampled on the same number of points as channels on the diode array or CCD camera used as a detector. The G-matrix in this case needs to be diagonalised only once. This allows us a severe improvement in the computational efficiency. The use of Fourier transform techniques is compared to other techniques and the advantages are discussed in the context of temperature and relative concentration diagnostics for $N_2 - O_2$ mixtures in [59].

When working in the frequency domain the spectrum needs to be calculated on a fine frequency grid. Grid points must have a spacing much less than any features of the spectrum because of the small widths of the transitions. This leads to a much more computationally intensive exercise. If a sufficiently coarse frequency grid were chosen, no line structure would appear at all.

Aside from this, the measured spectrum is, in fact, the convolution of the actual emitted spectrum with the instrument function. The instrument function is a Voigt profile. The calculation of the Voigt profile is again computationally intensive, involving long numerical integrations. The Fourier transform of a Voigt profile is

$$F(t) = e^{-a|t| - \frac{1}{2}bt^2}, \tag{2.49}$$

and thus the Fourier transform of the convolution of the spectrum with the instrument function is simply the product of their respective Fourier transforms. This allows one to replace the calculation of a large number of numerical integrations with a single calculation of (2.49) at each of the points on the time grid.

The final result is that at each point (a large number of points) in the frequency domain, the G-matrix needs to be inverted as well as a numerical integration performed to calculate the Voigt profile and then finally the convolution of the two needs to be calculated. In the time domain, at a number of points orders of magnitudes less than in the case of the frequency domain, the sum of autocorrelation functions needs to be calculated and then the product taken of this with the Fourier transform of the Voigt profile. An inverse Fourier transform of the result will give the frequency spectrum. In conclusion, there is vastly less computation required when working in the time domain.

2.9 Calculation of Line-Widths

In the calculation of spectra, the values of the line-widths have been used but no argument in favour of any particular set of parameters has been given. It is simple to discuss, in principle, the calculation of spectra and even simple to do such calculations given the line-widths, but the calculation of the line-widths presents a small but subtle problem.

The four unknown parameters $(A, N, \beta/\gamma, l_c)$ need to be found and this presents somewhat of a challenge. To obtain four values is not too difficult given the wealth of isotropic data available to be fitted (see Appendix A). It is finding a set of uncorrelated parameters that returns a small $\frac{\chi^2}{ndf}$ that is more of a challenge. A number of fits to the data have been attempted but never have the correlations between the parameters been published. A solid argument in favour of highly correlated parameters is impossible as highly correlated parameters are manifestations of each other and the problem is overdetermined.

In choosing parameters for the prediction of the line-widths, the correlations are taken into consideration as much as is possible.

The possibility of reducing the number of parameters is something that must be considered very carefully as this greatly simplifies the problem. As there is a limited amount of data in the anisotropic region, our primary region of interest, the smaller the number of parameters requiring fitting the better. The anisotropic data is shown in Appendix B.

Fits to all four parameters are considered initially but, in an attempt to

simplify the problem, a value for l_c is fixed and the remaining parameters fitted. l_c will be fixed to the value obtained in a fit to the isotropic data. This will allow the fitting of only three parameters to the anisotropic data.

The reason for fixing l_c is that it represents an effective interaction length for the collisions and thus is the most physical of the parameters occurring in the basis rates. There is, in principle, no reason why the isotropic and anisotropic data should lead to different values of l_c.

The thing that must be remembered, however, is that we are dealing with an effective l_c because the various poles of the interaction potential will have different values of l_c. Ideally a theoretical calculation of l_c would be possible as it is the parameter most likely to lend itself to a theoretical calculation. This possibility is being considered and will be the subject of further work.

Two fitting methods will be considered with their results shown in the following chapter. They will be discussed here.

2.9.1 Levenberg-Marquardt Least Squares Fitting

When a non-linear least squares fit was required, a Levenberg-Marquardt least squares fitting algorithm has been implemented. This procedure involves finding the sum of the squares of the residuals as a function of certain parameters, to be fitted, and then minimising this function, weighted by the errors, by an optimal choice of parameters. This function to be minimised will be written in two forms with both results being calculated and tabulated. This is done for ease of comparison with values in the literature. The first formula contains the squares of the uncertainties weighted by the sum of the squares of the uncertainties and is given by:

$$E = \sum_i \frac{\left(\Gamma_i - W^K_{j_i,j_{i+K},j_i,j_{i+K}}(A, N, \beta(\gamma), l_c)\right)^2}{\frac{\sigma_i^2}{\sum_j \sigma_j^2}}. \tag{2.50}$$

The second formula to be used is the standard χ^2 formula:

$$\chi^2 = \sum_i \frac{\left(\Gamma_i - W^K_{j_i,j_{i+K},j_i,j_{i+K}}(A, N, \beta(\gamma), l_c)\right)^2}{\sigma_i^2}. \tag{2.51}$$

In these formulae Γ_i is an experimental width, σ_i is the uncertainty in Γ_i and $W^K_{j_i,j_{i+K},j_i,j_{i+K}}(A, N, \beta(\gamma), l_c)$ is the theoretical prediction for a given set of parameters. It is the quantity given by equation (2.50) that is referred to in this thesis as the error. These functions are minimised by calculating the slope of the function in parameter space and then stepping towards a

minimum. There are two basic implementations of a Levenberg-Marquardt algorithm. Firstly, if one is able to analytically determine the partial derivative of equation (2.50) with respect to each of the parameters, then it is possible to easily find the slope. If the function, for whatever reason, cannot be differentiated, it is possible to use numerical differentiation to find an approximation to the slope and then use this to find a minimum. It is obvious that both forms will be minimised by the same set of parameters, though the sum will be different.

This fitting procedure is based on certain assumptions; these being that the parameters are orthogonal and the errors are normally distributed and uncorrelated. The procedure has shown a surprisingly robust ability to handle cases where these assumptions are not strictly true.

The only drawback to this, and to all non-linear least squares fitting algorithms, is that, in general, it is not possible to guarantee that a global, rather than local, minimum has been found. This makes the initial guess of parameter values important. Contour plotting procedures are not feasible given the computation time required to generate sufficient points to plot contours.

2.9.2 Partially Linearised Fitting

If one considers the line-width equation being used, it is simple enough to note that it can be written as

$$\begin{aligned} W^K_{j_i,j_f,j'_i,j'_f} &= A\left(\frac{T_0}{T}\right)^N \frac{\delta_{j_i j'_i}\delta_{j_f j'_f}}{2}\left(\frac{1}{\tau'_{j_i}}+\frac{1}{\tau'_{j_f}}\right) - \frac{[j'_i]}{2}\sqrt{[j_f][j'_f]} \\ &\quad \left(\Omega^2_{j_{imax}} e^{-\frac{\hbar\omega_{j_{imax}j_i}}{k_B T}} + \Omega^2_{j_{fmax}} e^{-\frac{\hbar\omega_{j_{fmax}j_f}}{k_B T}}\right) \\ &\quad \sum_\lambda [\lambda] \begin{pmatrix} j_i & j'_i & \lambda \\ 0 & 0 & 0 \end{pmatrix} \begin{pmatrix} j_f & j'_f & \lambda \\ 0 & 0 & 0 \end{pmatrix} \\ &\quad \begin{Bmatrix} j_i & j_f & K \\ j'_i & j'_f & \lambda \end{Bmatrix} \frac{Q'_\lambda}{\Omega_\lambda}. \end{aligned} \tag{2.52}$$

By taking the logarithm of widths, the equation can be made linear in two parameters i.e. $\ln(A)$ and N:

$$\begin{aligned} \ln\left(W^K_{j_i,j_f,j'_i,j'_f}\right) &= \ln(A) + N ln\left(\frac{T_0}{T}\right) + \ln\left(\frac{\delta_{j_i j'_i}\delta_{j_f j'_f}}{2}\left(\frac{1}{\tau'_{j_i}}+\frac{1}{\tau'_{j_f}}\right)\right. \\ &\quad \left. -\frac{[j'_i]}{2}\sqrt{[j_f][j'_f]}\left(\Omega^2_{j_{imax}} e^{-\frac{\hbar\omega_{j_{imax}j_i}}{k_B T}} + \Omega^2_{j_{fmax}} e^{-\frac{\hbar\omega_{j_{fmax}j_f}}{k_B T}}\right)\right) \end{aligned}$$

$$\sum_{\lambda}[\lambda]\begin{pmatrix} j_i & j_i' & \lambda \\ 0 & 0 & 0 \end{pmatrix}\begin{pmatrix} j_f & j_f' & \lambda \\ 0 & 0 & 0 \end{pmatrix} \begin{Bmatrix} j_i & j_f & K \\ j_i' & j_f' & \lambda \end{Bmatrix} \frac{Q_\lambda'}{\Omega_\lambda}\Big). \tag{2.53}$$

The equation for the logarithm of the width is then only non-linear in l_c and either β or γ. Then, given a particular set of values for the remaining two non-linear parameters, there is no question of the best fit values for the linear parameters. The solution can be found by finding the single value decomposition of the design matrix and then inverting the problem. By taking the single value decomposition, we are able to ascertain immediately if the system of algebraic equations is close to singular or not. As it turns out this was never a problem.

The new error, σ', is given by

$$\sigma' = \frac{\sigma}{\Gamma}. \tag{2.54}$$

This does affect the weightings and results in errors which cannot be directly compared with those obtained in the case of the Levenberg-Marquardt fits, but the χ^2 values are still comparable.

2.9.3 Non-resonant Background

The non-resonant background is the signal contribution which can be thought of as coming from transitions between virtual states only. Thus no actual characteristic transition of the medium is being probed.

The non-resonant background can be suppressed through the design of the experiment. In the case of the Swedish spectra this has not been done. Thus a brief discussion of some of the literature available on non-resonant contributions to the third order non-linear susceptibility is necessary.

The first calculation of χ_{NR} was done by Rado [72] and this work has formed the basis for further calculations.

In [70] CARS is used to find a value for χ_{NR} for H_2 taking into account the most recent results regarding Raman cross-sections. A value of χ_{NR} for N_2 is then calculated using an experimentally determined value of $\frac{\chi_{NR}^{H_2}}{\chi_{NR}^{N_2}}$. A large number of χ_{NR} values for other molecules are also presented in this paper.

The value of χ_{NR} used here is taken from [71]. This is the same value that was used in [44, 45, 69]. In this text much of the background is presented with a large amount of detail.

Chapter 3

Implementation

To achieve the required end of spectral calculation and comparison, it is imperative that an accurate model of line-widths be available. A model, given earlier, has been developed but, due to the difficulty in calculating the potential surfaces, it has in part a dependence on basis rates which in turn contain parameters which need to be determined empirically. Two different methods for determination of these parameters have been discussed and the results will be shown and discussed here.

The first involved the implementation of a Levenberg-Marquardt fitting procedure and the second involved the partial linearisation of the problem, reducing the number of non-linear parameters.

These results need to be considered and an evaluation of the results made to allow the selection of the best model and its parameters. First, all the results will be documented and then a comparison made.

3.1 Levenberg-Marquardt Fits to all Parameters

The first fit involves using a Levenberg-Marquardt fit to find all 4 unknown parameters. This is done for the isotropic data, anisotropic data and then the combined data. In each case, both forms of the basis rates are used as well as both possible values of n which occur in the adiabaticity correction.

3.1.1 Isotropic (Vibrational) Data

The isotropic data is a much better endowed data set than the anisotropic data. It consists of 179 distinct widths and is shown in appendix A. At each temperature we have sufficient widths to expect reasonable fit results. We

also have data at a temperature range larger than we expect to cover in temperature diagnostics in a piston chamber.

Free A, N, β, l_c

The attempt to fit all of the parameters with an exponential form of the basis rates and $n = 1$ resulted in an error of $4.167\frac{mk^2}{amagat^2}$ for the fitted parameters shown in table 3.1. These results are consistent with those in [41] bearing in mind that the units are different. Note the high correlations between the parameters. The results for a similar fit with $n = 2$ result in an error

$n = 1$					
Fit Results		Correlations			
Parameter	Value	$A(\frac{mk}{amagat})$	N	β	l_c(Å)
$A(\frac{mk}{amagat})$	3.602	1.000	0.8471	0.9985	-0.9152
N	0.8183	-	1.000	0.8292	-0.7128
β	1.845	-	-	1.000	-0.9308
l_c(Å)	0.7652	-	-	-	1.000
$n = 2$					
Fit Results		Correlations			
Parameter	Value	$A(\frac{mk}{amagat})$	N	β	l_c(Å)
$A(\frac{mk}{amagat})$	3.885	1.000	0.8574	0.9988	-0.8902
N	0.8212	-	1.000	0.8421	-0.7067
β	2.037	-	-	1.000	-0.9054
l_c(Å)	0.6814	-	-	-	1.000

Table 3.1: Parameters for a complete Levenberg-Marquardt fit to isotropic data with an exponential form of the basis rates

of $4.122\frac{mk^2}{amagat^2}$ and the parameters are shown in table 3.1. The parameter correlations are similar to those of the fit for $n = 1$ in table 3.1. The change in the value of n does not result in significant changes in the parameters, correlations or error, although this is marginally lower.

Free A, N, γ, l_c

Now in the case of the polynomial form of the basis rates, a complete fit to the isotropic data with $n = 1$ results in an error of $5.217\frac{mk^2}{amagat^2}$ with the results shown in table 3.2. This fit converged very slowly implying a very flat parameter space and this is confirmed by the very high correlations between

the parameters. The error is larger than in either of the cases for an exponential form of the basis rates. The results for a similar fit with $n = 2$ give

$n = 1$					
Fit Results		Correlations			
Parameter	Value	$A(\frac{mk}{amagat})$	N	γ	l_c(Å)
$A(\frac{mk}{amagat})$	80.19	1.000	-0.9740	0.9997	-0.9761
N	-8.593×10^{-2}	-	1.000	-0.9776	0.9721
γ	1.240	-	-	1.000	-0.9802
l_c(Å)	0.8045	-	-	-	1.000
$n = 2$					
Fit Results		Correlations			
Parameter	Value	$A(\frac{mk}{amagat})$	N	γ	l_c(Å)
$A(\frac{mk}{amagat})$	70.91	1.000	-0.9722	0.9997	-0.9802
N	-7.456×10^{-2}	-	1.000	-0.9700	0.9717
γ	1.197	-	-	1.000	-0.9839
l_c(Å)	0.7899	-	-	-	1.000

Table 3.2: Parameters for a complete Levenberg-Marquardt fit to isotropic data with a polynomial form of the basis rates

an error of $4.822\frac{mk^2}{amagat^2}$ and the parameters are shown in table 3.2. Once again the change in n results in no significant changes in parameters or correlations and again the error is marginally reduced. Both of the polynomial fits converge extremely slowly. They are less sensitive to small changes in the parameters. The correlations between parameters, in the case of a polynomial form of the basis rates, are very high. The form of the basis rates cannot, based on the correlations, be considered a satisfactory representation of the true basis rates.

3.1.2 Anisotropic (Rotational) Data

The anisotropic data is shown in appendix B and is a significantly smaller set than the isotropic data set. Again a large temperature range is covered but with a reduced number of widths at most temperatures ($J = 8 - 16$). This will prove to be quite a debilitating situation.

Free A, N, β, l_c

For completeness all 4 parameters have been fitted to the anisotropic data. In the case where $n = 1$, the error is $4.293\frac{mk^2}{amagat^2}$ and the results are shown in table 3.3. This error is for the anisotropic data set and so should not be compared with the errors from the isotropic data set. Errors that can be compared have been calculated and are shown in table 3.17. The correlations, however, can be compared and we find, in general, reduced correlations for this fit over the corresponding isotropic fit shown in table 3.1. In the $n = 2$

$n = 1$					
Fit Results		Correlations			
Parameter	Value	$A(\frac{mk}{amagat})$	N	β	l_c(Å)
$A(\frac{mk}{amagat})$	4.309	1.000	0.5660	0.9993	-0.8408
N	0.7866	-	1.000	0.5570	-0.3617
β	2.581	-	-	1.000	-0.8607
l_c(Å)	0.6113	-	-	-	1.000
$n = 2$					
Fit Results		Correlations			
Parameter	Value	$A(\frac{mk}{amagat})$	N	β	l_c (Å)
$A(\frac{mk}{amagat})$	4.507	1.000	0.6023	0.9994	-0.8151
N	0.7878	-	1.000	0.5950	-0.3795
β	2.732	-	-	1.000	-0.8341
l_c (Å)	0.5752	-	-	-	1.000

Table 3.3: Parameters for a complete Levenberg-Marquardt fit to anisotropic data with an exponential form of the basis rates

case, we have that the error is $4.207\frac{mk^2}{amagat^2}$ with the resulting fit shown in table 3.3. The error is, again, marginally reduced and the parameters and correlations are largely unchanged. Once again, based on the correlations, the form of the basis rates cannot be regarded as satisfactory.

Free A, N, γ, l_c

Then it is possible to attempt the fit using the polynomial form of the model. Again we consider the two cases. For $n = 1$, we obtain an error of $4.104\frac{mk^2}{amagat^2}$ with the fit results shown in table 3.4. It is interesting to note that here the correlations have not been reduced over the corresponding isotropic fit (table 3.2) as was the case with the exponential form of the basis rates. In the

$n = 2$ case, we have an error of $3.957\frac{mk^2}{amagat^2}$ and the fit is shown in table 3.4. Once again the change of n results in a small reduction in the error but no really significant changes.

3.1.3 Mixed Data Set

The model being used should be able to predict both the isotropic and anisotropic line-widths with one set of parameters. Thus it is possible to combine the two sets of experimental data and do one fit. Given the larger amount of isotropic data, these fits will be dominated by the isotropic data.

Free A, N, β, l_c

In the case where $n = 1$, the fit (table 3.5) results in an error of $5.745\frac{mk^2}{amagat^2}$. Of interest is that the addition of a small amount of anisotropic data results in a significant change in the correlations, which might be expected to be very similar to those arising from the corresponding fit to the isotropic data in table 3.1.

In the $n = 2$ case, we have an error of $5.847\frac{mk^2}{amagat^2}$ for the fit shown in table 3.5. The same trend in correlations over the corresponding isotropic fit is observed. It is noteworthy that, contrary to previous fit trends, the error is marginally increased for $n = 2$.

Free A, N, γ, l_c

For the $n = 1$ mixed data set fit, we have an error of $8.862\frac{mk^2}{amagat^2}$ with the fit results shown in table 3.6. Again the addition of the anisotropic data reduces the correlations from the corresponding fit to the isotropic data shown in table 3.2.

In the $n = 2$ case, we have an error of $8.956\frac{mk^2}{amagat^2}$ for the fit shown in table 3.6. The change to $n = 2$ results in a marginal increase in the error.

3.2 Levenberg-Marquardt Fits to 3 Parameters

These fits will utilise the value of l_c obtained in the previous section and fit the remaining parameters to the anisotropic data. The value of l_c used will be that from the corresponding fit to the isotropic data.

$n = 1$					
Fit Results		Correlations			
Parameter	Value	$A(\frac{mk}{amagat})$	N	γ	l_c(Å)
$A(\frac{mk}{amagat})$	64.26	1.000	-0.9925	0.9999	-0.9978
N	-9.038×10^{-2}	-	1.000	-0.9929	0.9929
γ	1.209	-	-	1.000	-0.9983
l_c(Å)	0.7808	-	-	-	1.000
$n = 2$					
Fit Results		Correlations			
Parameter	Value	$A(\frac{mk}{amagat})$	N	γ	l_c(Å)
$A(\frac{mk}{amagat})$	58.54	1.000	-0.9900	1.000	-0.9977
N	-8.172×10^{-2}	-	1.000	-0.9904	0.9906
γ	1.176	-	-	1.000	-0.9983
l_c(Å)	0.7680	-	-	-	1.000

Table 3.4: Parameters for a complete Levenberg-Marquardt fit to anisotropic data with a polynomial form of the basis rates

$n = 1$					
Fit Results		Correlations			
Parameter	Value	$A(\frac{mk}{amagat})$	N	β	l_c(Å)
$A(\frac{mk}{amagat})$	3.347	1.000	0.6479	0.9972	-0.8381
N	0.7842	-	1.000	0.6180	-0.3487
β	1.783	-	-	1.000	-0.8750
l_c(Å)	0.7620	-	-	-	1.000
$n = 2$					
Fit Results		Correlations			
Parameter	Value	$A(\frac{mk}{amagat})$	N	β	l_c(Å)
$A(\frac{mk}{amagat})$	3.504	1.000	0.6711	0.9978	-0.8029
N	0.7830	-	1.000	0.6471	-0.3511
β	1.909	-	-	1.000	-0.8391
l_c(Å)	0.6861	-	-	-	1.000

Table 3.5: Parameters for a complete Levenberg-Marquardt fit to mixed data with an exponential form of the basis rates

Free A, N, β

For $n = 1$, we fix $l_c = 0.7652$Å and obtain an error of $4.597\frac{mk^2}{amagat^2}$ for the fit shown in table 3.7. The removal of the freedom to vary l_c results in a slightly larger error than in the corresponding fit to all 4 parameters shown in table 3.3. The correlation between A and β remains very high, while the correlation between A and N is reduced. For the $n = 2$, case the error was $4.462\frac{mk^2}{amagat^2}$ for an $l_c = 0.6814$Å and the results are shown in table 3.7. Again $n = 2$ results in a smaller error when considering an individual data set.

Free A, N, γ

For $n = 1$, we fix $l_c = 0.8045$Å and obtain an error of $4.105\frac{mk^2}{amagat^2}$ for the fit shown in table 3.8. There is a significant reduction in the correlations over the corresponding 4 parameter fit shown in table 3.4.

For the $n = 2$ case, the error was $3.959\frac{mk^2}{amagat^2}$ for an $l_c = 0.7899$Å and the results are shown in table 3.8.

3.3 Partially Linearised Model Fits to 3 Parameters

3.3.1 Anisotropic Data

Free A, N, β

For the $n = 1$ case and with $l_c = 0.7652$Å again, an error of 2.372×10^{-3} results. The parameter fit is shown in table 3.9.

For $n = 2$, the results are in table 3.9 and the error is 2.151×10^{-3} and $l_c = 0.6814$Å.

Free A, N, γ

For the $n = 1$ case and with $l_c = 0.8045$Å, I obtain an error of 1.610×10^{-3}. The parameter fit is shown in table 3.10. For $n = 2$, the results are in table 3.10 and the error is 1.797×10^{-3} with $l_c = 0.7899$Å. In this case the error has increased marginally. This is misleading and the errors shown in table 3.16 should be used for comparison.

$n = 1$					
Fit Results		Correlations			
Parameter	Value	$A(\frac{mk}{amagat})$	N	γ	l_c(Å)
$A(\frac{mk}{amagat})$	38.68	1.000	-0.8092	0.9908	-0.8646
N	-4.951×10^{-2}	-	1.000	-0.8600	0.9103
γ	0.9997	-	-	1.000	-0.9241
l_c(Å)	1.185	-	-	-	1.000
$n = 2$					
Fit Results		Correlations			
Parameter	Value	$A(\frac{mk}{amagat})$	N	γ	l_c(Å)
$A(\frac{mk}{amagat})$	40.78	1.000	-0.7290	0.9865	-0.8241
N	-6.302×10^{-2}	-	1.000	-0.7985	0.8676
γ	1.022	-	-	1.000	-0.9048
l_c(Å)	1.070	-	-	-	1.000

Table 3.6: Parameters for a complete Levenberg-Marquardt fit to mixed data with a polynomial form of the basis rates

$n = 1$				
Fit Results		Correlations		
Parameter	Value	$A(\frac{mk}{amagat})$	N	β
$A(\frac{mk}{amagat})$	2.848	1.000	0.3982	0.9997
N	0.7806	-	1.000	0.3956
β	1.519	-	-	1.000
$n = 2$				
Fit Results		Correlations		
Parameter	Value	$A(\frac{mk}{amagat})$	N	β
$A(\frac{mk}{amagat})$	3.064	1.000	0.4109	0.9998
N	0.7812	-	1.000	0.4086
β	1.684	-	-	1.000

Table 3.7: Parameters for a reduced Levenberg-Marquardt fit to anisotropic data with an exponential form of the basis rates

Fit Results		Correlations		
Parameter	Value	$A(\frac{mk}{amagat})$	N	γ
$A(\frac{mk}{amagat})$	60.44	1.000	-0.2177	0.9998
N	-8.435×10^{-2}	-	1.000	-0.2200
γ	1.185	-	-	1.000
$n = 2$				
Fit Results		Correlations		
Parameter	Value	$A(\frac{mk}{amagat})$	N	γ
$A(\frac{mk}{amagat})$	55.49	1.000	-0.1664	0.9997
N	-7.622×10^{-2}	-	1.000	-0.1692
γ	1.155	-	-	1.000

Table 3.8: Parameters for a reduced Levenberg-Marquardt fit to anisotropic data with a polynomial form of the basis rates

Fit Results		
Parameter	Value	
	$n = 1$	$n = 2$
$ln(A)$	1.521	1.762
N	0.7683	0.7756
β	2.735	3.632

Table 3.9: Parameters for a partially linearised fit to anisotropic data with an exponential form of the basis rates

Fit Results		
Parameter	Value	
	$n = 1$	$n = 2$
$ln(A)$	4.473	4.328
N	-0.1450	-0.1315
γ	1.333	1.277

Table 3.10: Parameters for a partially linearised fit to anisotropic data with a polynomial form of the basis rates

3.3.2 Room Temperature Anisotropic Data

Free A, N, β

Here I do a fit to the 293K and 296K anisotropic data in order to eliminate much of the temperature dependence and thus decide which model best reproduces the J dependence of the data. For the $n = 1$ case and with $l_c = 0.7652$Å, an error of 2.366×10^{-3} results. The parameter fit is shown in table 3.11. For $n = 2$, the results are in table 3.11 and the error is 2.145×10^{-3}

Fit Results		
Parameter	Value	
	$n = 1$	$n = 2$
$ln(A)$	1.589	1.831
N	-	-
β	2.739	3.640

Table 3.11: Parameters for a partially linearised fit to room temperature data with an exponential form of the basis rates

and $l_c = 0.6814$Å.

Free A, N, γ

For the $n = 1$ case and with $l_c = 0.8045$Å, I obtain an error of 1.605×10^{-3}. The parameter fit is shown in table 3.12. For $n = 2$, the results are in table

Fit Results		
Parameter	Value	
	$n = 1$	$n = 2$
$ln(A)$	4.535	4.387
N	-	-
γ	1.334	1.278

Table 3.12: Parameters for a partially linearised fit to room temperature data with a polynomial form of the basis rates

3.12 and the error is 1.793×10^{-3} with $l_c = 0.7899$Å.

The N values provide the temperature scaling which is negligible in this case, i.e. less than 0.1%. To compare these values, the error is calculated

using (2.50). These errors are shown in table 3.13 along with the errors given earlier.

n	Basis Rates	Error	Error $\frac{mk^2}{amagat^2}$
1	Exponential	2.366×10^{-3}	4.788
2	Exponential	2.145×10^{-3}	4.628
1	Polynomial	1.605×10^{-3}	4.203
2	Polynomial	1.793×10^{-3}	4.047

Table 3.13: Errors for room temperature fits

3.3.3 Sensitivity of Parameters to l_c

In order to reduce the number of parameters, we have fixed the value of l_c without thus far fully evaluating the consequences of this. It is necessary to consider the effect of variations of l_c on the parameters and errors. This is done for the anisotropic data only, as the value of l_c is fixed by the isotropic data. Here only the error is included because it is related to the value of χ^2 by a constant multiplicative factor and so the analysis in terms of percentages is the same.

The complete sets of results are shown in appendices C and D. A more concise listing is given in table 3.14.

Based on the results shown table 3.14 it is clear that the actual parameters can differ quite largely for different values of l_c. The errors remain fairly consistent in regions of 25% around the best fit value of l_c. So, in choosing a value of l_c, all that must be ensured is that the chosen value is within $\approx 25\%$ of the true value to ensure that the error is within $\approx 10\%$.

The true value of l_c is not known but the results from the Levenberg-Marquardt fits to all 4 parameters have a mean value of 0.7220 and $\sigma_{n-1} = 0.08807$. This is a 12% deviation. So it is with renewed confidence that the results for the fits fixing l_c can be considered.

3.3.4 Discussion of Fit Results

The complete results are shown in tables 3.15 and 3.16. There is a fair amount of information shown in table 3.15 that needs to be considered. Fits for the same model but with differing values of n are in adjacent rows. In all but the cases for the combined data sets, the choice of $n = 2$ gives a marginally

Exponential form of basis rates				
l_c(Å)	$A(\frac{mK}{amagat})$	N	β	Error $\frac{mk^2}{amagat^2}$
0.5	7.930	0.8072	5.160	4.365
0.6	4.000	0.7852	2.365	4.221
0.65	3.343	0.7822	1.887	4.334
0.7	2.928	0.7807	1.586	4.557
0.75	2.638	0.7797	1.377	4.884
0.8	2.420	0.7789	1.223	5.303
0.85	2.251	0.7781	1.105	5.802
0.9	2.115	0.7772	1.013	6.365
1.0	1.909	0.7753	0.8796	7.636
Polynomial form of basis rates				
l_c(Å)	$A\frac{mK}{amagat}$	N	β	Error $\frac{mk^2}{amagat^2}$
0.5	631.3	-0.1929	2.246	4.388
0.6	119.5	-0.1394	1.463	4.078
0.65	88.87	-0.1190	1.340	4.011
0.7	72.01	-0.1014	1.256	3.974
0.75	61.42	-8.653×10^{-2}	1.194	3.958
0.8	54.24	-7.383×10^{-2}	1.146	3.961
0.85	49.14	-6.313×10^{-2}	1.109	3.979
0.9	45.38	-5.419×10^{-2}	1.079	4.012
1.0	40.38	-4.082×10^{-2}	1.034	4.128

Table 3.14: Results of fits for various values of l_c

lower error than $n = 1$. The $n = 1$ case was included for completeness. It only applies to the far wings of infra-red spectra [66].

The Levenberg-Marquardt fits to all the parameters are the first 12 fits in table 3.15. In the case of the isotropic data, the lowest error is obtained with exponential basis rates. For the anisotropic data the best results occur for polynomial basis rates. The mixed data set is best fitted with $n = 1$ and exponential basis rates. These results do not tell unequivocably which model is the best or most correct.

#	Set	Fit	n	$A(\frac{mK}{amagat})$	N	β	γ	l_c(Å)
1	Q	L-M(4)	1	3.603	0.8184	1.845	-	0.7652
P1	Q	L-M(4)	2	3.885	0.8212	2.037	-	0.6814
2	Q	L-M(4)	1	80.19	-8.593×10^{-2}	-	1.240	0.8045
P2	Q	L-M(4)	2	70.91	-7.456×10^{-2}	-	1.197	0.7899
3	S	L-M(4)	1	4.309	0.7866	2.581	-	0.6113
P3	S	L-M(4)	2	4.507	0.7878	2.732	-	0.5752
4	S	L-M(4)	1	64.26	-9.039×10^{-2}	-	1.209	0.7808
P4	S	L-M(4)	2	58.54	-8.172×10^{-2}	-	1.176	0.7679
P5	Q+S	L-M(4)	1	3.347	0.7842	1.783	-	0.7620
5	Q+S	L-M(4)	2	3.504	0.7830	1.909	-	0.6861
P6	Q+S	L-M(4)	1	38.68	-4.951×10^{-2}	-	0.9997	1.185
6	Q+S	L-M(4)	2	40.78	-6.302×10^{-2}	-	1.022	1.070
7	S	L-M(3)	1	2.848	0.7806	1.519	-	0.7652
P7	S	L-M(3)	2	3.064	0.7812	1.684	-	0.6814
8	S	L-M(3)	1	60.44	-8.435×10^{-2}	-	1.185	0.8045
P8	S	L-M(3)	2	55.49	-7.622×10^{-2}	-	1.155	0.7899
9	S	Lin(T_0)	1	4.901	-	2.739	-	0.7652
10	S	Lin(T_0)	2	6.244	-	3.640	-	0.6814
11	S	Lin(T_0)	1	93.22	-	-	1.334	0.8045
12	S	Lin(T_0)	2	80.43	-	-	1.278	0.7899
13	S	Lin S	1	4.576	0.7683	2.735	-	0.7652
P9	S	Lin S	2	5.826	0.7756	3.632	-	0.6814
14	S	Lin S	1	87.64	-0.1450	-	1.333	0.8045
P10	S	Lin S	2	75.83	-0.1315	-	1.277	0.7899

Table 3.15: Combined parameter listing

The errors do not give a good representation of how well the trends in the data are fitted. The better results for each particular model are plotted along with the experimental data to give an indication of how well the trends in the experimental data are actually followed by the model. For the isotropic

#	Set	Fit	Error	χ^2	$\frac{\chi^2}{ndf}$
1	Q	L-M(4)	4.167	266.6	1.523
P1	Q	L-M(4)	4.122	263.7	1.507
2	Q	L-M(4)	5.217	333.7	1.907
P2	Q	L-M(4)	4.822	308.5	1.763
3	S	L-M(4)	4.293	307.4	8.783
P3	S	L-M(4)	4.207	301.3	8.607
4	S	L-M(4)	4.104	293.9	8.397
P4	S	L-M(4)	3.957	283.4	8.096
P5	Q+S	L-M(4)	5.745	778.9	3.640
5	Q+S	L-M(4)	5.847	792.7	3.704
P6	Q+S	L-M(4)	8.862	1201	5.615
6	Q+S	L-M(4)	8.956	1214	5.674
7	S	L-M(3)	4.597	329.2	9.405
P7	S	L-M(3)	4.462	319.5	9.130
8	S	L-M(3)	4.105	294.0	8.399
P8	S	L-M(3)	3.959	283.5	8.100
13	S	Lin S	2.372×10^{-3}	794.9	22.71
P9	S	Lin S	2.151×10^{-3}	784.9	22.43
14	S	Lin S	1.610×10^{-3}	627.6	17.93
P10	S	Lin S	1.797×10^{-3}	594.7	16.99

Table 3.16: Combined error and χ^2 listing

Parameters	Errors $\frac{mK^2}{amagat^2}$ for data set		
	Isotropic	Anisotropic	Mixed
P1	4.122	12.92	8.770
P2	4.822	33.80	20.13
P3	13.67	4.207	8.674
P4	40.60	3.957	21.25
P5	5.748	5.743	5.745
P6	10.72	7.200	8.862

Table 3.17: Error comparisons for various parameter fits

case, the parameter fits labelled P1 and P2 are plotted at 295K, 940K and 1500K in figure 3.1.

In this plot it is obvious that the very low J trends in the experimental data are best represented by P1. The curves for P2 appear to have different concavity to the experimental data. P1 does have the lower error, most likely largely due to this low J deviation by P2.

For the anisotropic case, P3 and P4 are compared, in figure 3.2, to the experimental data at 293K, 795K and 1500K. Here it is not possible to identify accurately whether or not the model follows the low J trends in the data as there is very little low J data available. If the trends exhibited by the isotropic data and 293K anisotropic data at low J are expected to exist in the higher temperature anisotropic data, then it is quite clear that these trends are not followed by the model. From the isotropic case it seems as though the polynomial form of the basis rates has the wrong concavity to follow the low J trend. This potential shortcoming is not exposed due to the lack of low J anisotropic data.

In the case of P5 and P6, which should reproduce both isotropic and anisotropic data, isotropic and anisotropic predictions are plotted in figures 3.3 and 3.4 respectively. In this case, the concavity of the polynomial fit, P6, seems to follow the trends in the data better but there is, once again, inadequate low J data for the anisotropic case. The plots in the anisotropic case do rise as J continues to decrease, unlike the fits shown in figure 3.2.

Given that the objective is one set of parameters which can predict both isotropic and anisotropic line-widths, an analysis of the parameters mentioned above to fit the various data sets should be done. The errors occurring when a particular set of parameters is used to fit a particular data set is given in table 3.17. The only parameter fit which is consistent is P5 which has $n = 1$ and an exponential form of the basis rates and was fitted to a mixed data set. This fit also manages to maintain an increasing low J trend. The fits P1 and P2 achieve this as well, but they have much higher errors.

In attempting to reduce correlations and improve the fit by fixing l_c a number of fits resulting from a Levenberg-Marquardt fitting procedure were produced. Again the lower errors were for $n = 2$. The errors were not, however, lower than those achieved on the anisotropic data when all 4 parameters were allowed to vary. Correlations were reduced which is evidence for the high lack of orthogonality in parameter space. Plots of the two best models in this case are shown in figure 3.7. In this case, the exponential model least accurately reproduces the expected low J trends.

The final fitting is done using the partially linearised model. These parameters and their errors, calculated according to (2.50), are given in table 3.16. Once again the $n = 2$ results give marginally lower errors. The plots

of these fits are shown in figure 3.8. These fits suffer from the same low J underestimation as the previous fits. One curiosity of the partially linearised fit results is how close the two prediction are to each other. It is almost impossible to distinguish the two curves. They are certainly in better agreement with each other than any other polynomial and exponential fit. This would not be easy to deduce from the errors given in table 3.16.

In attempting to get the data to unequivocably choose a model, a partially linearised fit to the room temperature (293K and 296K) anisotropic was done. These fits exclude the temperature dependence and should allow the choice of the best model for reproducing the J dependence of the widths. In this case, the lowest error occurs for $n = 2$ which is consistent with all previous results. The best result is for the polynomial form of the basis rates. The best fits are shown in figure 3.9. From the plot it is clear that the exponential form of the basis rates reproduces the line-widths more accurately for $J < 3$ and for $J > 10$. The error for the polynomial form of the basis rates is lower only because it more accurately reproduced the line-widths for $3 < J < 10$, but these are far from reasonable reproductions of the experimental data.

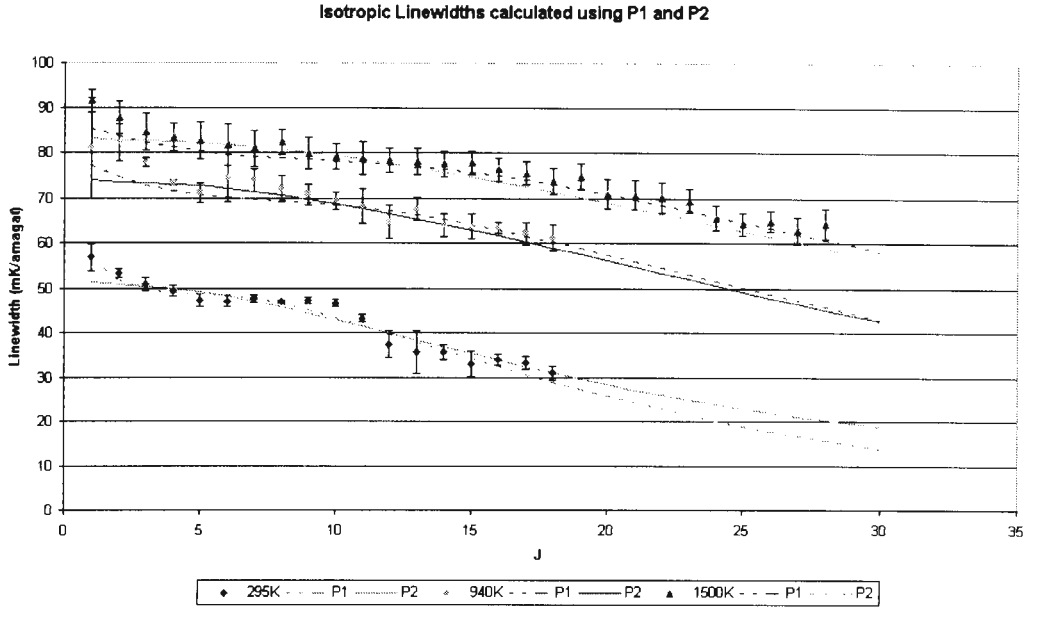

Figure 3.1: Plot of isotropic widths at various temperatures using parameter sets 1 and 2

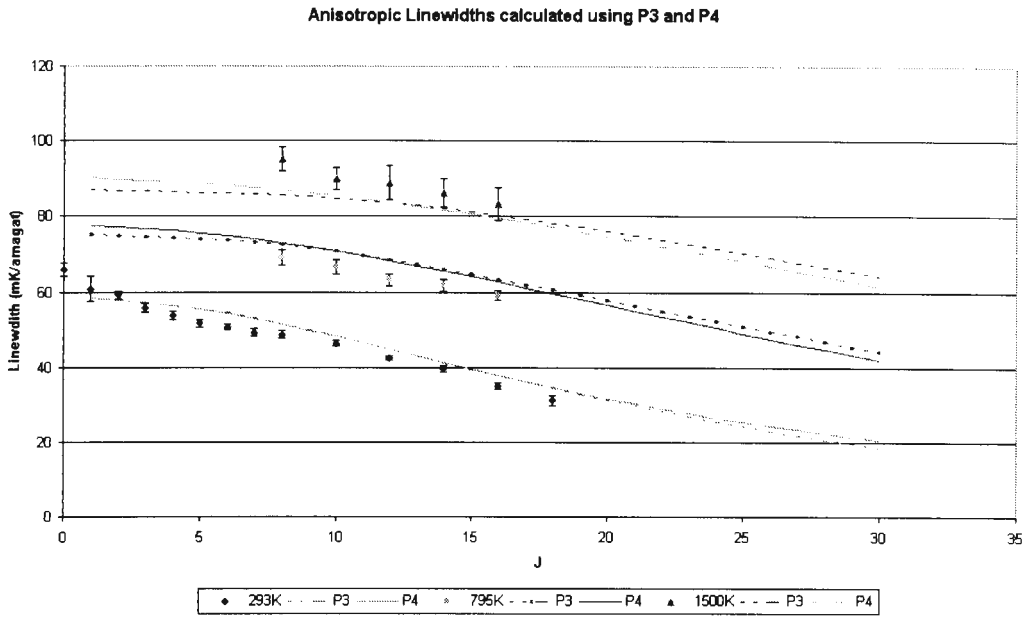

Figure 3.2: Plot of anisotropic widths at various temperatures using parameter sets 3 and 4

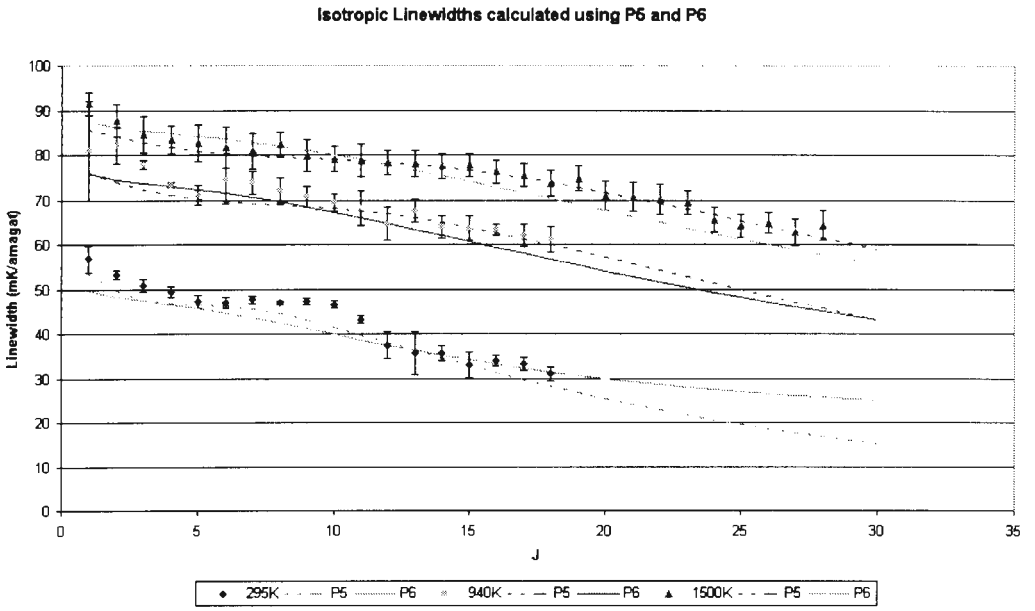

Figure 3.3: Plot of isotropic widths at various temperatures using parameter sets 5 and 6

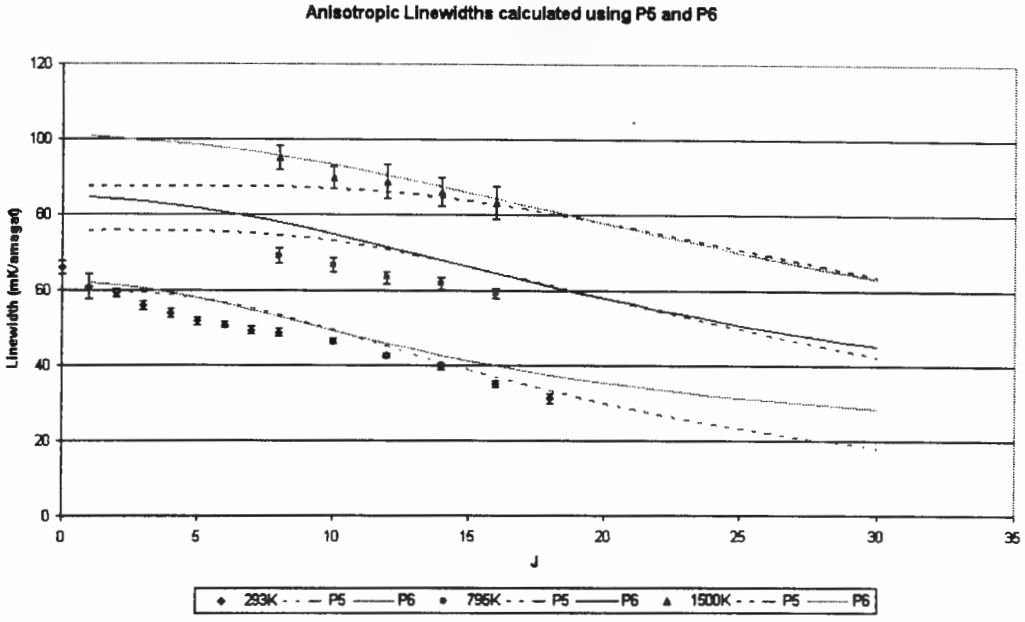

Figure 3.4: Plot of anisotropic widths at various temperatures using parameter sets 5 and 6

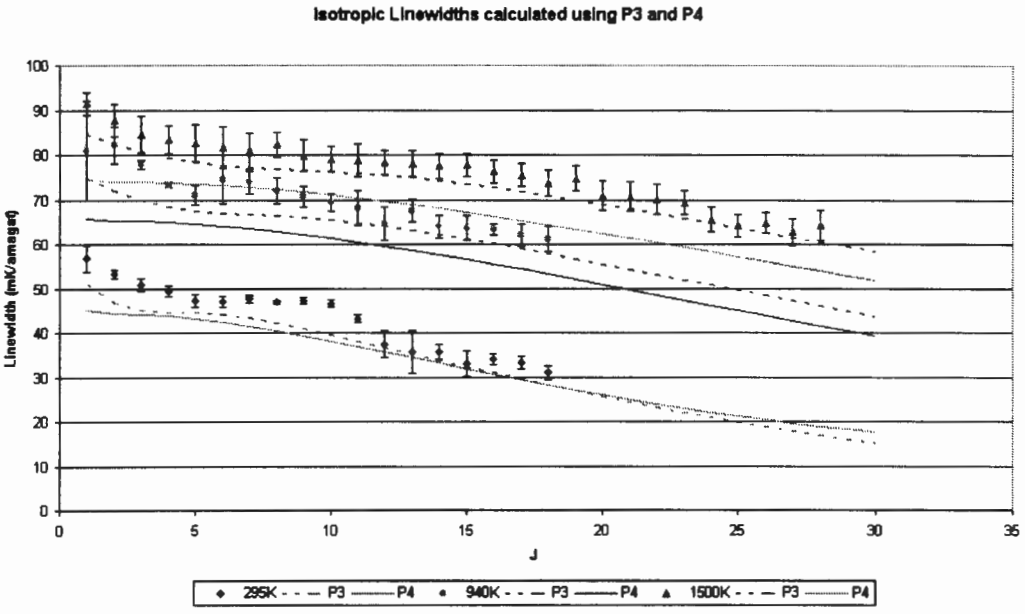

Figure 3.5: Plot of isotropic widths at various temperatures using parameter sets 3 and 4

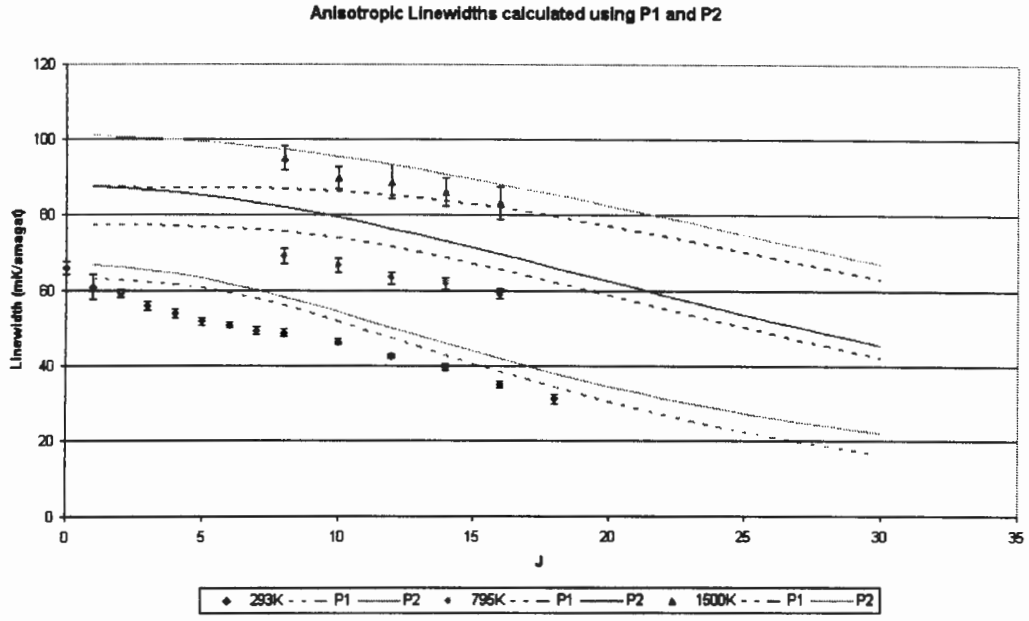

Figure 3.6: Plot of anisotropic widths at various temperatures using parameter sets 1 and 2

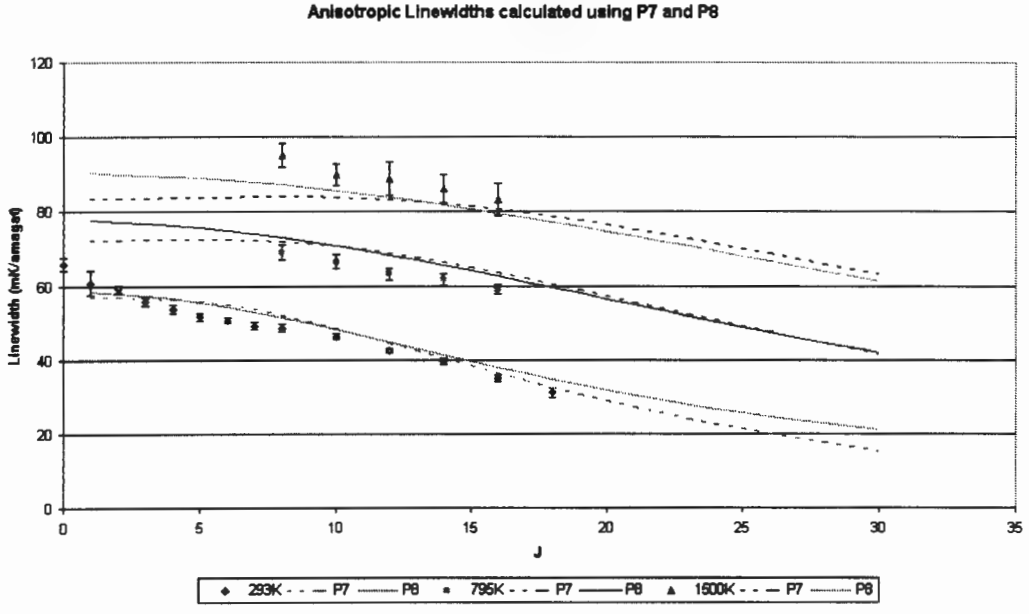

Figure 3.7: Plot of anisotropic widths at various temperatures using parameter sets 7 and 8

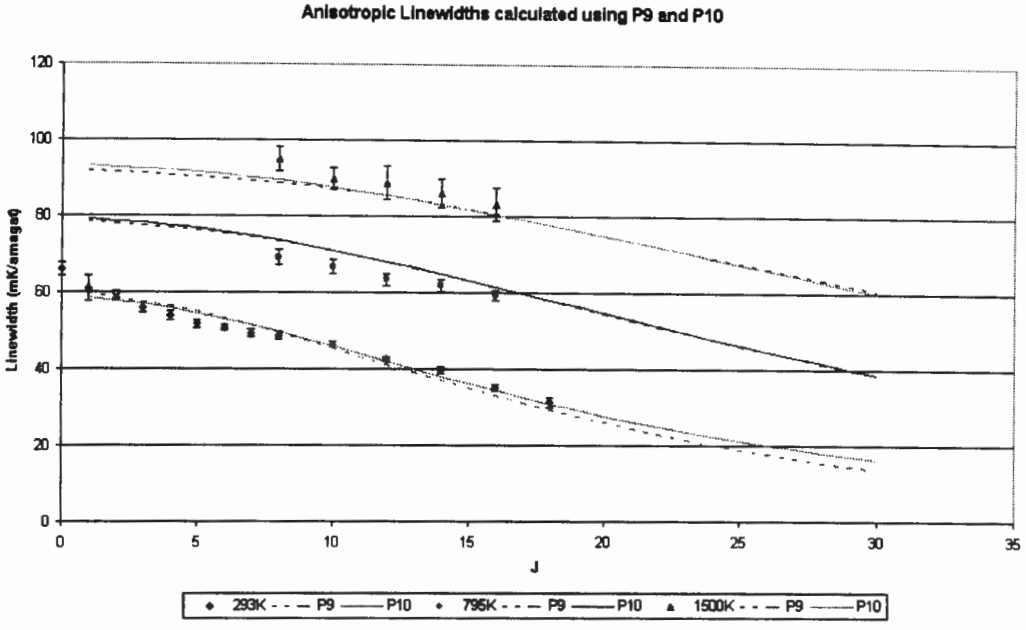

Figure 3.8: Plot of anisotropic widths at various temperatures using parameter sets 9 and 10

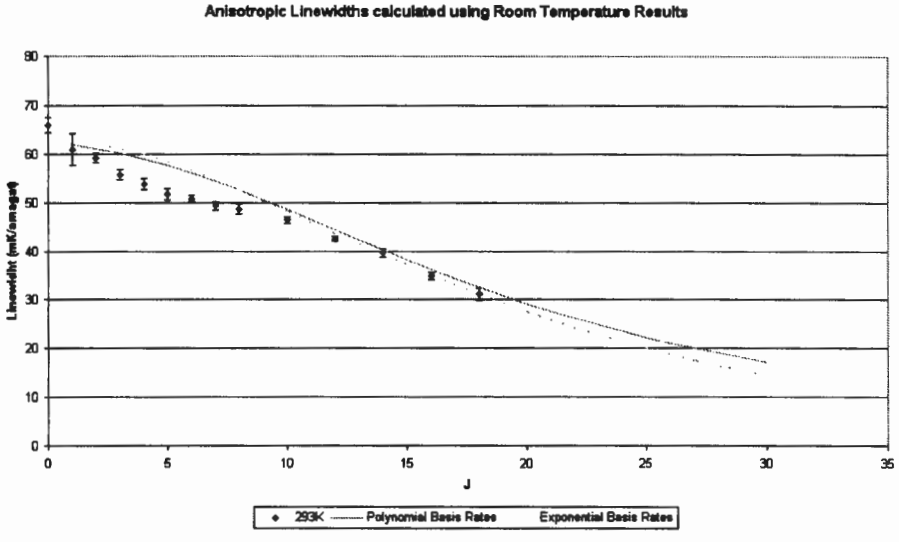

Figure 3.9: Plot of anisotropic widths at 293K using room temperature results

3.4 Swedish Results

The only experimental spectra currently available for testing of these results have kindly been made available by our colleagues in Lund. The spectra consist of room temperature rotational CARS spectra taken without cross-polarized beams so they lack suppression of the non-resonant background. The pressure has been varied to compile a set of spectra. Spectra are available at 1, 5, 10, 15, 20, 30, 40, 50, 60, 70, 80 and 90 bar. At each pressure three spectra have been provided, except for 50 bar where two spectra were provided. To make use of these spectra, the first calculation that must be completed is that of the dispersion relation of the Swedish detector.

3.4.1 Swedish Dispersion Relation

The calculation of the dispersion relation of the Swedish detector needs to be carried out before any real comparison of experimental data and theoretical spectra can be successful.

The Swedish spectra (see appendix E), taken at low pressure (< 10 bar), are used for this calculation. This is done as the high pressure spectra start to show large effects due to pressure broadening and so it is easier to unambiguously identify the peaks corresponding to transitions in the lower pressure spectra. In addition, the nine low pressure spectra are more than sufficient to accurately calculate the dispersion relation.

The distance between peaks is a constant for the rotational spectrum. The identification of the channels corresponding to the peaks is done through numerical differentiation and then the average channel spacing between peaks is found. This is then used to calculate the dispersion of the detector. The result of this calculation is $0.1944\frac{cm^{-1}}{channel}$.

Thus spectra can be calculated with the same spacing which simplifies somewhat the procedure of comparing the spectra.

3.4.2 Swedish Instrument Function

Once the dispersion relation is known, the process of calculating spectra can begin. Although not necessary initially, the details of the instrument are worth clarifying before any further calculations take place.

In principle it is possible to fit the instrument function if sufficient experimental data is available. When non-linear least squares fitting is being implemented, the potential complications make it imperative that we identify values for as many of the parameters as possible. In order to reduce the number of parameters to be fitted, use will be made of the published details

[45] of the Swedish detector; these being that it is Gaussian in nature with a FWHM value of $1.45cm^{-1}$.

3.4.3 Spectral Calculations

The complete process of fitting spectra begins with the calculation of a spectrum given that a suitable set of parameters for the calculation of line-widths can now be chosen. For the spectra to be calculated and all of the following fits, parameter set P5 ($A = 3.347\ \frac{mK}{atm}$, $N = 0.7842$, $\beta = 1.783$ and $l_c = 0.7620$ Å) will be used.

For ease of comparison, spectra will be plotted at 30, 50 and 70 atm as these are the pressures for which results have been published [44, 45]. In addition, spectra at 1 and 90 atm will also be plotted for completeness.

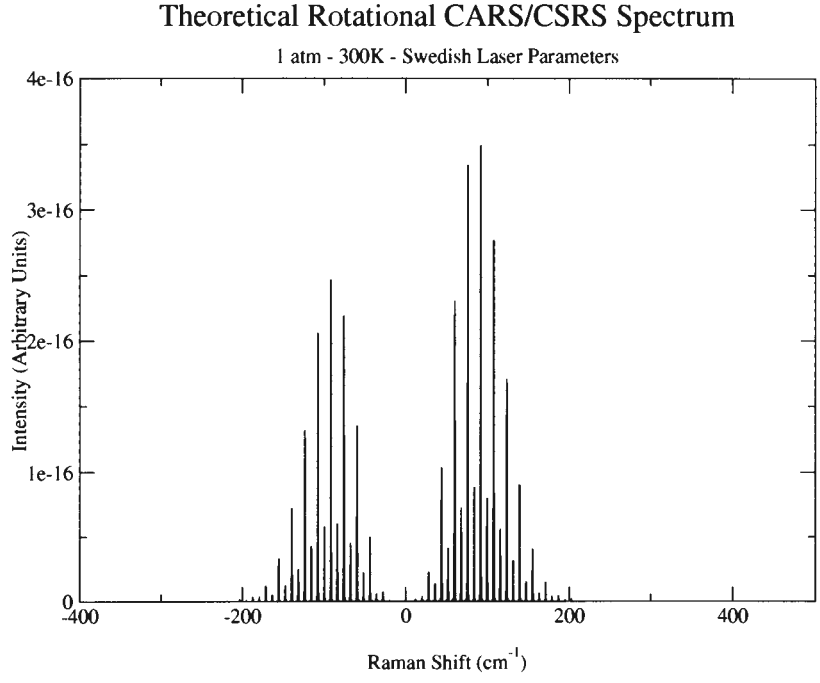

Figure 3.10: Theoretical results at 1 atm

These spectra include the non-resonant background and the overlap from the Stokes band. They are consistent with the results shown in [44, 45], though a different line-width calculation has been used.

To compare accurately with the experimental results we need to convolute the spectra with the instrument function. The changes to the spectra, due

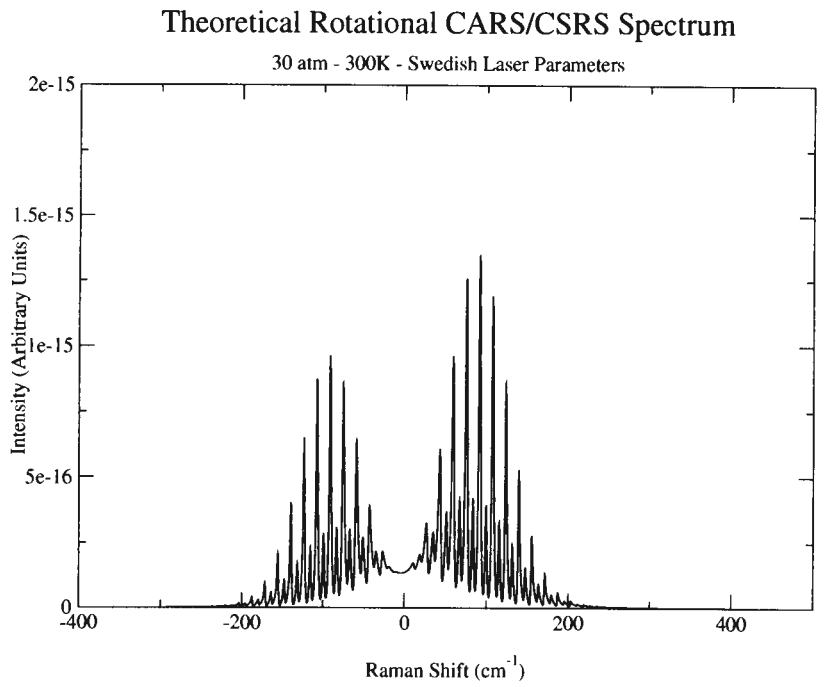

Figure 3.11: Theoretical results at 30 atm

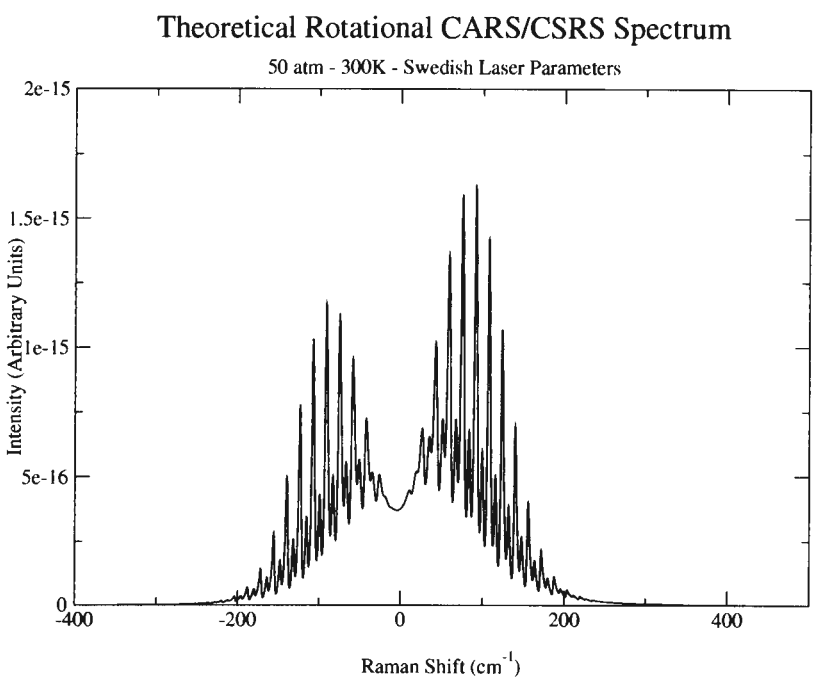

Figure 3.12: Theoretical results at 50 atm

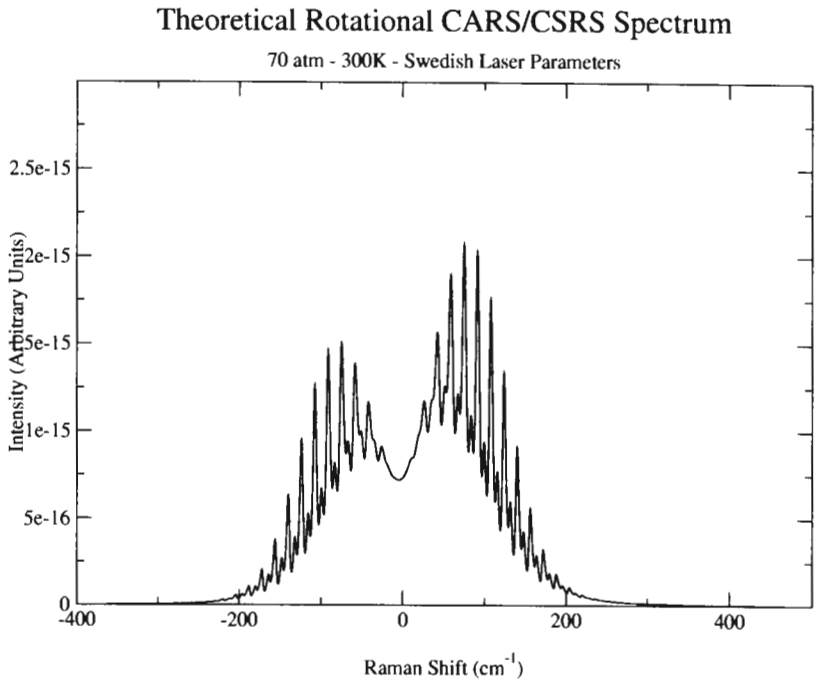

Figure 3.13: Theoretical results at 70 atm

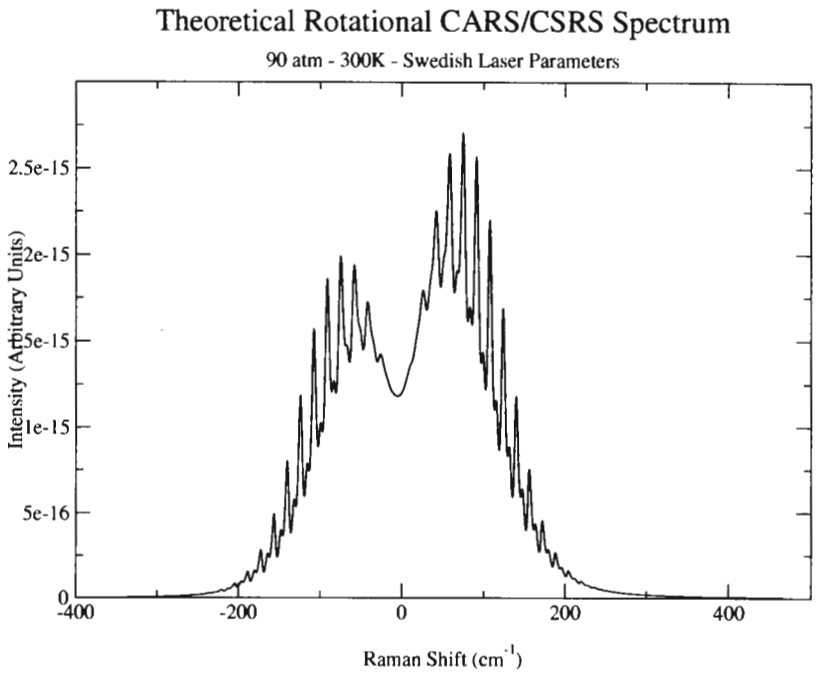

Figure 3.14: Theoretical results at 90 atm

to the instrument function, are quite clear and quite significant at higher pressure.

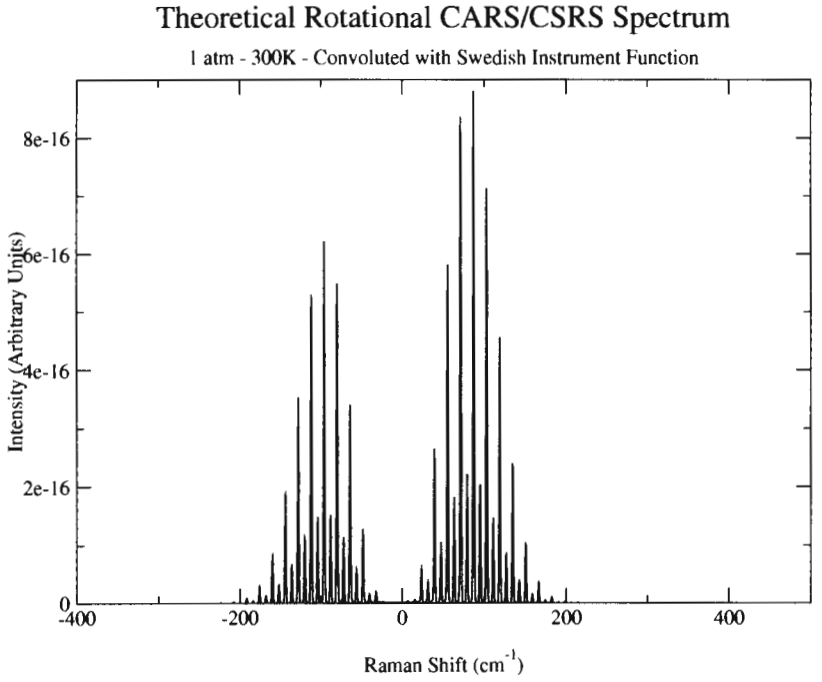

Figure 3.15: Theoretical results at 1 atm

Here, as pointed out in [44, 45], the significant contribution to the CARS spectrum from the CSRS overlap at high pressure can be seen clearly. The spectra are in good agreement with those shown in [44, 45]. For purposes of comparison figures 3.20-3.24 show theoretical and experimental spectra on the axes.

It should be noted that the line-width model used in [44, 45] allows for the accurate reproduction of low pressure spectra but not high pressure spectra. Thus the reproduction of low pressure spectra does not indicate a good spectral modelling capability. In comparing the spectra shown in figures 3.20-3.24 it is clear that, as one goes to higher pressure, the experimental and theoretical spectra agree less.

This does not inhibit the capability of rotational CARS for temperature diagnostics in a piston chamber because the pressures will stay in the range where good agreement is obtained.

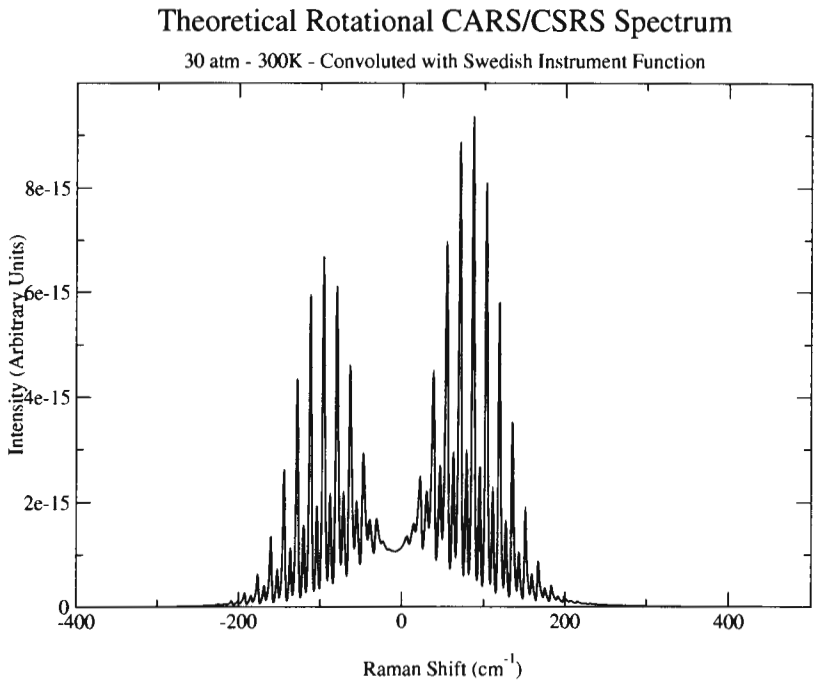

Figure 3.16: Theoretical results at 30 atm

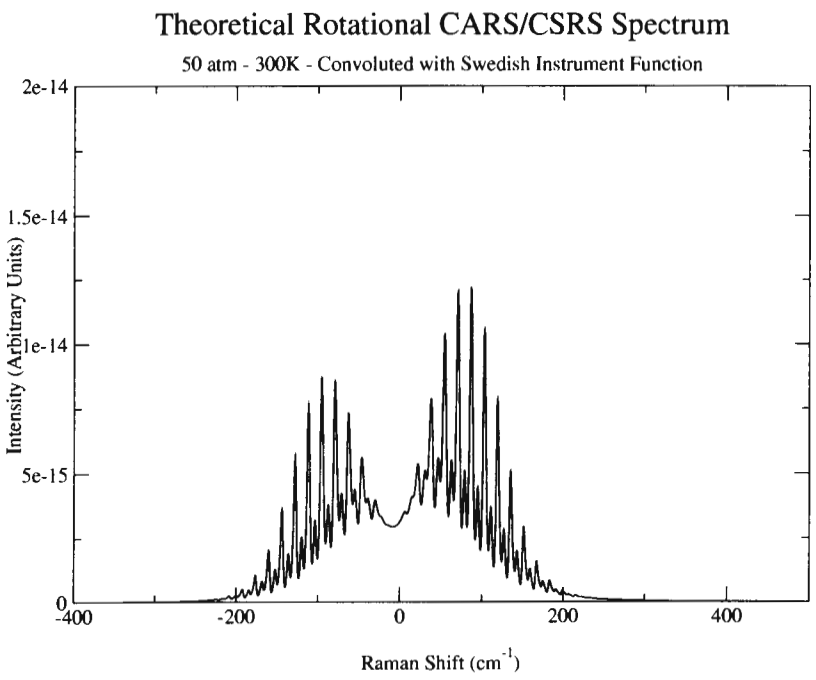

Figure 3.17: Theoretical results at 50 atm

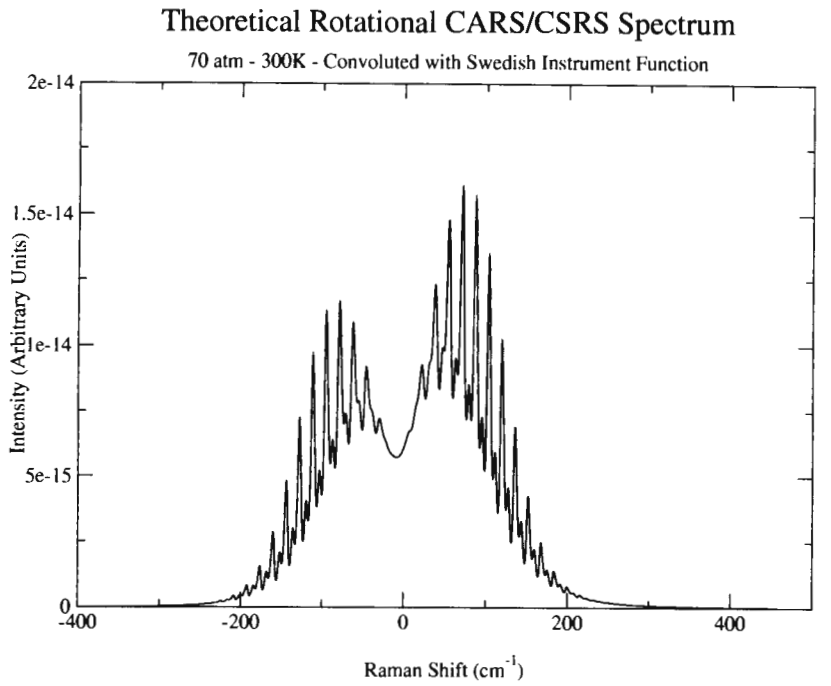

Figure 3.18: Theoretical results at 70 atm

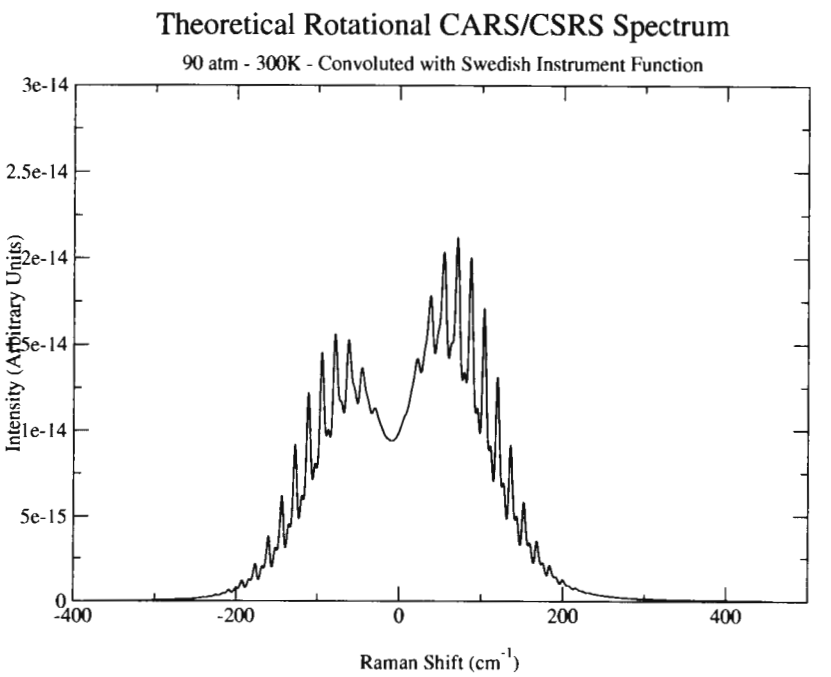

Figure 3.19: Theoretical results at 90 atm

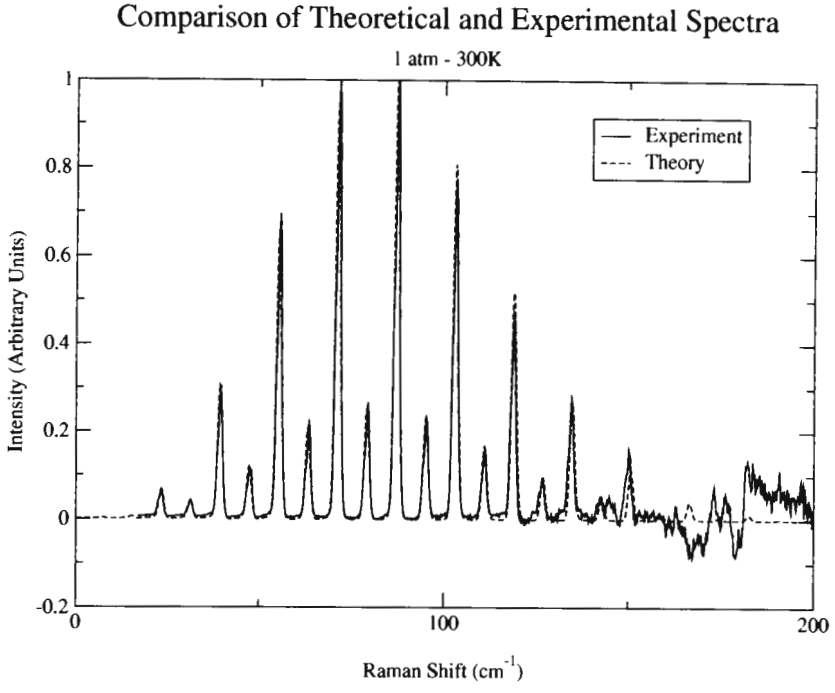

Figure 3.20: Experimental and theoretical spectra at 1 atm

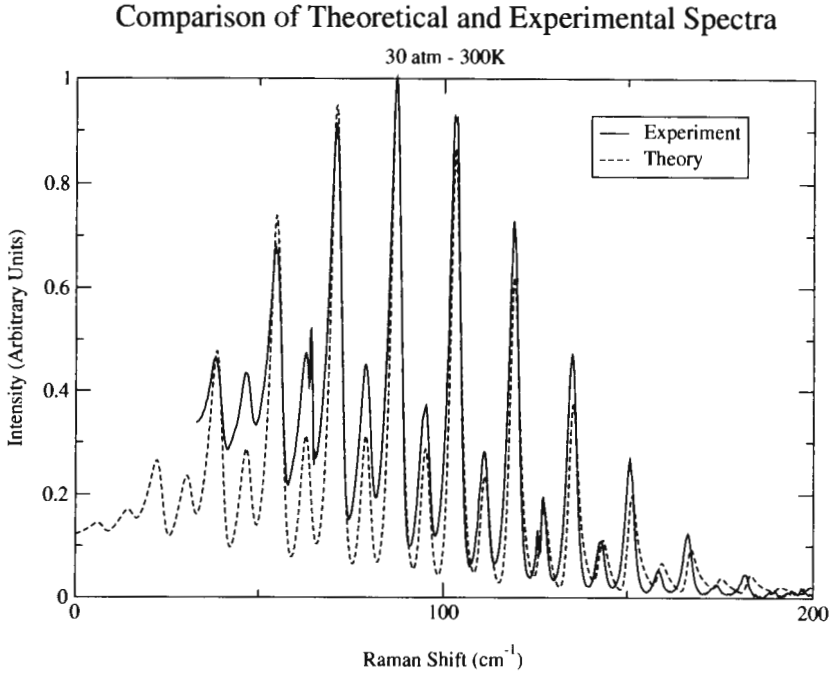

Figure 3.21: Experimental and theoretical spectra at 30 atm

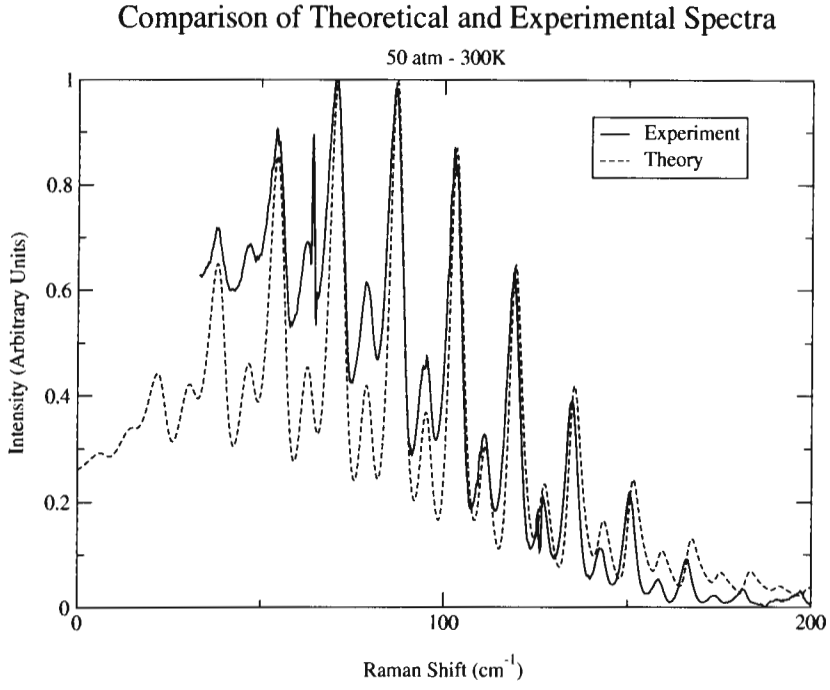

Figure 3.22: Experimental and theoretical spectra at 50 atm

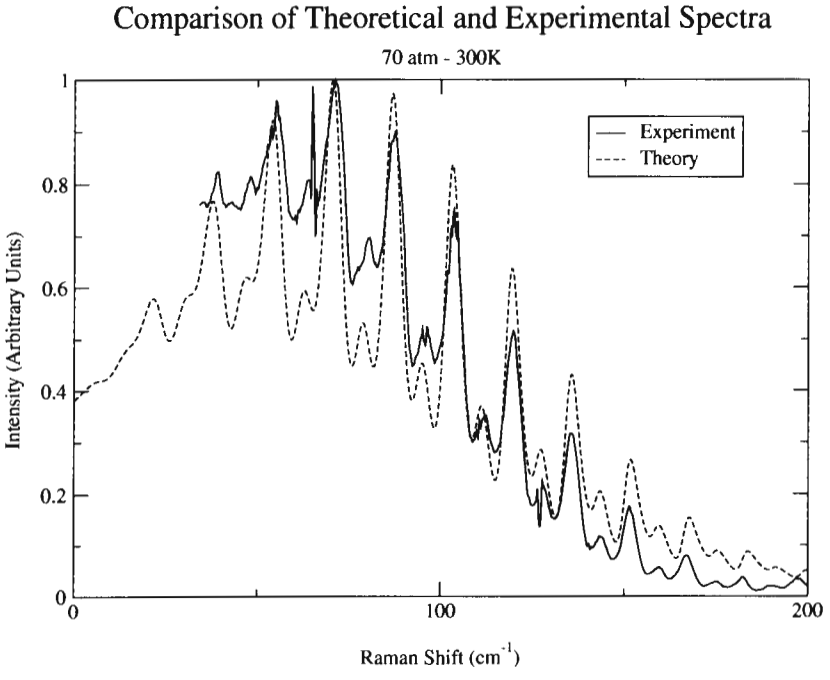

Figure 3.23: Experimental and theoretical spectra at 70 atm

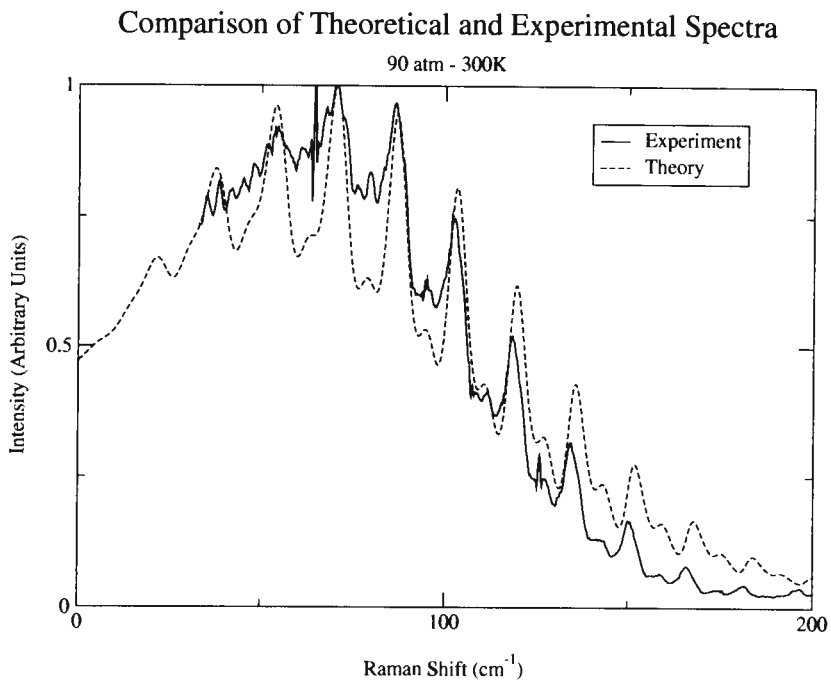

Figure 3.24: Experimental and theoretical spectra at 90 atm

Chapter 4

Conclusions and Recommendations

The line-width model by Bruet was implemented and parameter fits were carried out for various combinations of the forms of the basis rates, adiabaticity exponent and the available data sets. All of these results can be found in 3.3.4. As a check, Bruet's vibrational fit results were reproduced.

Due to the high correlations, l_c was fixed to reasonable values and further fit results produced. The sensitivity of the fits to a variation in the value of l_c was evaluated and these results supported the case in favour of fixing l_c rather than fitting it.

In addition the value of l_c was fixed and the model partially linearised so that an exact solution for the values of A and N could be found for arbitrary values of β/γ. Through the variation of β/γ a clearcut best fit set of parameters was the intended objective. Based on the values of $\frac{\chi^2}{ndf}$ this result was not achieved. The absolute minimum (physical or not) does not appear to reside in the subset of parameter space evaluated by this method. The form of the basis rates is empirical and thus not guaranteed to yield an uncorrelated set of parameters characterising all the experimental data.

The choice of basis rates has thus far been arbitrary. To reduce this degree of freedom, the room temperature rotational data was fitted using the partially linearised model. This removed the temperature scaling parameter N. These results do not favour either form of the basis rates to a significant enough degree to champion it. This is most clearly demonstrated by figure 3.9.

In an implementation of code for rotational CARS temperature diagnostics the best parameter set to use would be P5 based on $\frac{\chi^2}{ndf}$ values.

Given a set of parameters it is then possible to proceed with the calculation of spectra. This procedure can, given current computing capabilities,

be implemented with very little consideration for code optimization. A spectrum can be calculated in less than 2 minutes on a 2200 point grid using code without any optimizations at all. Techniques such as the use of Fourier Transforms could significantly reduce the computation required to calculate a spectrum. Thus the need for comparing experimental spectra with precalculated libraries, during temperature diagnostics, is no longer.

Spectra, calculated at various pressures, using the best fit parameters chosen have been included, as well as experimental spectra at the same pressure. The results are consistent with those in [44, 45]. From these results it does not appear that the line-width model leads to the high pressure discrepancies, as the model implemented here and the one in [44, 45] yield very similar results.

Thus a model which can be used to produce rotational CARS spectra is available which, using currently available experimental data, is able to reproduce rotational spectra at pressures expected in combustion diagnostics. No temperature analysis has been done as yet.

As is often the case, benefit could be derived from more rotational line-width data. The expansion of the rotational data set to higher temperature and higher J values, as well more data for $J < 8$, would allow more 'honest' fits; 'honest' in the sense that the fit would not be dominated to the same extent by the vibrational data as is currently the case. This issue has been discussed with our collaborators who have the capability to take such readings [1].

Another result which could prove useful is a theoretical calculation of a value for l_c. This would have to be an effective value, as the value varies for different components of the potential [68][2].

It is with absolute conviction that, now that rotational line-width data is available, one can say the model put forward by Bruet characterises both rotational and vibrational data. No favoured form of the basis rates can be chosen based on these results.

[1] Can I say this - I know it has been mentioned but are any extra readings actually going to be taken

[2] Is this going to be okay

Appendix A

Isotropic Data

J	Width $(\frac{mK}{atm})$	Uncertainty $(\frac{mK}{atm})$
1	56.8	3
2	53.2	1
3	50.9	1.5
4	49.5	1.2
5	47.3	1.4
6	47	1.1
7	47.6	0.8
8	46.9	0.4
9	47.2	0.7
10	46.6	0.8
11	43.2	0.8
12	37.4	3
13	35.6	4.8
14	35.7	1.7
15	33	2.8
16	33.9	1.2
17	33.2	1.5
18	31	1.6

Table A.1: Isotropic Data at 295K

J	Width $(\frac{mK}{atm})$	Uncertainty $(\frac{mK}{atm})$
1	35.85	1.65
2	35.25	1.35
3	34.85	2.2
4	33.8	1.25
5	32.55	1.05
6	32.5	1.6
7	31.25	1.3
8	30.75	1.1
9	30.9	1.05
10	30.65	1.2
11	29.75	1
12	29.55	1.05
13	28.45	0.9
14	27.55	1.05
15	27.3	0.9
16	27.1	0.85
17	25.85	0.85
18	25.1	0.9
19	24.25	0.5
20	23.6	0.75
21	21.9	0.75
22	21.3	0.65
23	19.9	0.7
24	19.6	0.6
25	18.1	0.75
26	17.45	0.55
27	15.8	0.8

Table A.2: Isotropic Data at 500K

J	Width ($\frac{mK}{atm}$)	Uncertainty ($\frac{mK}{atm}$)
1	34	1.9
2	31.7	0.5
3	30.8	0.7
4	30.7	0.7
5	30.1	0.5
6	30.1	0.6
7	29.6	0.7
8	28.5	0.7
9	29.6	0.9
10	28.9	0.5
11	29.8	1.2
12	28	1
13	28.7	1.7
14	27.3	1.9
15	26.6	0.6
16	25.6	0.5
17	25.1	0.6

Table A.3: Isotropic Data at 600K

J	Width $(\frac{mK}{atm})$	Uncertainty $(\frac{mK}{atm})$
1	28	0.5
2	27.35	1.1
3	26.85	0.95
4	26	1
5	26.25	0.95
6	25.7	0.85
7	24.25	1.15
8	24.4	1
9	24.15	0.8
10	24.2	0.85
11	23.55	0.9
12	23.6	0.95
13	22.55	1.15
14	22.5	1.1
15	22.1	0.8
16	21.45	0.9
17	21.5	0.8
18	21.4	0.85
19	20.5	1.2
20	19.85	1
21	19.55	1.25
22	19.3	0.65
23	18.75	0.7
24	17.85	1.05
25	19	0.85
26	16.65	0.6

Table A.4: Isotropic Data at 730K

J	Width $(\frac{mK}{atm})$	Uncertainty $(\frac{mK}{atm})$
1	25.4	3.5
2	25.8	1.3
3	24.4	0.3
4	23	0.2
5	22.3	0.7
6	23.4	1.7
7	23.2	0.8
8	22.6	0.9
9	22.2	0.7
10	21.8	0.6
11	21.4	1.2
12	20.3	1.2
13	21.2	0.8
14	20.1	0.8
15	20	0.9
16	19.9	0.4
17	19.5	0.8
18	19.2	0.9

Table A.5: Isotropic Data at 940K

J	Width $(\frac{mK}{atm})$	Uncertainty $(\frac{mK}{atm})$
1	23	0.5
2	21.8	0.7
3	21.1	0.7
4	20.75	0.65
5	20.7	0.7
6	20.65	0.65
7	19.95	0.65
8	20.05	0.65
9	19.5	0.65
10	19.85	0.75
11	19.25	0.7
12	19.25	0.6
13	18.85	0.65
14	18.85	0.6
15	18.2	0.6
16	18.15	0.55
17	18.1	0.5
18	18.05	0.6
19	16.8	0.6
20	16.45	0.55
21	16.45	0.6
22	16.15	0.5
23	15.8	0.6
24	16.65	0.5
25	14.95	0.55
26	14.5	0.5
27	14	0.75
28	14	0.5
29	13.2	0.75
30	13.2	0.5

Table A.6: Isotropic Data at 1000K

J	Width $(\frac{mK}{atm})$	Uncertainty $(\frac{mK}{atm})$
1	19	0.9
2	19.1	0.7
3	18.6	0.9
4	18.7	0.6
5	18.8	0.8
6	18.3	0.6
7	18.3	0.8
8	18.6	1.1
9	18.4	2.2
10	17.1	0.9
11	17.3	1.5
12	16.8	0.9
13	16.4	0.9
14	15.9	1.1
15	16.1	0.5

Table A.7: Isotropic Data at 1310K

J	Width ($\frac{mK}{atm}$)	Uncertainty ($\frac{mK}{atm}$)
1	18	0.5
2	17.25	0.7
3	16.65	0.8
4	16.4	0.6
5	16.25	0.8
6	16.05	0.9
7	15.9	0.8
8	16.2	0.55
9	15.7	0.7
10	15.55	0.55
11	15.5	0.7
12	15.4	0.5
13	15.35	0.55
14	15.25	0.55
15	15.3	0.5
16	15	0.5
17	14.85	0.5
18	14.5	0.55
19	14.7	0.55
20	13.95	0.65
21	13.9	0.65
22	13.8	0.65
23	13.65	0.5
24	12.9	0.55
25	12.65	0.5
26	12.75	0.45
27	12.35	0.6
28	12.65	0.65

Table A.8: Isotropic Data at 1500K

Appendix B

Anisotropic Data

J	Width ($\frac{mK}{atm}$)	Uncertainty ($\frac{mK}{atm}$)
0	66.36	1.62
1	61.26	3.32
2	59.56	0.98
3	56.16	1.08
4	54.08	1.19
5	52	1.09
6	51.08	0.67
7	49.59	0.93
8	49	0.99
10	46.71	0.63
12	42.79	0.51
14	39.92	0.82
16	35.14	0.85
18	31.36	1.26

Table B.1: Anisotropic Data at 293K

J	Width ($\frac{mK}{amagat}$)	Uncertainty ($\frac{mK}{amagat}$)
8	53.18	1.03
10	50.09	0.21
12	46.27	0.85
14	43.09	0.6
16	38.01	0.76

Table B.2: Anisotropic Data at 296K

J	Width ($\frac{mK}{amagat}$)	Uncertainty ($\frac{mK}{amagat}$)
8	69.1	2
10	66.6	1.8
12	63.2	1.6
14	61.8	1.6
16	59.1	1.3

Table B.3: Anisotropic Data at 795K

J	Width ($\frac{mK}{amagat}$)	Uncertainty ($\frac{mK}{amagat}$)
8	83.3	2.7
10	76.8	1.3
12	72.3	1.2
14	71.6	1.3
16	68.6	2.5

Table B.4: Anisotropic Data at 1000K

J	Width ($\frac{mK}{amagat}$)	Uncertainty ($\frac{mK}{amagat}$)
8	92.7	3
10	83	2.2
12	78.2	2.8
14	77.7	2.1
16	73.8	1.8

Table B.5: Anisotropic Data at 1200K

J	Width ($\frac{mK}{amagat}$)	Uncertainty ($\frac{mK}{amagat}$)
8	95.1	3.2
10	89.9	2.9
12	88.9	4.6
14	86.1	3.8
16	83.3	4.4

Table B.6: Anisotropic Data at 1500K

Appendix C

l_c Sensitivity, Exponential Basis Rates

Fit Results		Correlations		
Parameter	Value	$A(\frac{mK}{amagat})$	N	β
$A(\frac{mK}{amagat})$	7.930	1.000	0.9273	1.000
N	0.8072	-	1.000	0.9272
β	5.160	-	-	1.000
Error $(\frac{mK^2}{amagat})$		4.365		

Table C.1: Parameters for a reduced Levenberg-Marquardt fit to anisotropic data with $n = 2$ and an exponential form of the basis rates with $l_c = 0.5$Å

Fit Results		Correlations		
Parameter	Value	$A(\frac{mK}{amagat})$	N	β
$A(\frac{mK}{amagat})$	4.000	1.000	0.4879	0.9999
N	0.7852	-	1.000	0.4865
β	2.365	-	-	1.000
Error $(\frac{mK^2}{amagat^2})$		4.221		

Table C.2: Parameters for a reduced Levenberg-Marquardt fit to anisotropic data with $n = 2$ and an exponential form of the basis rates with $l_c = 0.6$Å

Fit Results		Correlations		
Parameter	Value	$A(\frac{mk}{amagat})$	N	β
$A(\frac{mk}{amagat})$	3.343	1.000	9.822×10^{-2}	0.6919
N	0.7822	-	1.000	1.939×10^{-2}
β	1.887	-	-	1.000
Error $(\frac{mK^2}{amagat^2})$		4.334		

Table C.3: Parameters for a reduced Levenberg-Marquardt fit to anisotropic data with $n = 2$ and an exponential form of the basis rates with $l_c = 0.65$Å

Fit Results		Correlations		
Parameter	Value	$A(\frac{mK}{amagat})$	N	β
$A(\frac{mK}{amagat})$	2.928	1.000	0.4035	0.9997
N	0.7807	-	1.000	0.4010
β	1.586	-	-	1.000
Error $(\frac{mK^2}{amagat^2})$		4.557		

Table C.4: Parameters for a reduced Levenberg-Marquardt fit to anisotropic data with $n = 2$ and an exponential form of the basis rates with $l_c = 0.7$Å

Fit Results		Correlations		
Parameter	Value	$A(\frac{mK}{amagat})$	N	β
$A(\frac{mK}{amagat})$	2.638	1.000	0.3909	0.9996
N	0.7797	-	1.000	0.3880
β	1.377	-	-	1.000
Error $(\frac{mK^2}{amagat^2})$		4.884		

Table C.5: Parameters for a reduced Levenberg-Marquardt fit to anisotropic data with $n = 2$ and an exponential form of the basis rates with $l_c = 0.75$Å

Fit Results		Correlations		
Parameter	Value	$A(\frac{mK}{amagat})$	N	β
$A(\frac{mK}{amagat})$	2.420	1.000	0.3843	0.9994
N	0.7789	-	1.000	0.3809
β	1.223	-	-	1.000
Error $(\frac{mK^2}{amagat^2})$		5.303		

Table C.6: Parameters for a reduced Levenberg-Marquardt fit to anisotropic data with $n = 2$ and an exponential form of the basis rates with $l_c = 0.8$Å

Fit Results		Correlations		
Parameter	Value	$A(\frac{mK}{amagat})$	N	β
$A(\frac{mK}{amagat})$	2.251	1.000	0.3805	0.9993
N	0.7781	-	1.000	0.3766
β	1.105	-	-	1.000
Error $(\frac{mK^2}{amagat^2})$		5.802		

Table C.7: Parameters for a reduced Levenberg-Marquardt fit to anisotropic data with $n = 2$ and an exponential form of the basis rates with $l_c = 0.85$Å

Fit Results		Correlations		
Parameter	Value	$A(\frac{mK}{amagat})$	N	β
$A(\frac{mK}{amagat})$	2.115	1.000	0.3781	0.9991
N	0.7772	-	1.000	0.3739
β	1.013	-	-	1.000
Error $(\frac{mK^2}{amagat^2})$		6.365		

Table C.8: Parameters for a reduced Levenberg-Marquardt fit to anisotropic data with $n = 2$ and an exponential form of the basis rates with $l_c = 0.9$Å

Fit Results		Correlations		
Parameter	Value	$A(\frac{mK}{amagat})$	N	β
$A(\frac{mK}{amagat})$	1.909	1.000	0.3753	0.9988
N	0.7753	-	1.000	0.3703
β	0.8796	-	-	1.000
Error $(\frac{mK^2}{amagat^2})$		7.636		

Table C.9: Parameters for a reduced Levenberg-Marquardt fit to anisotropic data with $n = 2$ and an exponential form of the basis rates with $l_c = 1.0$Å

Appendix D

l_c Sensitivity, Polynomial Basis Rates

Fit Results		Correlations		
Parameter	Value	$A(\frac{mK}{amagat})$	N	γ
$A(\frac{mK}{amagat})$	631.3	1.000	-0.7861	1.000
N	-0.1929	-	1.000	-0.7861
γ	2.246	-	-	1.000
Error $(\frac{mK^2}{amagat^2})$		4.388		

Table D.1: Parameters for a reduced Levenberg-Marquardt fit to anisotropic data with $n = 2$ and a polynomial form of the basis rates with $l_c = 0.5$Å

Fit Results		Correlations		
Parameter	Value	$A(\frac{mK}{amagat})$	N	γ
$A(\frac{mK}{amagat})$	119.5	1.000	-0.3490	1.000
N	-0.1394	-	1.000	-0.3500
γ	1.463	-	-	1.000
Error $(\frac{mK^2}{amagat^2})$		4.078		

Table D.2: Parameters for a reduced Levenberg-Marquardt fit to anisotropic data with $n = 2$ and a polynomial form of the basis rates with $l_c = 0.6$Å

Fit Results		Correlations		
Parameter	Value	$A(\frac{mK}{amagat})$	N	γ
$A(\frac{mK}{amagat})$	88.87	1.000	-0.2817	0.9999
N	-0.1190	-	1.000	-0.2833
γ	1.340	-	-	1.000
Error $(\frac{mK^2}{amagat^2})$		4.011		

Table D.3: Parameters for a reduced Levenberg-Marquardt fit to anisotropic data with $n = 2$ and a polynomial form of the basis rates with $l_c = 0.65$Å

Fit Results		Correlations		
Parameter	Value	$A(\frac{mK}{amagat})$	N	γ
$A(\frac{mK}{amagat})$	72.01	1.000	-0.2325	0.9998
N	-0.1015	-	1.000	-0.2345
γ	1.256	-	-	1.000
Error $(\frac{mK^2}{amagat^2})$		3.974		

Table D.4: Parameters for a reduced Levenberg-Marquardt fit to anisotropic data with $n = 2$ and a polynomial form of the basis rates with $l_c = 0.7$Å

Fit Results		Correlations		
Parameter	Value	$A(\frac{mK}{amagat})$	N	γ
$A(\frac{mK}{amagat})$	61.42	1.000	-0.1931	0.9998
N	-8.653×10^{-2}	-	1.000	-0.1956
γ	1.194	-	-	1.000
Error $(\frac{mK^2}{amagat^2})$		3.958		

Table D.5: Parameters for a reduced Levenberg-Marquardt fit to anisotropic data with $n = 2$ and a polynomial form of the basis rates with $l_c = 0.75$Å

Fit Results		Correlations		
Parameter	Value	$A(\frac{mK}{amagat})$	N	γ
$A(\frac{mK}{amagat})$	54.24	1.000	-0.1602	0.9997
N	-7.383×10^{-2}	-	1.000	-0.1630
γ	1.464	-	-	1.000
Error $(\frac{mK^2}{amagat^2})$		3.961		

Table D.6: Parameters for a reduced Levenberg-Marquardt fit to anisotropic data with $n = 2$ and a polynomial form of the basis rates with $l_c = 0.8$Å

Fit Results		Correlations		
Parameter	Value	$A(\frac{mK}{amagat})$	N	γ
$A(\frac{mK}{amagat})$	49.14	1.000	-0.1320	0.9996
N	-6.313×10^{-2}	-	1.000	-0.1352
γ	1.109	-	-	1.000
Error $(\frac{mK^2}{amagat^2})$		3.979		

Table D.7: Parameters for a reduced Levenberg-Marquardt fit to anisotropic data with $n = 2$ and a polynomial form of the basis rates with $l_c = 0.85$Å

Fit Results		Correlations		
Parameter	Value	$A(\frac{mK}{amagat})$	N	γ
$A(\frac{mK}{amagat})$	45.38	1.000	-0.1075	0.9996
N	-5.419×10^{-2}	-	1.000	-0.1111
γ	1.079	-	-	1.000
Error $(\frac{mK^2}{amagat^2})$		4.013		

Table D.8: Parameters for a reduced Levenberg-Marquardt fit to anisotropic data with $n = 2$ and a polynomial form of the basis rates with $l_c = 0.9$Å

Fit Results		Correlations		
Parameter	Value	$A(\frac{mK}{amagat})$	N	γ
$A(\frac{mK}{amagat})$	40.38	1.000	-6.689×10^{-2}	0.9994
N	-4.082×10^{-2}	-	1.000	-7.100×10^{-2}
γ	1.034	-	-	1.000
Error $(\frac{mK^2}{amagat^2})$		4.128		

Table D.9: Parameters for a reduced Levenberg-Marquardt fit to anisotropic data with $n = 2$ and a polynomial form of the basis rates with $l_c = 1.0$Å

Appendix E

Swedish Experimental Spectra

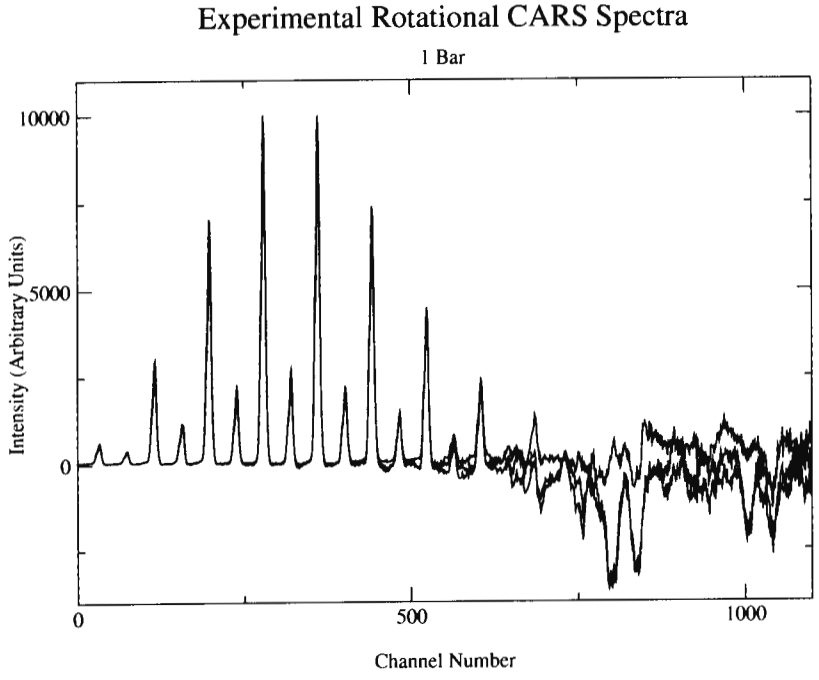

Figure E.1: Experimental results at 1 Bar

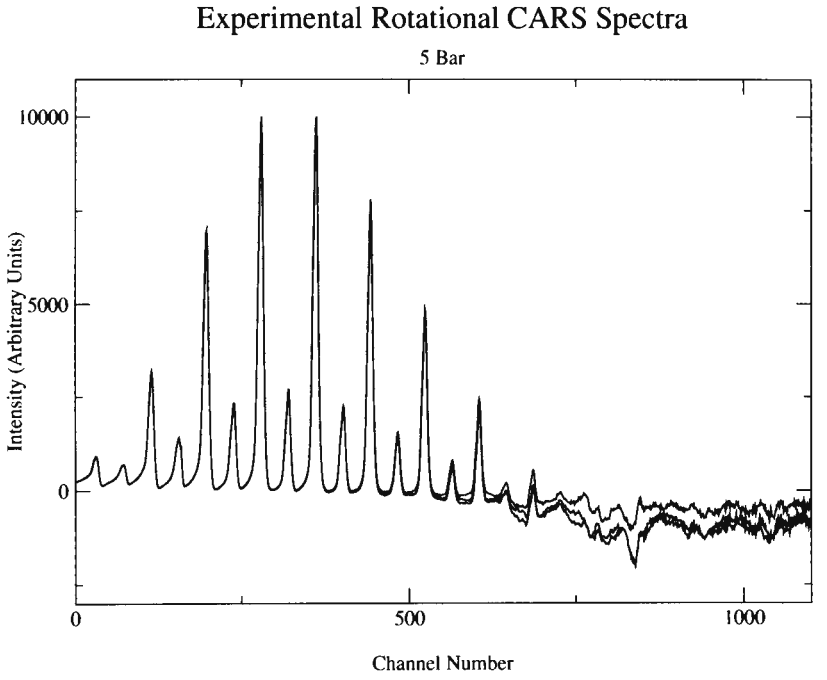

Figure E.2: Experimental results at 5 Bar

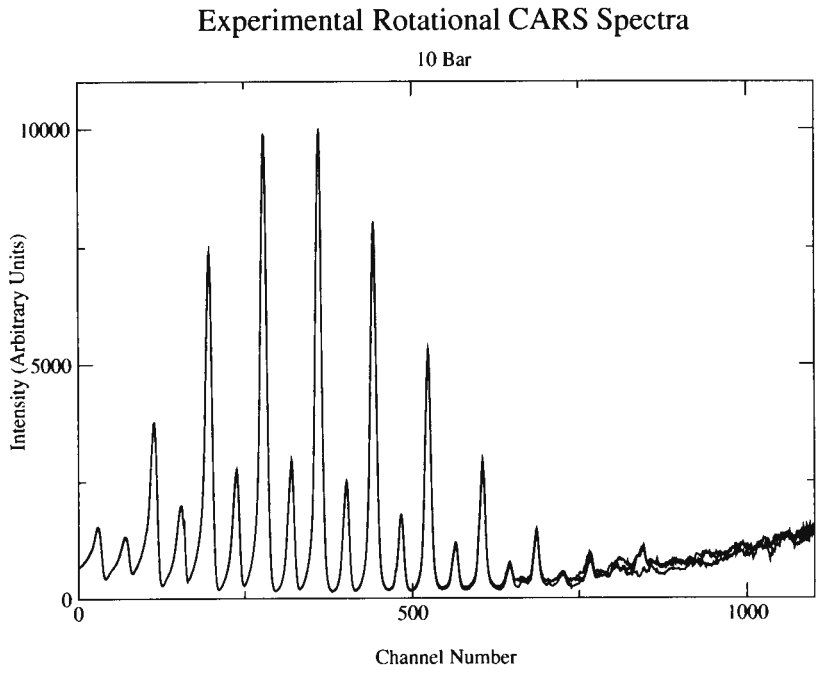

Figure E.3: Experimental results at 10 Bar

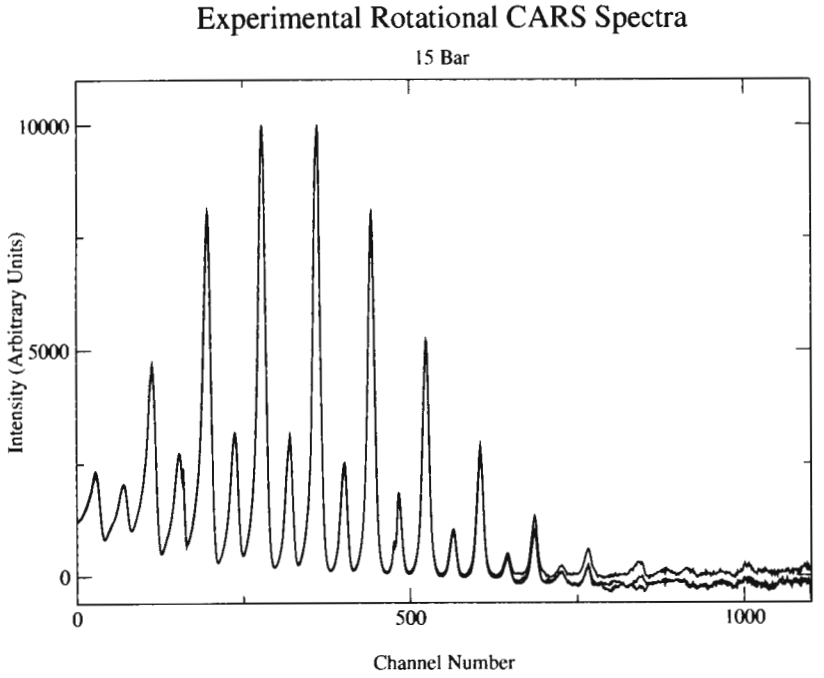

Figure E.4: Experimental results at 15 Bar

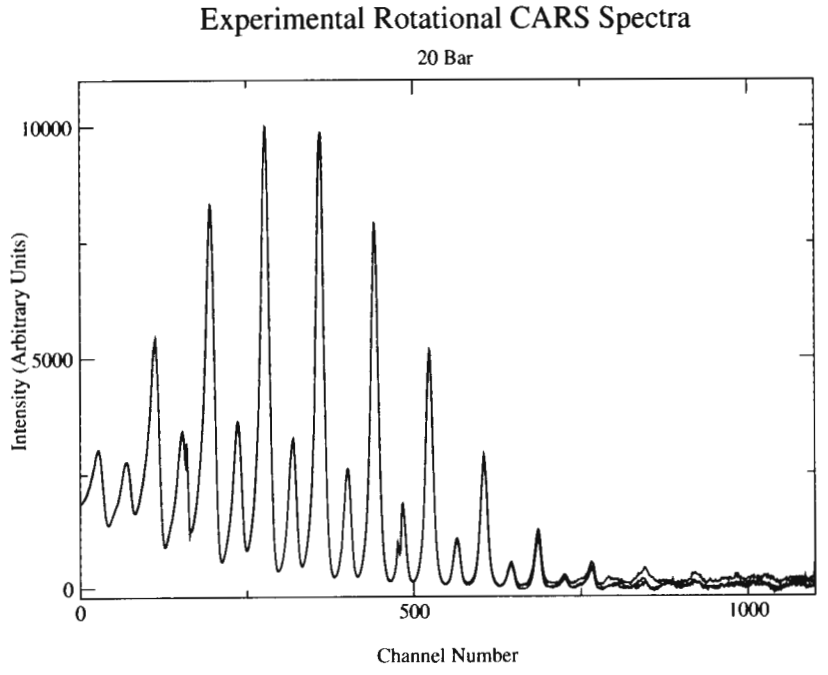

Figure E.5: Experimental results at 20 Bar

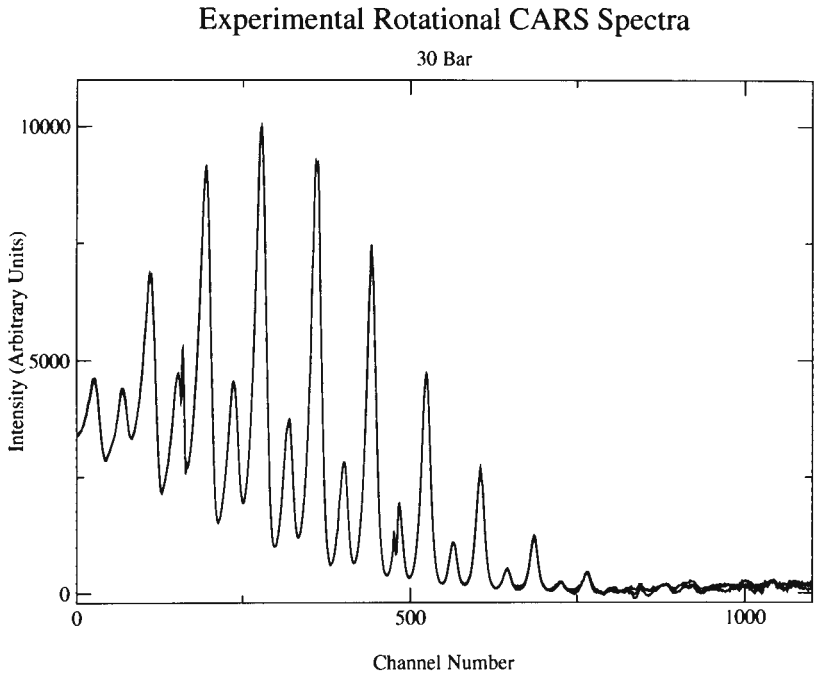

Figure E.6: Experimental results at 30 Bar

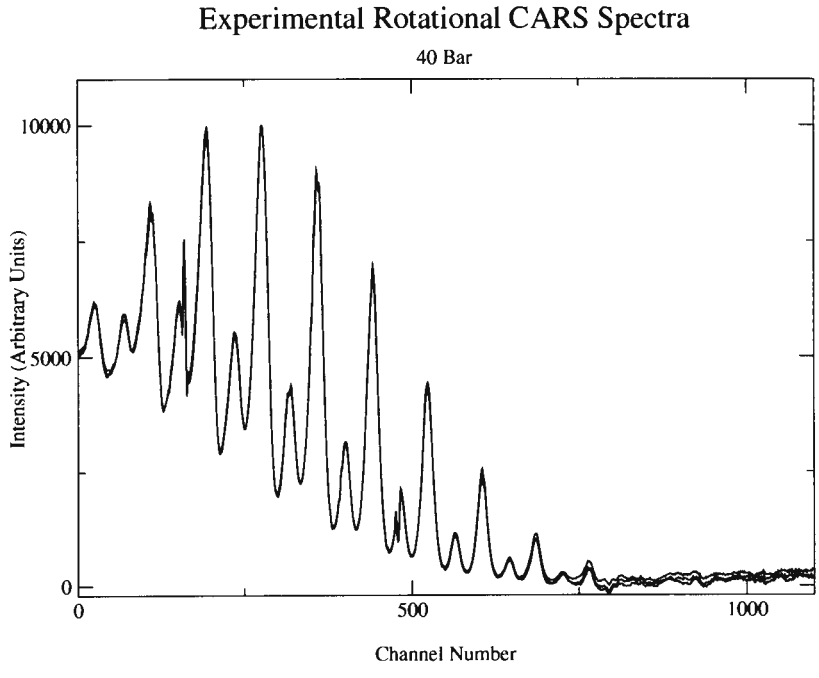

Figure E.7: Experimental results at 40 Bar

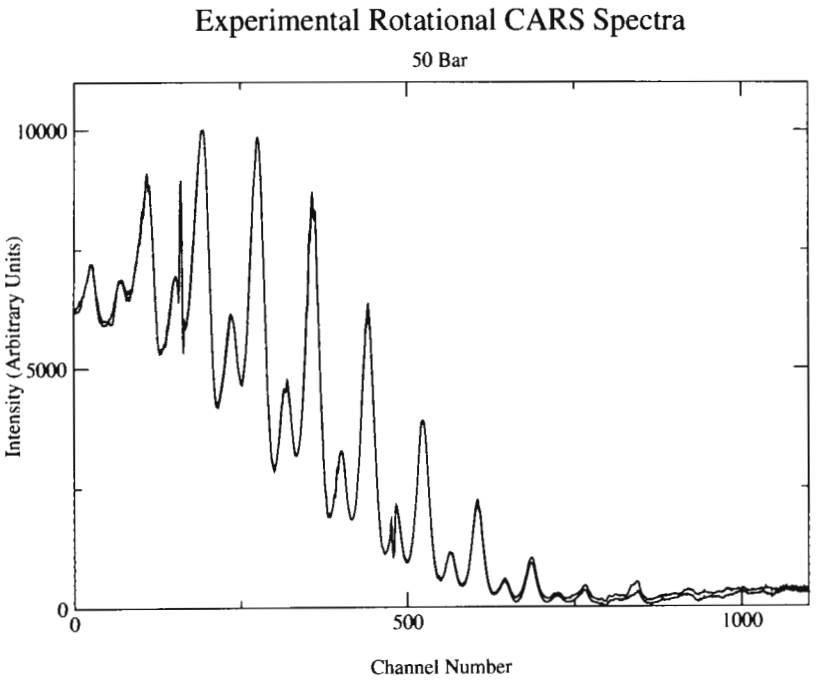

Figure E.8: Experimental results at 50 Bar

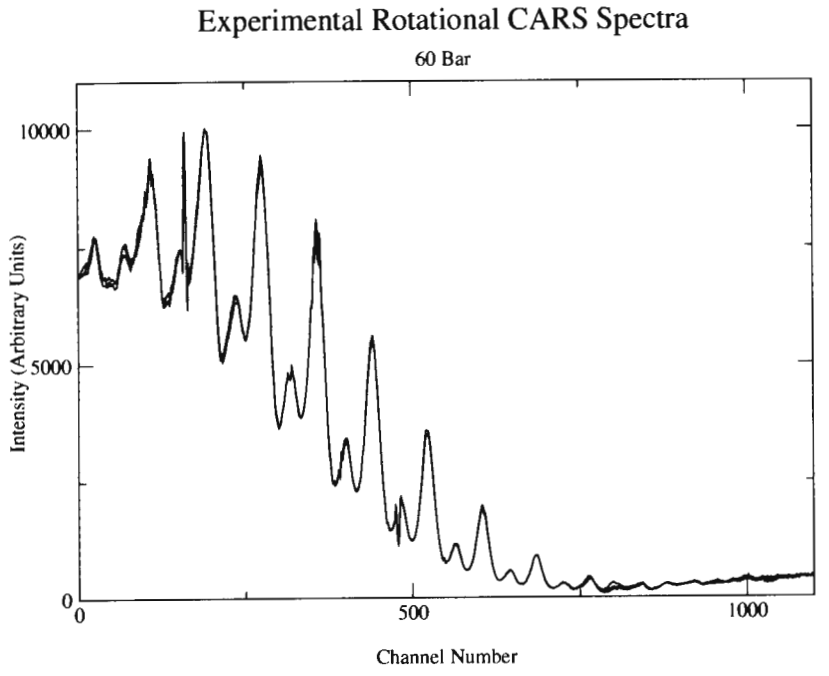

Figure E.9: Experimental results at 60 Bar

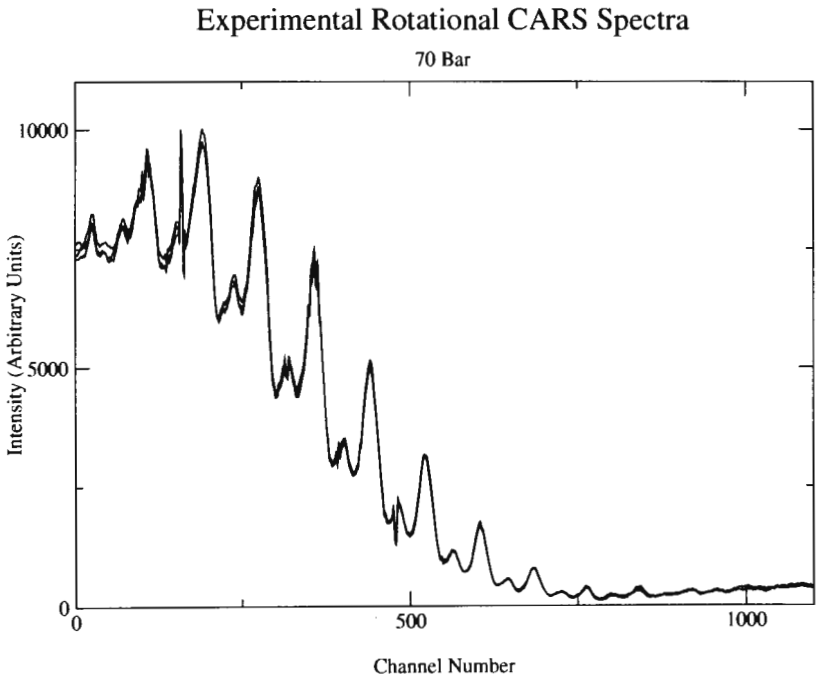

Figure E.10: Experimental results at 70 Bar

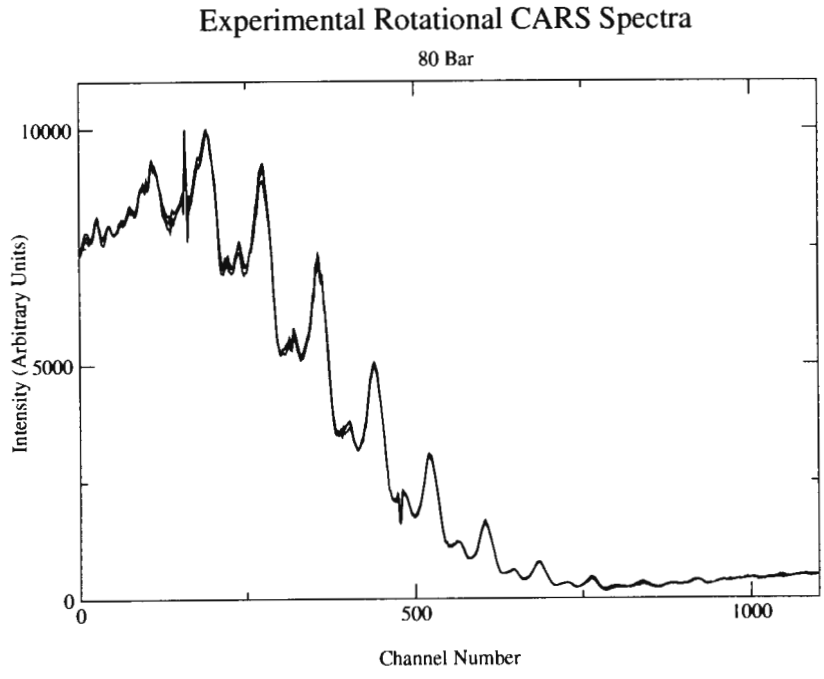

Figure E.11: Experimental results at 80 Bar

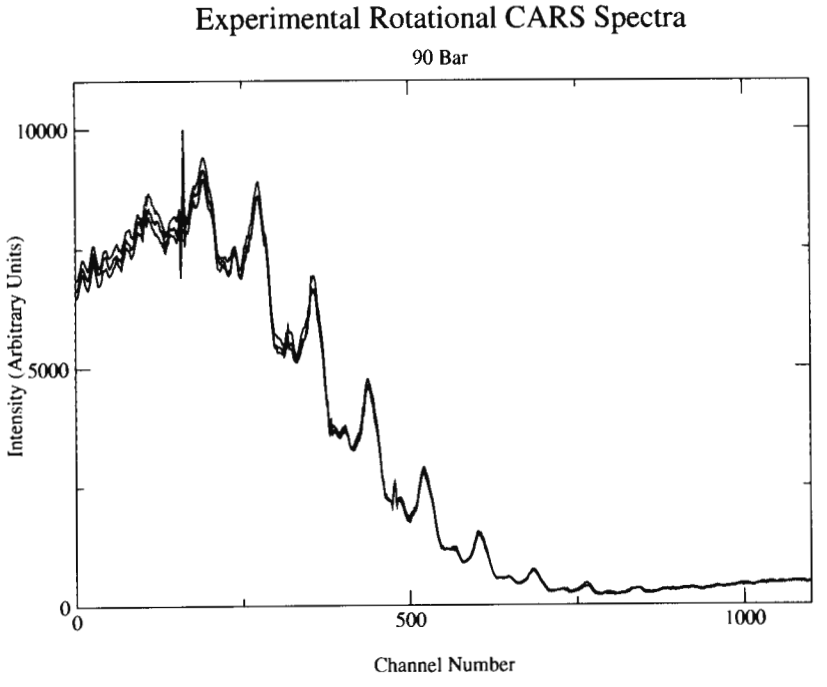

Figure E.12: Experimental results at 90 Bar

Appendix F

Theoretical Rotational Spectra

F.1 500 K

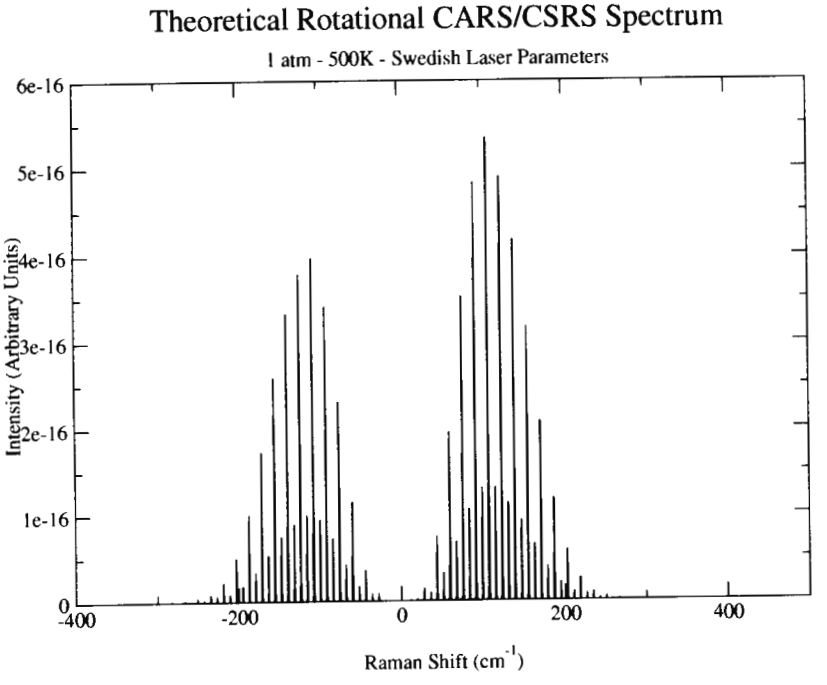

Figure F.1: Theoretical results at 1 atm

F.2 1000 K

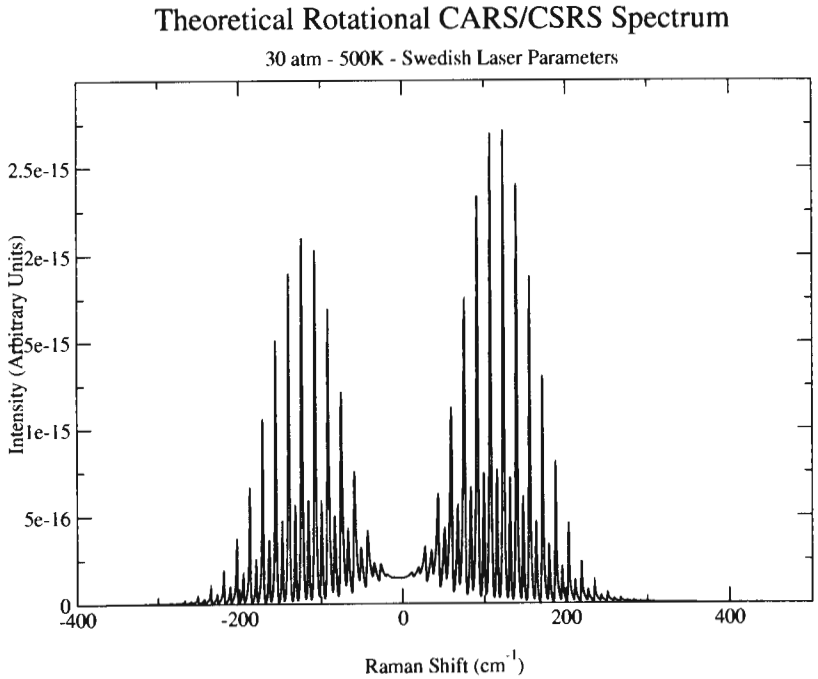

Figure F.2: Theoretical results at 30 atm

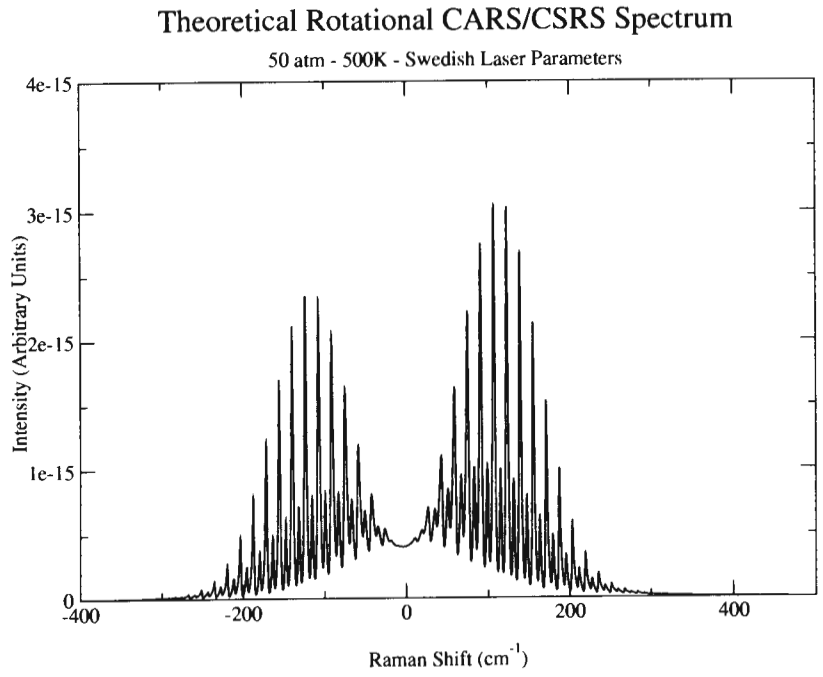

Figure F.3: Theoretical results at 50 atm

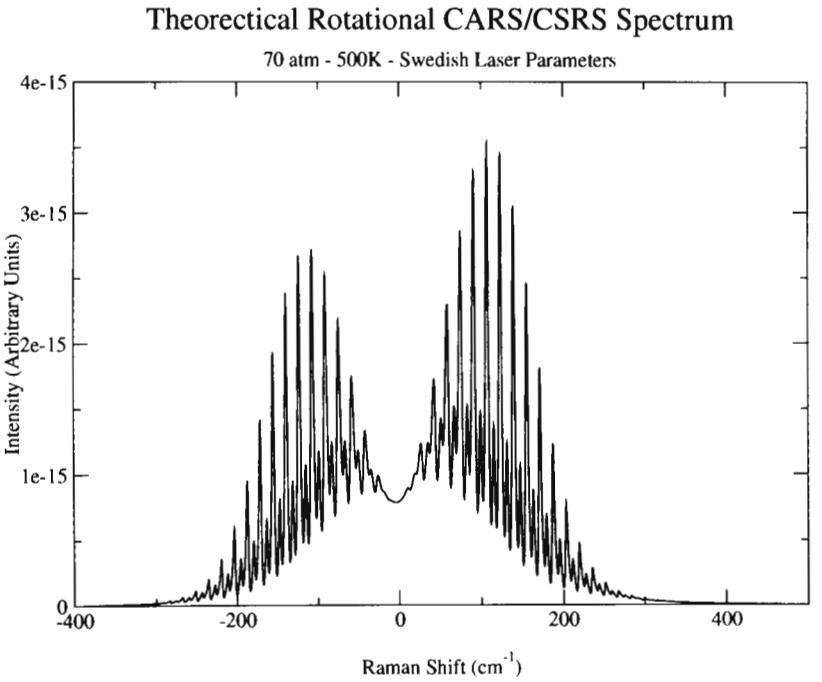

Figure F.4: Theoretical results at 70 atm

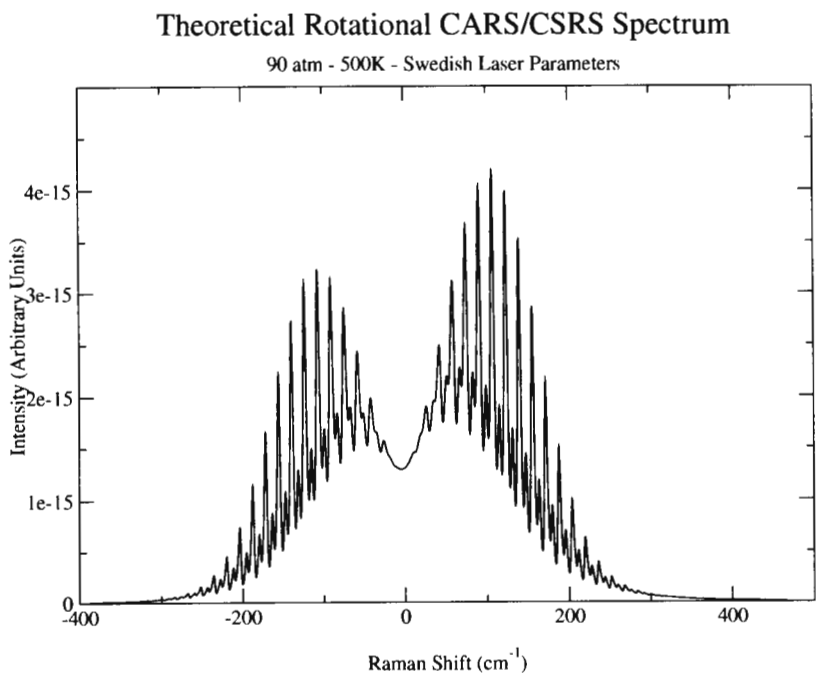

Figure F.5: Theoretical results at 90 atm

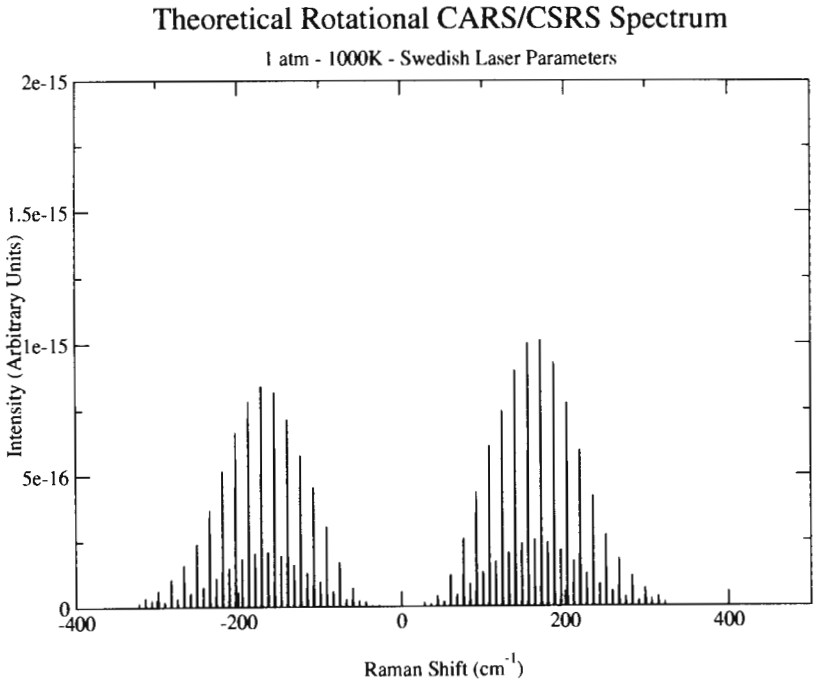

Figure F.6: Theoretical results at 1 atm

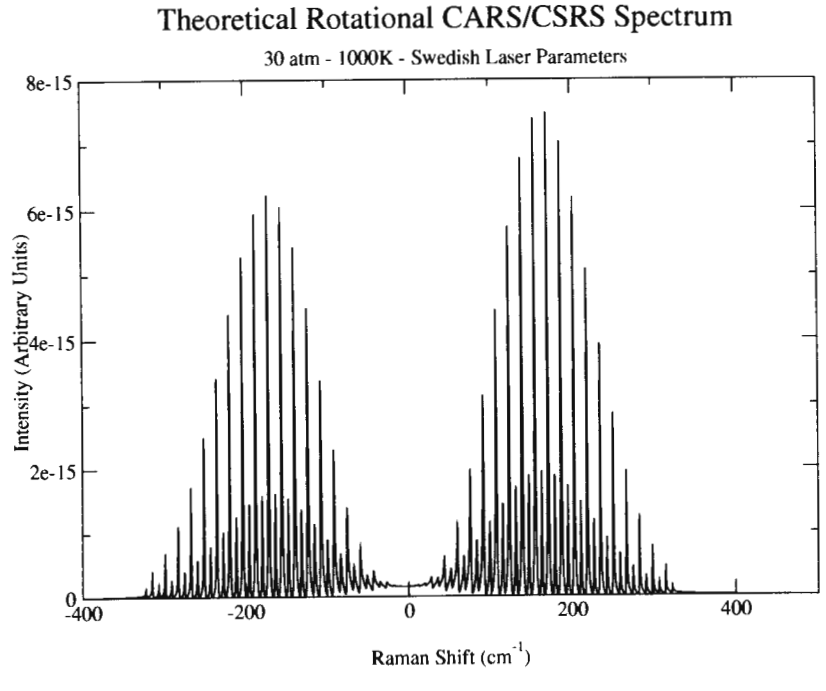

Figure F.7: Theoretical results at 30 atm

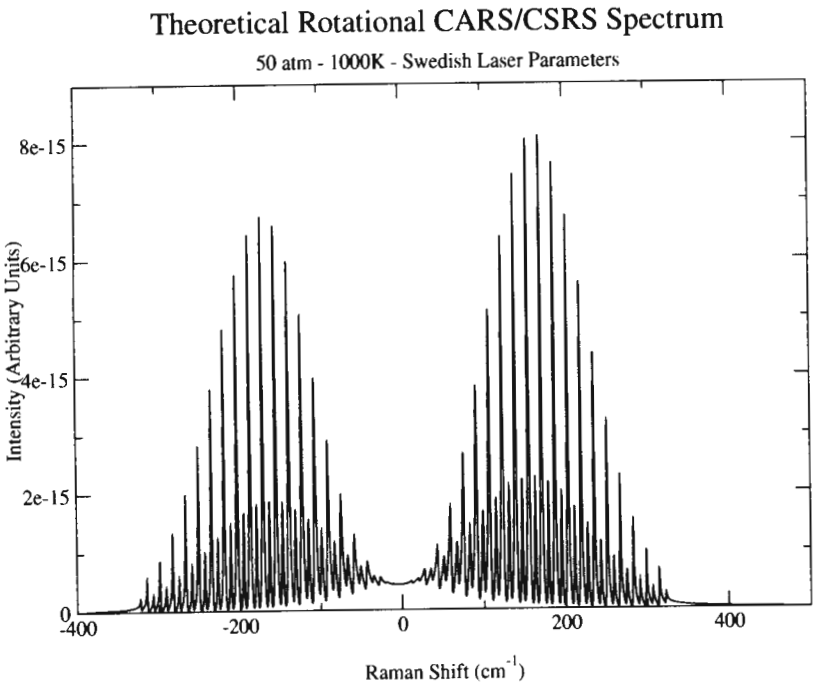

Figure F.8: Theoretical results at 50 atm

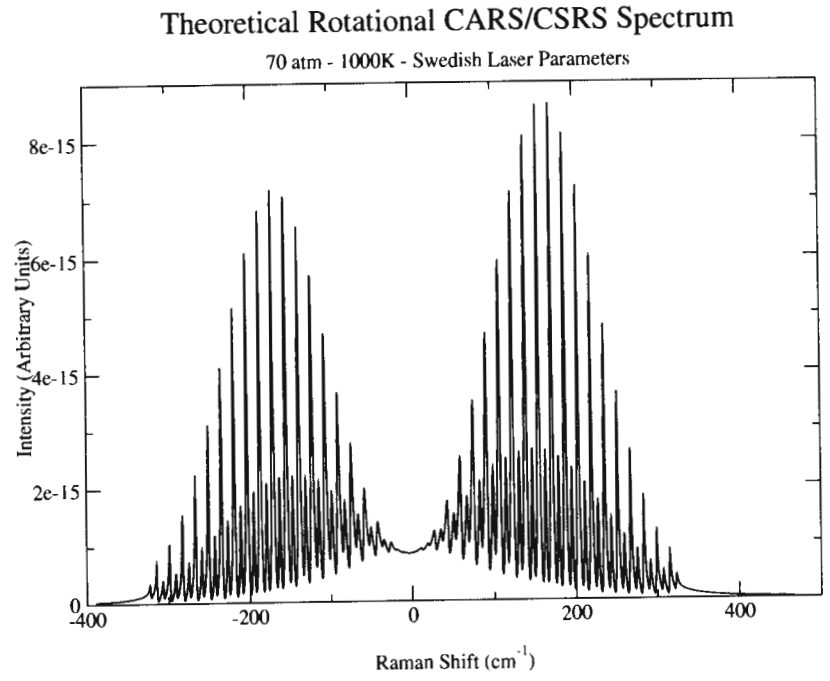

Figure F.9: Theoretical results at 70 atm

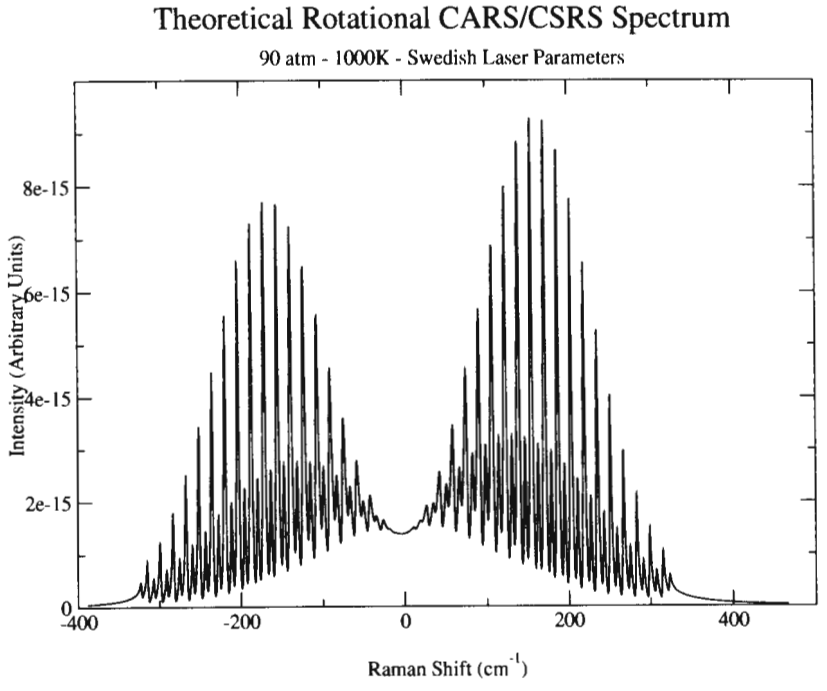

Figure F.10: Theoretical results at 90 atm

Bibliography

[1] C.V. Raman and K.S. Krishnan, *Nature* **121**, 501 (1928)

[2] D.A. Long, *Raman Spectroscopy*, McGraw-Hill International Book Company, New York (1977)

[3] Editor: A. Weber, *Raman Spectroscopy of Gases and Liquids*, Chapter 4: Raman Scattering Cross Sections in Gases and Liquids by H.W. Schrötter and H.W. Klöckner, Springer-Verlag, Berlin, (1979)

[4] S.A.J. Druet and J.-P. E. Taran, *Prog. Quant. Electr.* **7**, 1 (1981)

[5] P.D. Maker and R.W. Terhune, *Phys. Rev.* **137A**, 801 (1965)

[6] R.J.H. Clark and R.E. Hester, *Advances in Non-Linear Spectroscopy*, Chapter 5 by D.A. Greenhalgh, John Wiley & Sons, Chichester, 1988

[7] M.N. Neuman and G.C. Tabisz, *Mol. Phys.* **47**, 849 (1982)

[8] G.J. Rosasco, W. Lempert, W.S. Hurst and A. Fein *Chem. Phys. Lett.* **97**, 435 (1983)

[9] L.A. Rahn and R.E. Palmer, *J. Opt. Soc. Am. B* **3**, 1164 (1986)

[10] Editor: J.R. Duria *Workshop on Advanced Raman Spectroscopy*, Collisional Effects on Raman Q-Branch Spectra at High Temperature by D. Robert (1987)

[11] A.D. May, J.C. Stryland and G. Varghese, *Can. J. Phys.* **48**, 2331 (1970)

[12] M. Aldén, P.-E. Bengtsson, H. Edner, S. Kröll and D. Nilsson *Appl. Opt.* **28**, 3206 (1989)

[13] S. Kröll, P.-E. Bengtsson, M. Aldén and D. Nilsson *Appl. Phys. B* **51**, 25 (1990)

[14] T. Seeger and A. Leipertz, *Appl. Opt.* **35**, 2665 (1996)

[15] A. Thumann, M. Schenk, J. Jonuscheit, T. Seeger and A. Leipertz, *Appl. Opt.* **36**, 3500 (1996)

[16] P.W. Anderson, *Phys. Rev.* **76**, 647 (1949)

[17] J. Fiutak and J. van Kranendonk, *Can. J. Phys.* **40**, 1085 (1962)

[18] M. Baranger, *Phys. Rev.* **111**, 481 (1958)

[19] M. Baranger, *Phys. Rev.* **111**, 494 (1958)

[20] M. Baranger, *Phys. Rev.* **112**, 855 (1958)

[21] J. Fiutak and J. van Kranendonk, *Can. J. Phys.* **41**, 21 (1963)

[22] A. Ben-Reuven, *Phys. Rev.* **141**, 34 (1966)

[23] A. Ben-Reuven, *Phys. Rev.* **145**, 7 (1966)

[24] R.T. Pack, *J. Chem. Phys.* **60**, 633 (1974)

[25] P. McGuire and D.J. Kouri, *J. Chem. Phys.* **60**, 2488 (1974)

[26] R. Goldflam, S. Green and D.J. Kouri, *J. Chem. Phys.* **67**, 4149 (1977)

[27] D. J. Kouri, *Rotational Excitation II: Approximation Methods* Need to check how to reference this correctly

[28] D. Robert and J. Bonamy *J. Physique* ????, 923 (1979)

[29] A. E. De Pristo *J. Chem. Phys.* **73**, 2145 (1980)

[30] Editor: K.P. Lawley *Dyanmics of the Excited State*, Fitting Laws for Rotationally Inelastic Collisions by T. A. Brunner and D. Pritchard, John Wiley and Sons Ltd., (1982)

[31] B. Lavorel, G. Millot, R. Saint-Loup, C. Wenger, H.Berger, J.P. Scala, J. Bonamy and D. Robert *J. Physique* **47**, 417 (1986)

[32] L.A. Tahn and R.E. Palmer *J. Opt. Soc. Am. B* **3**, 1164 (1986)

[33] L.A. Rahn, R.E. Palmer and M.L. Koszykowski *Chem. Phys. Letters* **133**, (1987)

[34] J. Boissoles, C. Boulet, D. Robert and S. Green *J. Chem. Phys.* **87**, 3436 (1987)

[35] B. Lavorel, G. Millot, J. Bonamy and D. Robert *Chem. Phys.* **115**, 69 (1987)

[36] J.P. Looney, G.J. Rosasco, L.A. Rahn, W.S. Hurst and J.W. Hahn *Chem. Phys. Letters* **161**, 232 (1989)

[37] Th. Bouché, Th. Dreier, B. Lange, J. Wolfrum, E.U. Franck and W.Schilling *Appl. Phys. B* **50**, 527 (1990)

[38] G. Millot *J. Chem. Phys.* **93**, 8001 (1990)

[39] L. Bonamy and F. Emond *Phys. Rev. A* **51**, 1235 (1995)

[40] F. Emond *Modelisation des spectres d'absorption infrarouge et de diffusion raman coherente: Generalisatgion des lois d'echelle dynamique a des modes vibrationnels excites avec duree finie de collisions*, PhD Thesis, 3 March 1995

[41] X. Bruet *Mécanismes de relaxation collisionnelle dans l'hydrogène et l'azote en mélange gazeux. Application à la thermométrie optique dans les moteurs cryogéniques et les moteurs à combustion interne.* PhD Thesis, 26 October 2000

[42] M. Abramovitz and I.A. Stegun *Handbook of Mathematical Functions* U.S. Government Printing Office, Washington DC (1964)

[43] Editors: R.J.H. Clark and R.E. Hester *Advances in Non-Linear Spectroscopy*, Chapter 5 Quantitative CARS Spectroscopy by D.A. Greenhalgh, John Wiley and Sons Ltd., (1988)

[44] M. Afzelius and P.-E. Bengtsson *Dual Broadband rotational CARS modelling of nitrogen at pressures up to 9MPa. I. Inter-branch interference effect.* (2001) - submitted for publication.

[45] M. Afzelius, P.-E. Bengtsson, J. Bood, J. Bonamy, F. Chaussard, H. Berger and T. Dreier *Dual Broadband rotational CARS modelling of nitrogen at pressures up to 9MPa. II. Rotational Raman line-widths* (2001) - submitted for publication.

[46] D. Robert, L. Bonamy and J. Bonamy, *Need to find this ref details - have a draft*

[47] J.H. Stufflebeam, J.F. Verdieck and R.J. Hall *CARS Diagnostics of High Pressure and Temperature Gases* Conference Proceedings of AIAA 18th Thermophysics Conference (1983)

[48] Th. Lasser *Opt. Comm.* **35** 447 (1980)

[49] M. L. Koszykowski, R.L. Farrow and R.E. Palmer *Optics Letters* **10** 478 (1985)

[50] R.J. Hall *Opt. Comm.* **52** 360 (1985)

[51] J. Bonamy, L. Bonamy, D. Robert, M.L. Gonze, G. Millot, B. Lavorel and H. Berger *J. Chem. Phys.* **94** 6584 (1991)

[52] S. Temkin, J.M. Thuet, L. Bonamy, J. Bonamy and D. Robert *Chem. Phys.* **158** 89 (1991)

[53] J.I. Steinfeld, P. Ruttenberg, G. Millot, G. Fanjoux and B. Lavorel *J. Phys. Chem.* **95** 9638 (1991)

[54] J.P. Sala, J. Bonamy, D. Robert, B. Lavorel, G. Millot and H. Berger *Chem. Phys.* **106** 427 (1986)

[55] J. van Kranendonk *Can. J. Phys.* **41** 433 (1963)

[56] L. Bonamy, J. Bonamy, D. Robert, S.I. Temkin, G. Millot and B. Lavorel *J. Chem. Phys.* **101** 7350 (1994)

[57] M.L. Koszykowski, L.A. Rahn, R.E. Palmer and M.E. Coltrin *J. Phys. Chem.* **91** 41 (1987)

[58] A.C. Eckbreth *J. Quant. Spectrosc. Radiat. Transfer* **40** 369 (1988)

[59] M. Schenk, A. Thumann, T. Seeger and A. Leipertz *App. Opt.* **37** 5659 (1998)

[60] Editors: E. Castelluci, R. Righini and P. Foggi *Coherent Raman Spectroscopy: Applications and New Developments*, Analysis of CARS spectra using fourier transform techniques by G.N. Robertson and A. Roblin, World Scientific, Singapore (1993)

[61] J.J. BelBruno, J. Gelfand and H. Rabitz *J. Chem. Phys.* **78** 3990 (1983)

[62] A.E. DePristo, J.J. BelBruno, J. Gelfand and H. Rabitz *J. Chem. Phys.* **74** 5031 (1981)

[63] X. Bruet, L. Bonamy and J. Bonamy *Phys. Rev. A* **62** 062702 (2000)

[64] A.E. DePristo, S.D. Augustin, R. Ramaswamy and H. Rabitz *J. Chem. Phys.* **72** 850 (1979)

[65] Editor: W.H. Miller *Dynamics of Molecular Collisions*, R.D. Levine and R.B. Bernstein, Plenum, New York (1975)

[66] L. Bonamy and J. Buldyvera *Phys. Rev. A* **63** 0127175 (2000)

[67] J. Buldyvera and L. Bonamy *Phys. Rev. A* **60** 370 (1999)

[68] L. Bonamy, Private Communication, 2001

[69] L. Martinsson, P.-E. Bengtsson, M. Aldén, S. Kröll, J. Bonamy *J. Chem. Phys.* **99** 2466 (1993)

[70] T. Lundeen, S.-Y. Hou and J.W. Nibler *J. Chem. Phys* **79** 6301 (1983)

[71] G.J. Rosasco and W.S. Hurst *Phys. Rev. A* **32** 281 (1985)

[72] W.G. Rado *Appl. Phys. Lett.* **11** 123 (1967)

[73] M.D. Levenson and S.S. Kano *Introduction to Nonlinear Laser Spectroscopy*, Academic Press, London (1988)

[74] R.W. Hellwarth *Progr. Quant. Electr.* **5**, 1 (1977)

[75] G. Herzberg *Spectra of Diatomic Molecules*, Van Nostrand, New York (1950)